Molten Alkali Metal Borate/Carbonate Salts for High Temperature CO_2 Capture and Electrochemical Conversion

By

Michael Philip Nitzsche

B.S. Mechanical Engineering, Computer Science

Rutgers University, 2019

Submitted to the Department of Mechanical Engineering on August 13 2021

in partial fulfillment of the requirements for the

Degree of Master of Science in Mechanical Engineering

At the

MASSACHUSETTS INSTITUTE OF TECHNOLOGY

September 2021

Author .....

Department of Mechanical Engineering
August 13 2021

Certified by .....

T. Alan Hatton
Ralph Landau Professor, Department of Chemical Engineering Director,
David H. Koch School of Chemical Engineering Practice
Thesis Supervisor

Certified by .....

Asegun Henry
Robert N. Noyce Career Development Professor
Thesis Reader

Accepted by .....

Nicolas Hadjiconstantinou
Chairman, Department Committee on Graduate Theses

Electrochemically Mediated Molten Salt Processes for High Temperature CO_2 Capture and Conversion

By

Michael Philip Nitzsche

Submitted to the Department of Mechanical Engineering on August 13, 2021

in Partial Fulfillment of the Requirements for the

Degree of Master of Science in Mechanical Engineering

Abstract

In recent years, alkali carbonate molten salts have been developed as a medium for electrochemical conversion of CO_2 into value-added carbonaceous materials, including carbon nanotubes (CNTs). While electricity requirements are significant, the high economic value of CNTs make these processes potentially appealing both as a means of carbon sequestration and as an alternative to current greenhouse gas-intensive CNT synthesis pathways. Prior work in this field has primarily focused on the effects of parameters such as alternate chemistries, electrolyte additives, and electrode composition on the achievable products and energetic demands. This research has worked towards commercial operation of electrochemical CNT synthesis.

In this thesis, we present research advancing integration of electrochemical conversion of CO_2 in molten salts into real chemical processes at moderate temperatures (500-650°C). First, we examine molten alkali borates as a novel hybrid sorbent for CO_2 conversion. Alkali borates have been demonstrated as a promising high-temperature molten salt sorbent for acid gas separations, but prior studies have focused on regeneration through steam sweeping or thermal cycling. Here, we demonstrate that $Na_xB_{1-x}O_{1.5-x}$ with $x=0.75$ can be regenerated electrochemically, achieving CNT synthesis in the process. We determine an optimal mixture of borate/carbonate salts to maximize CO_2 uptake and coulombic efficiency. We then examine novel materials for containment of borates and demonstrate the effects of varying cathode materials on electrolysis. We also investigate potential synergies between carbonate electrolysis and the alkaline thermal treatment (ATT) process for conversion of oceanic biomass and plastic wastes into hydrogen. We perform preliminary investigations into the possibility of an all-in-one gasification/electrolysis reactor, determining that the presence of seaweed ash inhibits CNT synthesis, but LDPE can be gasified without affecting the electrochemistry. Finally, we present a technoeconomic analysis of the ATT process, evaluating the relative merits of both the originally proposed slag-regenerated ATT process and an electrochemically mediated alternative. We determine that variable operating expenses are prohibitive in most cases for a slag-regenerated system, making electrochemical regeneration attractive if practical concerns can be addressed.

Thesis Supervisor: T. Alan Hatton
Title: Ralph Landau Professor, Department of Chemical Engineering Director,
David H. Koch School of Chemical Engineering Practice

Thesis Reader: Asegun Henry
Title: Robert N. Noyce Career Development Professor

Acknowledgments

First and foremost, I am extremely appreciative of the support and guidance I received from my advisor, Dr. T. Alan Hatton. Professor Hatton has been a constant source of ideas, questions, and mentorship throughout my Master's.

I am also appreciative of the support and guidance I received from Dr. Asegun Henry, who provided mentorship through the first year of my master's and taught me a great deal about high temperature experimentation.

Thank you to Cameron Halliday for his mentorship throughout my time in the Hatton Group. His efforts to help me transition to the group dramatically lessened the learning curve I faced, and even after defending his Ph.D., he was always eager to help when I encountered challenges or interesting results. I cannot overstate how valuable it was to have him as a resource for all things related to alkali borate salts and high temperature carbon capture.

I am especially grateful to Dr. Lev Bromberg, whose insights truly challenged me to think critically and appreciate the science at the heart of our work. Lev's immense knowledge of chemistry was an incredible resource throughout my time in the lab, and his way of distilling broad research challenges to focus on key questions is something I will carry with me throughout my career.

I would also like to thank the collaborators I have had the pleasure of working with throughout this project, including Jonah Williams and Caspar Stinn, who made significant contributions to the work presented in Chapters 4 and 5 respectively.

Thank you to all of the members of the Hatton Group for providing me with support and guidance throughout my time in the lab. I learned an incredible amount about electrochemistry, science, and life in general from our daily interactions, and I am especially grateful to Kyle Diederichsen, Stephen Dewitt, Yayuan Liu, Seoni Kim, Jin Soo Kang, and Sebastien Schwaminger for helping me every day in the lab.

In the broader MIT community, I am grateful to Caleb Amy, Colin Kelsall, and Ethan Benderly-Kremen for providing invaluable advice in designing and safely operating bench-scale experiments at high temperatures.

Finally, thank you to my family for their unwavering support of all my endeavors. I am incredibly lucky to have parents and a sister who have encouraged me to follow my passions and try to make a difference with whatever I do.

Contents

List of Figures

1 Introduction

1.1 Motivation for CO_2 Capture

To mitigate the effects of climate change, it is imperative to reduce the emissions of greenhouse gases (GHG) to net zero as quickly as possible – the goals set by the 2015 Paris agreement target GHG neutrality by the mid-21st century to limit global warming to 1.5-2°C.[1] In 2019, global CO_2 emissions exceeded 37 gigatons.[2] While CO_2 accounts for the vast majority of GHG emissions by mass, trace GHGs including N_2O, CH_4, and fluorinated gases[3] are an order of magnitude more potent and raise this figure to the warming equivalent of 51 gigatons of CO_2 per year.

Decarbonizing human activities is a monumental undertaking, requiring a fundamental shift in how we as a society approach nearly all aspects of daily life, as shown in Figure 1-1. Economic pressures imposed by governing bodies which monetize the environmental costs of GHG emissions are increasingly incentivizing companies to develop sustainable alternatives.[4,5] The rapidly falling costs of non-CO_2 producing resources due to technological advancements in photovoltaics and wind power further incentivize the development of CO_2-free pathways over combustion-based energy.[6]

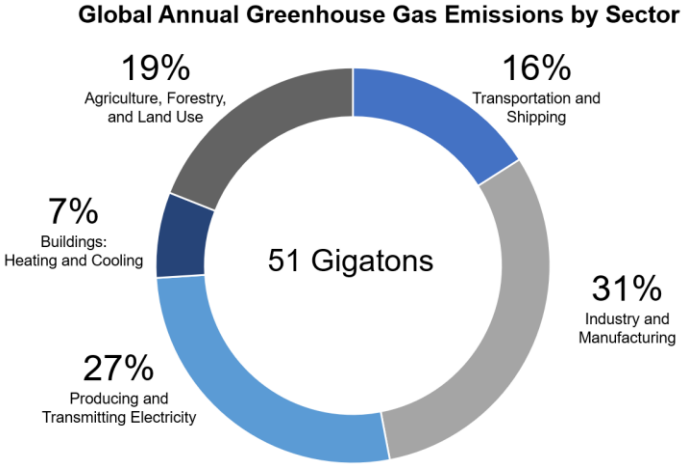

Figure 1-1: Global greenhouse gas emissions by sector, with data from[103]

Despite these trends, many industrial activities are ill-suited for decarbonization through renewable resources. Traditional rotary kilns and blast furnaces for production of metals and cement are seen as particularly expensive to substitute. This is both because of the high temperatures required, and because regardless of the heat source, large-scale processes such as the calcination of limestone ($CaCO_3$) to produce quicklime (CaO) in cement manufacturing or carbon-driven reduction of hematite (Fe_2O_3) to metallic iron in steelmaking are reliant on the thermodynamic driving force provided by the formation of CO_2. Combustion-free alternatives to other heat-intensive industrial processes like production of chemicals are similarly challenging. Even in applications that can be more readily decarbonized like electricity production, significant capital investments in fossil fuel plants with multi-decade lifespans make it economically desirable to continue operation if the associated GHG emissions can be mitigated. For these applications, it is therefore imperative to develop technologies for carbon capture and utilization/sequestration (CCUS). If CCUS technologies can be made cost-competitive at scale, they can enable continued

utilization of existing technologies and infrastructure while abating their associated environmental impacts.[7,8]

1.2 High Temperature Sorbents for CO_2 Separation

Modifications to industrial processes to capture their CO_2 emissions can take many forms. The overall process configuration can be redesigned to produce high-purity gas streams for sequestration or conversion, as in chemical looping combustion[9], oxy-combustion[10], and the Allam cycle.[11,12] The existing process can also be modified for post-treatment separation of acid gases using sorbents, membranes,[13,14] or phase manipulation.[15] In this work, we focus on sorbent-based separations.

In sorbent-based separations, materials with a conditional affinity for a given species (in this work, CO_2 or other acid gases) are used to selectively bind and remove that species from a mixed stream. The sorbent operating conditions are then altered, thermodynamically driving release of the bound species into a separate stream. In temperature-driven processes, thermal dependence of the binding equilibrium is used to vary capacity for a given species and drive uptake and release, typically absorbing at low temperature and desorbing at a raised temperature. The most common example of a thermally driven sorption process is amine-based acid gas scrubbing[16]. In pressure or concentration driven sorbent processes, chemical equilibrium conditions are unchanged between absorption and desorption, but desorption is driven by lowering the activity of the gas in question through vacuum or convective removal by an easily separable species like steam. This is widely employed in pressure-swing adsorption processes used to purify hydrogen in steam methane reforming.[17] Finally, variations in external electrical potential can be used to drive reactions in chemical sorbents. This can take the form of absorption/desorption in redox-active species like amines and quinones,[18] or can regenerate the sorbent by converting the absorbed species to a different molecule entirely, as in electroreduction of molten carbonates to form carbon and oxygen.[19] This space of commonly employed sorbent regeneration options is summarized in Figure 1-2.

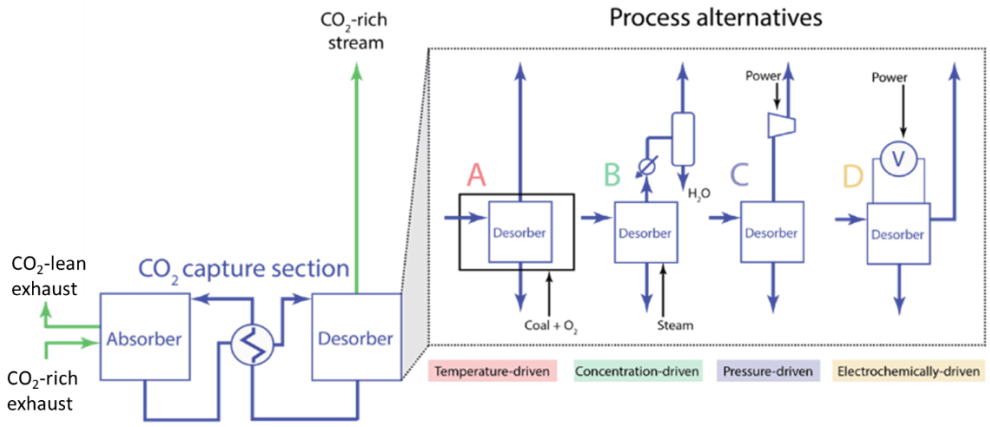

Figure 1-2: Regeneration process alternatives for CO_2 sorbent separations

In many applications involving the combustion of hydrocarbons, it can be advantageous to perform CO_2 capture with sorbents that operate at high temperatures (above 500-600°C). The

motivation for these high-temperature sorption processes is best explained via the diagram in Figure 1-3, depicting a typical combustion process with temperature-swing sorbent separation.

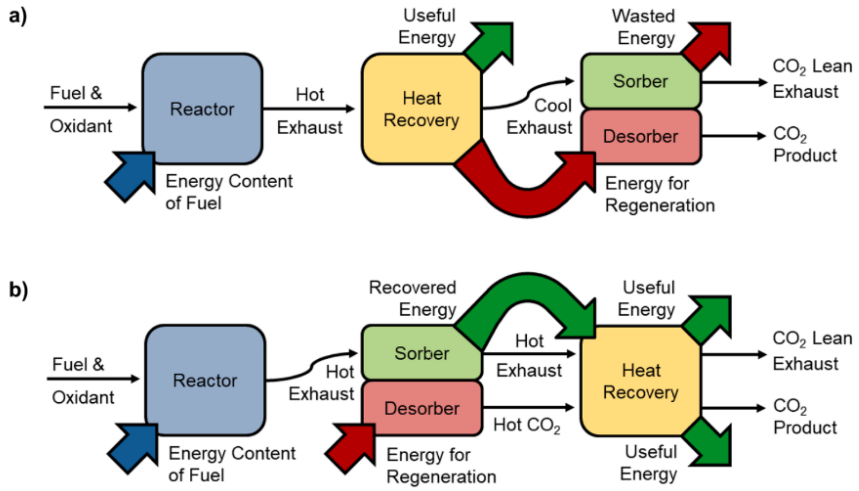

Figure 1-3: Block diagram comparing the energy flows associated with CO_2 sorption processes at (a) low and (b) high temperature, Adapted with permission from *Halliday, C. & Hatton, T. A. The potential of molten metal oxide sorbents for carbon capture at high temperature: Conceptual design. Applied Energy* ***280****, (2020). Copyright 2020 Elsevier Ltd.*[30]

In low temperature post-combustion CO_2 sorbent separation (Figure 1-3a), fuel and an oxidant (typically air) are mixed and combusted, and thermal energy is extracted from the outgoing stream to drive a process or produce electricity. The cool exhaust is then directed through a bed of lean sorbent, which exothermically binds the CO_2 and allows other gases like nitrogen to pass as CO_2-lean exhaust. The heat generated during binding at near-ambient temperature must be rejected to maintain equilibrium, and by Carnot's theorem cannot be used to generate energy due to its low grade. The CO_2-rich sorbent is then transferred for regeneration, here using thermal energy from elsewhere in the process to weaken the sorbent's affinity for CO_2 and release it as a purified stream.

The key difference in the high temperature alternative (Figure 1-3b) is that the heat of absorption is released at a useful temperature, and can then be used later on in the process rather than rejected as waste heat. Likewise, the sensible heat contained in the desorbed CO_2 can also be recovered at a high grade prior to liquefaction and export. In this manner, the contributions of sensible heating and the enthalpy of reaction to the energy penalty are greatly reduced, and the energy requirement approaches the entropy change of separating the species, or the thermodynamic minimum.[20]

A broad range of materials have been studied as potential CO_2 sorbents in high-temperature processes. The most extensively studied system of materials are those used in calcium looping, whereby fluidized solid particles are used to absorb CO_2 by thermally cycling between limestone ($CaCO_3$) and calcium oxide (CaO) according to the following reaction:[21]

$$CaCO_{3,(s)} \leftrightarrow CO_{2,(g)} + CaO_{(s)} \qquad \text{Eq. 1-1}$$

This chemistry has successfully been implemented at the pilot plant scale,[22] but challenges in particle sintering limit widespread adoption.[23] Due to morphological changes incurred during capture and release, the calcium particles aggregate over many cycles, gradually reducing their

CO_2 capacity and necessitating continuous purging and replenishment. The relative abundance of limestone makes this feasible, but continuous replenishment still imposes significant thermodynamic and economic penalties. Proposed solutions like mediators,[24] structural supports,[25] and nano-sized particles[26] increase costs and diminish the economic benefits offered by limestone's abundance.

Molten salts are liquid phase high temperature sorbents offering several advantages over solids, including high capacities, fast kinetics, and stable operation. Alkali carbonate salts (M_2CO_3, where M is an alkali metal) have been demonstrated as thermally-reversible CO_2 sorbents,[27] operating according to the temperature dependent reaction:

$$M_2CO_{3,(l)} \rightleftharpoons CO_{2,(g)} + M_2O_{dissolvd} \quad \text{Eq. 1-2}$$

However, the applications of carbonates as thermally-driven sorbents are limited due to the high required working temperatures for significant O^{2-} solubility (700°C-950°C) as well as their relatively low working capacities.

Molten alkali borates are a newly discovered class of molten salt acid gas sorbents, offering numerous advantages over other comparable materials. Alkali borate chemistries are typically denoted using a mixing ratio x, for $M_xB_{1-x}O_{1.5-x.}$ To maximize working capacity for CO_2, a mixing ratio of x=0.75 is adopted with equal quantities of sodium and lithium.[28] This ratio represents a triborate (BO_3) chemistry, chemisorbing CO_2 via[28]

$$4M_3BO_{3,(l)} + 3CO_{2,(g)} \leftrightarrow 3M_2CO_{3,(l)} + M_6B_4O_{9,(l)} \quad \text{Eq. 1-3}$$

The operating temperatures of these sorbents can be tuned by varying the chemistries, but a desirable working range of 550-700°C can be achieved for solid-to-liquid (Na_3BO_3) or fully liquid ($Na_{1.5}Li_{1.5}BO_3$) operating regimes. Importantly, this mechanism is strongly dependent not only on temperature but also on the partial pressure of CO_2. This enables high working capacities for near-isothermal desorption into steam sweep gas at a dramatically reduced thermodynamic penalty compared to traditional pressure or temperature swing processes.[29,30] Another significant advantage of borate salts is their capacity for other acid gases including NO_x, $SO_{x.}$, and H_2S, offering potential for all-in-one flue gas sweetening that would reduce overall system costs.[31]

While promising results have been achieved at the gram scale,[32] significant further research is necessary to determine the viability of alkali borates as a sorbent in a full-size operation. Alkali borates are exceptionally corrosive materials, oxidizing and dissolving most common metals and ceramics with the notable exception of platinum, a prohibitively expensive material for most applications.[33] The dissolution rate of nickel's stable oxide layer is sufficiently slow that it could feasibly be used to construct infrastructure, but corrosion would still represent a significant challenge, and it is unclear if a flowing liquid would exacerbate these issues. Handling of the resulting solids from capture of SO_x and H_2S is also an open challenge.

1.3 CO_2 Sequestration and Utilization

After CO_2 is captured, it must then be sequestered or utilized in a manner that prevents its atmospheric release. With current technologies, the most economical means of accomplishing

sequestration is by liquefying the CO_2 at 150 bar and transporting via pipelines for injection in underground facilities.[34] These facilities typically take the form of depleted oil and gas reservoirs, deep saline aquafers, or potentially deep ocean sites.[35] Liquefied CO_2 can also be used for enhanced oil recovery, displacing fossil fuels for more efficient extraction as it is injected for sequestration.[36] The availability of sites for CO_2 sequestration is inherently geographically limited. While the cost of liquefaction and sequestration of CO_2 is typically a fraction of the cost of its capture, in regions such as Japan with limited oil and gas reserves, the liquefied CO_2 must be shipped elsewhere for long-term storage, dramatically increasing the associated costs.[37] These geographic variations in sequestration site availability and associated costs provide additional motivation for on-site chemical conversion or utilization.

A complement to CO_2 sequestration is conversion or incorporation of CO_2 into usable chemicals or products. While not expected to deliver CO_2 emissions reductions at the same scale as sequestration, the higher geographic independence of CO_2 conversion and utilization as well as potential revenue streams from sale of CO_2-based products can make these options economically favorable in certain circumstances.[38] The chemical stability of CO_2 and the high hydrogen demands to produce many CO_2-based fuels and chemicals typically make options for direct employment more desirable when available. Opportunities for direct utilization of CO_2 can include enhanced oil recovery, supercritical solvents and working fluids, and enhanced plant growth.[38–40] While often energetically expensive, processes converting CO_2 into chemicals and fuels like polymers, methane, methanol, urea, and gasoline/diesel have been explored, as well as building materials that combine minerals or waste with CO_2. [41] Urea production from CO_2 is well-established as a large-scale industrial process, representing the largest single industrial consumer of CO_2. Among the upcoming conversion technologies, polymer production and building materials show high potential for near-term economic viability due to their thermodynamic favorability, as conversion of the stable CO_2 into CO_3^{2-} results in an even lower energy state. In chemical production, Fisher-Troph syntheses of hydrocarbons and electrochemical reduction of CO_2 to products like formic acid are also economically promising, but these technologies lack maturity.[39] It is also important to note that unlike mineralization, production of consumable hydrocarbons and chemicals from CO_2 tends to be carbon neutral, not carbon negative, as they are ultimately used in processes which re-emit the CO_2.

1.3.1 Electrochemical Conversion of CO_2 into Value-Added Carbons

A relatively recent development has been the use of molten alkali carbonate salt electrolytes to convert CO_2 into value-added carbonaceous products.[19,42–44] The working principle of these technologies involves reduction of carbonates to form oxygen and carbon according to the following generalized half-reactions, where M is an alkali metal:

$$(M_2)CO_{3,(l)} + 4e^- \rightarrow (M_2)O_{(dissolved)} + C_{(s)} + 2O^{2-}{}_{(dissolved)} \qquad \text{Eq. 1-4}$$

$$2O^{2-}{}_{(dissolved)} \rightarrow O_{2,(g)} + 4e^- \qquad \text{Eq. 1-5}$$

The system is then regenerated via the following uptake reaction:

$$M_2O_{(\text{dissolved})} + CO_{2,(g)} \rightarrow M_2CO_{3,(l)} \qquad \text{Eq. 1-6}$$

The overall reaction stoichiometry can therefore be represented as:

$$CO_2(g) \rightarrow C(s) + O_2(g) \qquad \text{Eq. 1-7}$$

The morphology and dopants of the resulting carbon product are determined by the composition of the electrolyte, choice of electrode materials, and to a lesser extent the current density of the electrolysis process. While electroreduction of CO_2 in sodium and potassium salt chemistries generally results in low-value amorphous carbon, lithium carbonates and lithium-rich eutectics can be used to produce more valuable products ranging from nano-onions and graphene[45,46] to multiwalled carbon nanotubes (CNTs) of varying thickness, length, and levels of entanglement,[43] as shown in Figure 1-4. Salt additives in small (<10 mol% or weight%) quantities such as calcium metaborate ($CaBO_2$), alkali nitrates ($(M)NO_3$) or alkali sulfates ($(M_2)SO_4$) can also be used to add dopants to the nanotubes, modifying their chemical and electrical properties.[47,48]

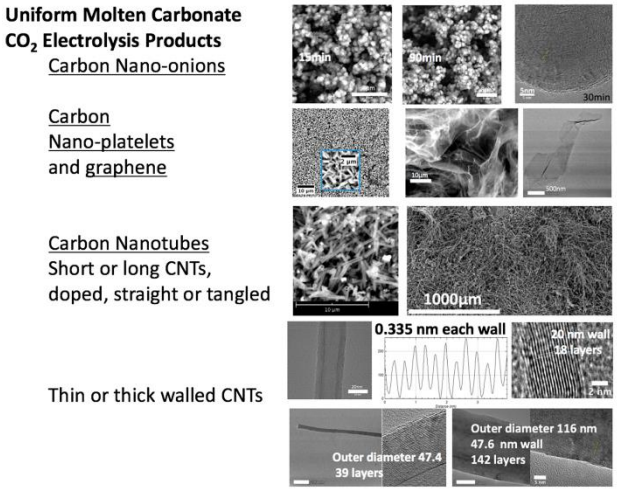

Figure 1-4: A selection of achievable products obtainable via electroreduction of CO_2 in carbonate salts, adapted with permission from Ren, J. et al. Recent Advances in Solar Thermal Electrochemical Process (STEP) for Carbon Neutral Products and High Value Nanocarbons. Accounts of Chemical Research **52**, (2019). Copyright 2019 American Chemical Society

Among these potential products, carbon nanotubes are by far the most valuable, and most research in this field is tailored towards development and optimization of pathways for their production. A factor hypothesized to be significant in achieving CNTs rather than onions and platelets is the presence of transition metals in the melt to act as catalysts for nucleated growth. This is most easily achieved through careful selection of the electrodes. Traces of nickel oxide donated by a nickel anode and zinc oxide donated from galvanized steel cathodes have been shown to achieve this effect, as has addition of small amounts of zinc oxide directly to the melt.[49] Kinetics have also been shown to have a significant influence on the morphology of the carbon product obtained.[50] Assuming equal active surface area across electrodes, the kinetically limiting step in the overall reaction is the evolution of oxygen at the anode. For a given stainless steel cathode and fixed current density, materials such as nickel or platinum that act as effective catalysts for O_2 evolution were shown to promote nucleated carbon growth into ordered materials, whereas poor catalysts like copper will favor amorphous carbon deposition.

Materials selection and operating conditions are important not only for controlling carbon morphology, but also for avoiding undesirable side reactions. Depending on the materials used, at higher temperatures molten carbonate electrolysis begins to favor CO production[51] according to the following modified reactions:

$$(M_2)CO_{3,(l)} + 2e^- \rightarrow (M_2)O_{(dissolved)} + CO_{(g)} + O^{2-}{}_{(dissolved)} \quad \text{Eq. 1-8}$$

$$\frac{1}{2}O^{2-}{}_{dissolved} \rightarrow \frac{1}{2}O_{2,(g)} + 2e^- \quad \text{Eq. 1-9}$$

In lithium carbonate (Li_2CO_3), CO evolution predominates above 850°C, but this reaction can become a concern at lower temperatures, particularly when employing graphite as a cathode material. This reaction pathway can be targeted intentionally for syngas applications, but is generally an engineering constraint on system design. More common side reactions include co-deposition of alkali metals at high applied potentials, which is more favored for potassium and sodium than lithium.[19]

The energetic requirement of this molten salt electrolysis process is quite high compared to other means of CO_2 conversion and utilization– the incoming CO_2-rich stream must be heated to the operating temperature of the salt if not employed in typical use-cases for high temperature sorbents, and the operating voltage of this 4-electron reaction is typically on the order of 0.8V-2V, leading to a high electricity requirement of approximately $360/ton of CNTs ($50/ton CO_2) at optimal conditions with electricity at $0.05/kWh.[52] It is important to note that there are fundamental differences between this process and other CO_2 conversion pathways. CO_2-based chemical syntheses are typically thermodynamically unfavorable compared to their traditional synthesis pathways, relying on CO_2 pricing and the rapid decline in electricity costs for potential economic viability in spite of increased energy requirements. State-of-the-art methods for carbon nanofiber and nanotube production including electrospinning, chemical vapor deposition,[53] and arc/plasma techniques[54] can be 1-2 orders of magnitude more electricity intensive than carbonate electrolysis,[55] so here the CO_2-based pathway is energetically preferable if the desired morphologies can be obtained. While electrolytic production of CNTs cannot replicate the precision achievable with other processes (single walled nanotubes of highly controlled alignments or contiguous, macroscopic length scales are currently valued on the order of $100/g), the randomly oriented multiwalled nanotubes obtained via carbonate electrolysis are comparable to those obtained via CVD, which are still highly valuable on the order of $100-300/kg.[53] These multiwalled nanotubes can be suitable for large-volume applications including battery electrodes and additives, composite materials, conductive inks, and photovoltaics.[56]

1.3.2 Challenges and Opportunities in Electrochemical Conversion of CO_2 into Carbon Nanotubes

Molten salt technologies for converting CO_2 into value-added carbons have been demonstrated extensively at the bench scale, but significant research is still necessary to continue understanding and optimizing chemical mechanisms and to enable full-scale operation.

Pumping of molten carbonates has been demonstrated extensively at scale for concentrated solar power plants,[57] but challenges remain in developing technologies for continuous removal of the CNT product. Depending on acids and other chemicals required for purification, carbon emissions

associated with post-processing of value-added carbons can easily exceed those mitigated by sequestration of CO_2 in them. Loss of the lithium-rich working fluid can also adversely affect the economic viability of these processes. Studies involving high-temperature press filtration have been conducted to resolve this issue, but are still in progress.

To minimize energy expenditure, carbonate electrolysis processes should ideally be incorporated in similar use-cases to other high-temperature sorbents, where CO_2 can be captured at high temperature to minimize sensible heating requirements. Potential synergies between carbonate electrolysis and high temperature applications (>750°C) like cement manufacturing have been explored extensively.[58,59] The use of such sorbents in moderate temperature processes (~500-600°C) such as power generation from coal or biomass is more challenging because of the low working capacities associated with low solubility of oxide species in carbonates in this temperature range.[60] The use of alkali borates as oxide mediators could provide one possible means to expand the working capacity of electrochemically-mediated salt sorbents in this temperature range.[61,62] Another unexplored use case is cyclic processes involving carbonates such as alkaline thermal treatment, as additional value can be extracted from the calcined salt in cyclic operation. In this process, the formation of hydroxides could potentially be used to lower working temperatures. The goal of this thesis is to investigate the potential synergies and challenges associated with integrating carbonate electrolysis into mid-temperature processes in this manner.

1.4 Motivation for Molten Alkali Borates as Electrochemically Mediated CO_2 Sorbents

Several studies have shown that the addition of borates to carbonate electrolytes can be used to modify properties and morphology of carbonaceous products, as well as to enhance the yields and selectivity of electrochemical reactions. Addition of 5-10% lithium metaborate ($LiBO_2$) to Li_2CO_3 has also been shown to add boron dopants to the resulting carbon nanotubes, increasing their electrical conductivity tenfold,[47] and addition of 7.7% calcium metaborate ($CaO{\cdot}B_2O_3$) to Li_2CO_3 was shown to produce thin-walled boron-doped carbon nanotubes with a high Coulombic efficiency.[48] Addition of ~1.25% $LiBO_2$ to LiCl-Li_2CO_3 electrolytes was shown to allow selectivity of 90% between CO and CNTs, and to reduce electrolysis energy consumption by up to 40%.[61,62] The hypothesized mechanism for these improvements is regulation of O^{2-} species via the following mediating reactions:

$$BO_2^- + O^{2-} \rightleftharpoons BO_3^{3-} \qquad \text{Eq. 1-10}$$

$$BO_3^{3-} + CO_2 \rightleftharpoons CO_3^{2-} + BO_2^- \qquad \text{Eq. 1-11}$$

The impacts of this buffering mechanism can be explained by examining the cathodic Nernst potentials for CO_3^{2-} electroreduction into C and CO (vs Li/Li^+) reported by Hu et. al.[61] at 550°C:

$$E_{CO} = 0.95 - \frac{RT}{4F}(2ln[O^{2-}] + ln[CO] - \ln[CO_3^{2-}]) \qquad \text{Eq. 1-12}$$

$$E_C = 1.25 - \frac{RT}{4F}(3ln[O^{2-}] - \ln[CO_3^{2-}]) \qquad \text{Eq. 1-13}$$

From these equations, two key insights can be drawn: high local activities of O^{2-} anions minimize the energy required for electrodeposition of carbon, and at sufficiently low O^{2-} activities, CO evolution becomes thermodynamically favored due to the difference in O^{2-} dependence. Through the BO_2^-/BO_3^{3-} buffering mechanism, the activity of the oxide anions can be tuned, improving mass transport and availability at low temperatures where solubility would otherwise be low, and reducing O^{2-} activity at high temperatures where solubility is high and CO evolution is desired.

While borates have been explored as additives to molten alkali salt carbonate media at low additive concentrations in carbonate media (<10 mol% borate), there are no reported studies using borates as the primary medium for CO_2 electroreduction. The work of Harada et. al suggests that alkali borates ($M_xB_{1-x}O_{1.5-x}$, where M represents alkali metal species) can be used to chemisorb CO_2 according to the following reversible mechanism.[63]

$$4M_3BO_3 + 3CO_2 \leftrightarrow 3M_2CO_3 + M_6B_4O_9 \qquad \text{Eq. 1-14}$$

This formation of carbonate and metaborate from CO_2 and borate (Eq. 1-14) with the subsequent formation of carbonate anions ($M_2CO_{3(molten)} \leftrightarrow 2M^+ + CO_3^2$) fulfill the pre-requisite for the electrochemical conversion of CO_2 to carbon via:

$$Li_2CO_{3(liquid)} \rightarrow C_{(CNT)} + Li_2O_{(dissolved)} + O_{2(gas)} \qquad \text{Eq. 1-15}$$

This suggests that the same uptake and electroreduction of CO_2 can be performed using triborates as a starting medium.

Electrolytes primarily composed of alkali borates could offer several potential advantages over traditional carbonates. The solubility of CO_2 in carbonate-based electrochemical sorbents below 750°C is limited by the low solubility of M_2O, as the presence of M_2O is a pre-requisite for the absorption of CO_2 in carbonate:

$$M_2O_{(dissolved)} + CO_{2_{(dissolved)}} \leftrightarrow M_2CO_{3_{(l)}} \qquad \text{Eq. 1-16}$$

However, the potential of the triborate anions to enhance the CO_2 solubility (Eq. 1-11) suggests that high concentrations of borates could alleviate these issues by absorbing or releasing O^{2-} anions as needed. Furthermore, the reversibility of the mechanism in Eq. 1-14 indicates that a borate-based chemistry could allow operation as a sorbent or as an electrolyte. In scenarios with variable electricity costs where CO_2 capture is desired, having steam or temperature-swing based desorption as available options could allow for grid matching or multiple desorption steps for maximizing working capacity. For example, in a power grid heavy in solar resources, CO_2 could be converted into high-value carbon nanotubes during the day when electricity is inexpensive and desorbed via a steam sweep gas for liquefaction and sequestration at night.

While borates alone can theoretically act as a starting medium for CO_2 electrolysis, the addition of carbonates could offer significant benefits to the electrochemical properties of the molten salt. The addition of carbonates is closely analogous to increasing the mixing ratio x for a given borate salt composition $(Na_aK_bLi_c)_xB_{1-x}O_{1.5-x}$. The value x=0.75 was found to optimize the working capacity, as it represents a triborate stoichiometry (M_3BO_3) and allows the full melt to utilize the reversible working mechanism given in Eq. 1-10. For mixing ratios exceeding x=0.83,

the borate melt becomes more closely analogous to an oxide solution, absorbing CO_2 according to the additional mechanism presented in Eq. 1-16.

The addition of metal oxides directly to the borate melt can cause processing problems due to the issues with metal oxide calcination and high temperatures required for such dissolution. The presence of metal oxides lowers the borate's working capacity as a concentration- or temperature-driven sorbent, but increases the overall sorption capacity for CO_2.[28] Therefore, the addition of carbonate to borates (or increase in mixing ratio x) represents a tradeoff between relative working capacity and overall availability of the CO_3^{2-} anion for electrolysis. By tuning this ratio, we herein hoped to achieve an optimal value maximizing CO_2 uptake capacity and coulombic efficiency.

Through these studies, we aim to determine if alkali borates can be used as a standalone medium for CO_2 electroreduction, to address challenges in materials compatibility, and to determine if an optimal carbonate/borate mixing ratio exists for electroreduction of CO_2 to value-added carbonaceous products.

1.5 Alkaline Thermal Treatment and Potential for Electrochemical Mediation

A recent paper by the Park group at Columbia University details an Alkaline thermal treatment process (ATT), whereby hydrocarbons in organic material (here, seaweed) are gasified through a reaction with alkali hydroxide salts to produce hydrogen.[64] This is exemplified through the following nominal cellulose exothermic reaction (ΔH=-629.2 kJ/mol), taking place at 500°C:

$$C_6H_{10}O_5 + 12NaOH + H_2O \rightarrow 6Na_2CO_3 + 12H_2 \qquad \text{Eq.1-17}$$

While further study is necessary to understand the exact mechanisms at play, the key to this process is hypothesized to be the alkalinity of the molten salt. It is analogous to paper pulping, where concentrated NaOH is used to break down cell walls, cell fibers, and glycoproteins to access the underlying sugars and hydrocarbons. This paper represents a significant advancement, both for its high relative conversion efficiencies compared to other biomass gasification processes, and because the process has synergy with seaweed, which is abundant but typically undesirable for biomass applications due to its high water and salt content. Preliminary results suggest that this process can be used for gasification of common plastic wastes such as LDPE – if this generalizes, alkaline thermal treatment could offer a promising avenue for treatment of biomass-contaminated ocean surface plastics, which cannot currently be recycled or gasified cost-effectively through traditional means. The Alkaline Thermal Treatment Process[65] outlined by Zhang et. al. is presented in Figure 1-5.

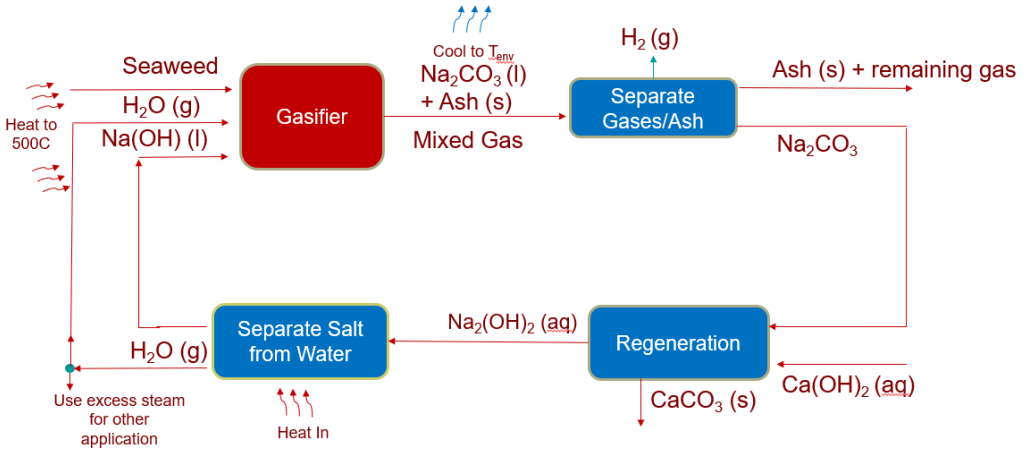

Figure 1-5: Base configuration of the Alkaline Thermal Treatment Process for hydrogen production from oceanic biomass, as described in[64]

A more extensive description of each of the unit operations this process entails is presented in Chapter 4. A key observation is the method of regeneration proposed. Sodium carbonate is cooled to room temperature and introduced into a slaked lime (CaOH) solution, where the following metathesis reaction is used to regenerate caustic soda (NaOH):

$$Ca(OH)_2(s) + Na_2CO_3(aq) \leftrightarrow 2NaOH(aq) + CaCO_3(s) \qquad \text{Eq. 1-18}$$

This can either be accomplished in a closed loop configuration by calcination of the resulting limestone ($CaCO_3$) as is done in calcium looping, or in an open loop system by consuming steel slag rich in CaO. In either case, significant thermodynamic penalties are imposed by cycling the salt between ambient temperature and 500°C, as well as by the separation of caustic soda from the regeneration solution. Generalizing to any alkaline hydroxide/carbonate chemistry, a potential alternative would be to reduce the carbonates electrochemically via the same mechanism described earlier:

$$M_2CO_{3(liquid)} \rightarrow C_{(s)} + M_2O_{(dissolved)} + O_{2(gas)} \qquad \text{Eq. 1-17}$$

Such a method is advantageous because the system could potentially operate near isothermally – neglecting thermal leakage, the only significant heat inputs required are preheating of the seaweed and steam. If a lithium-rich salt is selected, this solid carbon could feasibly take the form of nanotubes, increasing the recoverable value. This thesis aims to evaluate the feasibility as well as the advantages and challenges of electrochemical regeneration in the ATT process, both experimentally and through technoeconomic analysis.

1.6 Thesis Objectives and Outline

The objective of this thesis is to examine molten alkali borates as a potential medium for capture and electrolysis of CO_2, and to examine potential synergies between CO_2 electrolysis and industrial processes like the alkaline thermal treatment process.

1. Chapter 1, we discussed the motivation for development of high temperature acid gas sorbents, particularly those capable of serving as a medium for electrochemical reduction of CO_2.

2. In Chapter 2, we briefly investigate corrosion in novel materials to explore further the potential space of metals and ceramics for use as construction materials and electrodes. Thermogravimetric analysis is utilized to measure the CO_2 working capacity of alkali borates in contact with materials of interest, checking for declines indicative of corrosion and dissolution into the salt. We eliminate tantalum and tungsten as potential candidate materials, and suggest further study is necessary to determine if zirconia or yttria-stabilized zirconia could be used to contain borates in long-term operation.
3. In Chapter 3, we investigate the possibility of using molten alkali borates and alkali borate/carbonate mixtures as hybrid sorbents for capture of acid gases and electroreduction of CO_2. We develop a setup and procedural framework for electrolysis at high temperature under a controlled atmosphere and product recovery. We then examine the thermochemical properties of a novel carbonate/borate chemistry and demonstrate the effects of carbonate/borate loadings on carbonate electroreduction, determining a 1:3 molar ratio of the borate and carbonate salts to be optimal. Finally, the effects of varying cathode materials such as nickel and 316 stainless steel are investigated.
4. In Chapter 4, we experimentally investigate the possibility of combining alkaline thermal treatment with electrochemical synthesis of carbon nanotubes. First, we conduct a parametric study evaluating the coulombic efficiency of CNT synthesis in carbonate/hydroxide salts. Then, we conduct a series of experiments examining the effects of a simulated ATT process for treatment of biologically contaminated ocean plastics under nitrogen on salt electrolysis. We show that LDPE gasification does not inhibit CNT formation, but the presence of seaweed ash results in electrodeposition of amorphous carbon. We conclude that an electrochemically mediated ATT process would need to occur in multiple steps, with intermediate ash removal.
5. In Chapter 5, we present a technoeconomic analysis comparing alkaline thermal treatment processes regenerated both via slag and electrochemically. Cost estimates for capital expenses, variable and fixed operating expenses, and feedstock costs are developed for a nominal ATT plant with heat recovery and compared to the DOE Target Metrics for oceanic-derived biomass. We show that the baseline alkaline thermal treatment process using slag regeneration can meet targets for capital, feedstock, and fixed operating expenses, but variable operating expenses are prohibitive under most circumstances due to the cost of slag and thermodynamic penalty of regeneration. Next, we modify this model to examine a potential case using electrochemical regeneration, co-producing carbon nanotubes. The costs and revenues associated with electrolysis of carbon nanotubes dominate the system, but this configuration holds promise if practical considerations can be addressed.
6. Chapter 6 discusses conclusions and avenues for future work.

2 Continued Exploration of Candidate Materials for Alkali Borates

The exceptional oxidizing capabilities of alkali borate salts make them an ideal candidate for acid gas capture. However, these same chemical properties also make them exceptionally corrosive. Lithium tetraborate in particular is known to be an exceptionally corrosive liquid and strong solvent of oxides, as it is employed extensively in industry as a flux to dissolve rocks, minerals, ores, metal oxides, and metals for spectrochemical analysis.

Halliday et. al. conducted an extensive study on the compatibility of $Na_xB_{1-x}O_{1.5-x}$ and $(Na_{0.5}Li_{0.5})_xB_{1-x}O_{1.5-x}$ with common high-temperature working materials.[33] It was found that the working capacity of the alkali borates declines as substrate molecules are associated into the melt, enabling the use of thermogravimetric analysis and CO_2 breakthrough curves as an indirect means of probing materials interactions. Further analysis was also conducted using scanning electron microscopy, x-ray diffraction, and inductively coupled plasma-mass spectrometry. Through their work, it was determined that platinum is nearly inert with respect to alkali borates. Among non-precious metals, nickel was identified as a strong candidate material due to its protective oxide layer, with an estimated corrosion rate on the order of 0.5 mm/year for oxidized nickel 200/201. Inconel showed dramatically reduced performance compared to high purity nickel 200/201. Metals and metal alloys including 316 stainless steel, titanium, nickel-chromium were shown to oxidize and dissolve too quickly for long-term practical application (on the order of years or decades), and common ceramics including alumina and quartz were shown to dissolve and drive the working capacity to 0 almost instantly.

Several additional candidate high-temperature materials were hypothesized in Halliday's dissertation but not tested due to time constraints, including metals like tungsten, and tantalum, as well as zirconia and yttria-stabilized zirconia ceramics. These materials were screened using a similar thermogravimetric analysis procedure to explore other possible electrode or containment options prior to this study. $Na_xB_{1-x}O_{1.5-x}$ with x=0.75 was shown to be more corrosive than the sodium-lithium eutectic due to the higher operating temperatures required, and was used for this study.

2.1 Sample Preparation

Sodium hydroxide (NaOH, 97%) and boric acid (H_3BO_3) were purchased from Sigma-Aldrich. Powders in the proper mixing ratio were dissolved in deionized water, which was then evaporated at 120C overnight before an additional 2 hours of drying at 400°C to precipitate the desired Na_3BO_3.

2.2 Experimental Setup and Methodology

The cyclic uptake and release of CO_2 by the borate sorbent was measured by thermogravimetric analysis (Q-50, TA Instruments) on a platinum pan in the presence of the other material of interest. The capture and release of CO_2 results in a sample weight change, which can be converted to a CO_2 loading expressed in mmol/gram of sorbent. Sample weights were on the order of 8-12 mg of Na_3BO_3, with excess of each material added to the base. The experimental procedure was modelled after that used by Halliday et. al.[33] consisting of a ramp to 800°C and then isothermal

conditions for an hour under pure nitrogen. The temperature was then reduced to 700°C, and purge conditions were alternated between 100% N_2 and 20% CO_2 at 30-minute intervals over 20-100 cycles. Unless stated otherwise, the gas purge rate was 60 cubic centimeters/minute, and the weight of the pan and non-borate material is zeroed out during calibration.

2.3 Results

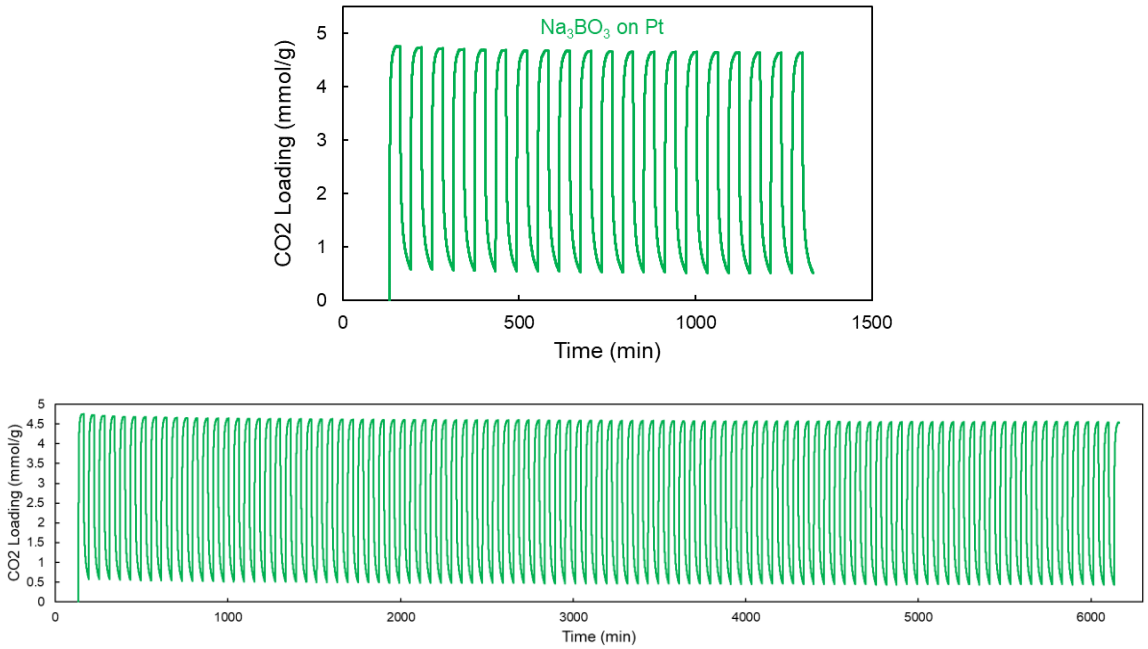

Figure 2-1: Control Experiment- Absorption Performance of Na_3BO_3 on Pt for the first 20 cycles and the full 100 cycles between 20% CO_2 and 100% N_2 at 700°C

To establish a baseline, a 6.4 mg sample (4.8 mg after pre-treatment) from this batch of Na_3BO_3 was tested alone on the platinum pan, as shown in Figure 2-1. No degradation was observed, and a stable working capacity of 4.1 mmol/g was achieved for 100 cycles.

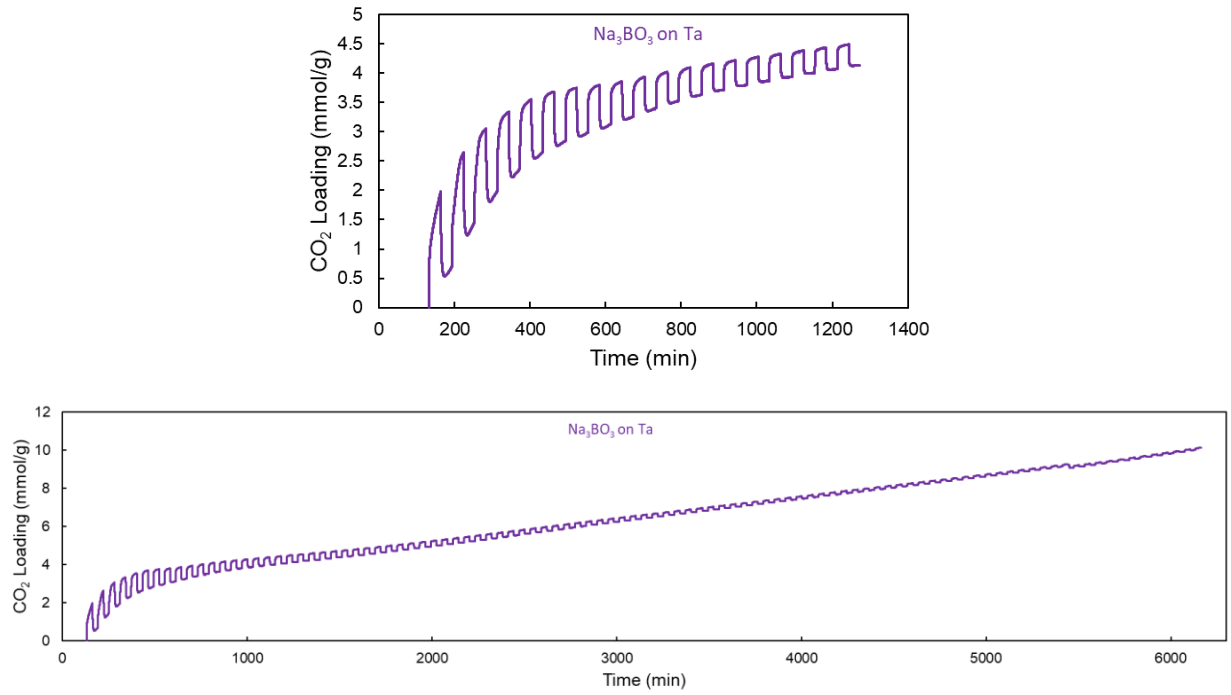

Figure 2-2: Absorption Performance of Na3BO3 on Tantalum foil for 20 cycles and the full 100 cycles between 20% CO_2 and 100% N_2 at 700°C

Next, 10.01 mg of salt was loaded onto tantalum foil (Sigma Aldrich, ≥99.9%) and tested for 100 cycles, shown in Figure 2-2. Two trends can be observed throughout the run. The average weight of the sample continuously increases, indicating that the tantalum foil is being oxidized by the CO_2 at these temperatures. While tantalum is commonly employed as a corrosion-resistant material due to its high melting point and the exceptional stability of its TaO_z suboxide surface layer, experiments by Bouzouita et. al. suggest that non-protective Ta_2O_5 is formed above 700°C. This mechanism could contribute to the continuous weight increase observed in this trial[66].

A rapid decline in working capacity is also observed over time, suggesting that the resulting Ta_2O_5 is readily dissolved by the borate melt. This indicates that tantalum is not a suitable construction material.

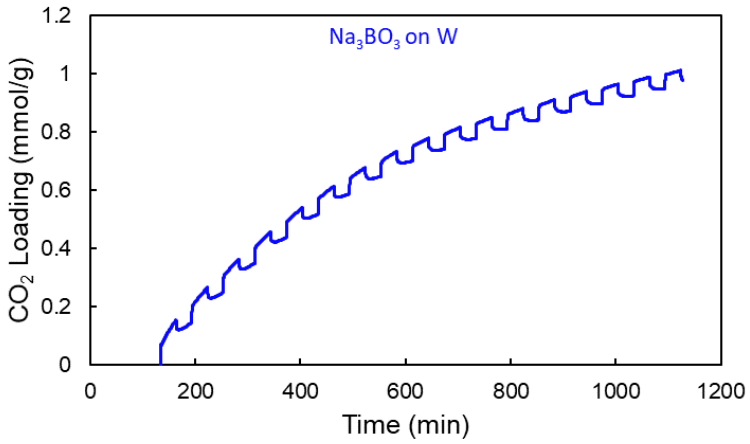

Figure 2-3: Absorption Performance of Na_3BO_3 on Tungsten foil for 20 cycles between 20% CO_2 and 100% N_2 at 700°C

In a 20-cycle trial on tungsten foil, it is again observed that the weight increases with time, indicating tungsten oxidation by the CO_2. While the working capacity is nearly constant, it is reduced by more than an order of magnitude compared to Na_3BO_3 on Pt. 24.7 mg of salt were used in this experiment rather than 5 on Pt. This difference in mass could possibly contribute to the lower working capacity due to mass diffusion effects, but the reduction observed far exceeds any expected geometric effects. The sample was also visibly extremely corroded after testing, indicating that tungsten can also be eliminated as a candidate material.

In addition to the metals tested above, zirconia and yttria-stabilized zirconia were also suggested as possible ceramic alternatives, shown below.

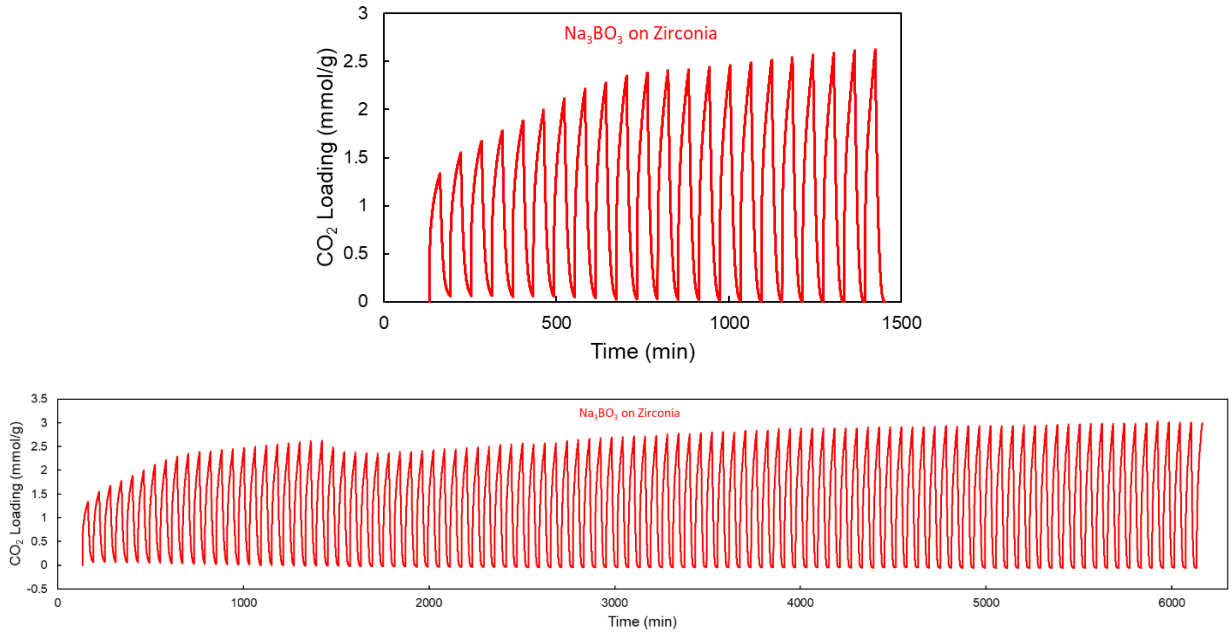

Figure 2-4: Absorption Performance of Na_3BO_3 with powdered zirconia for the first 20 cycles and a full 100 cycles between 20% CO_2 and 100% N_2 at 700°C

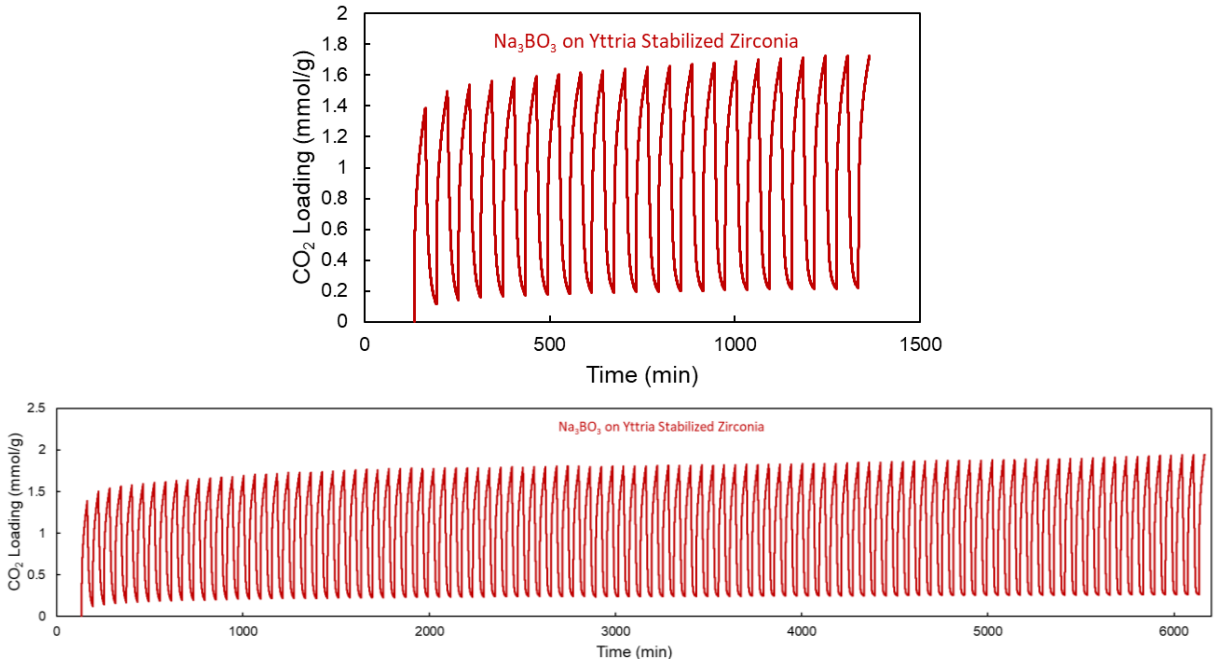

Figure 2-5: Absorption Performance of Na_3BO_3 with powdered yttria-stabilized zirconia for 20 cycles and 100 cycles between 20% CO_2 and 100% N_2 at 700°C

The zirconia (ZrO_2) and yttria-stabilized zirconia (YSZ) experiments were conducted using 8.06 and 8.33 mg of molten salt respectively (measured after 1-hour pre-treatment at 800°C). The average weight of both samples is relatively constant with time, indicating no retention of N_2 or CO_2. The working capacity of Na_3BO_3 on ZrO_2 fluctuates substantially, varying between 1.4 mmol/g and 3 mmol/g. The working capacity of Na_3BO_3 on YSZ is more stable, varying between 1.28 mmol/g and 1.68 mmol/g. It should be noted that the working capacity in both samples actually increases over time rather than showing the rapid decline in performance displayed on incompatible substrates like tantalum. However, the working capacity is noticeably reduced, never achieving the 4.1 mmol/g obtained during the control experiment (25% and 60% reductions for ZrO_2 and YSZ, respectively).

From these data alone, it cannot be conclusively determined whether this reduction in working capacity is due to geometric effects or chemical interactions with the ceramics. As the borate salt intermixes with the ZrO_2/YSZ powders, the exposed area could be reduced, hindering uptake. Expansion and contraction upon CO_2 uptake and release could move the ceramic particles, changing the geometric contribution and resulting in some of the early fluctuations observed in ZrO_2. It is also possible that the ZrO_2 and yttria are only slightly soluble in the Na_3BO_3, contributing to the reduction in working capacity shown.

It is important to note that this cyclic approach cannot be utilized to affirm that the materials in question are inert with respect to the salt – the value of this approach is in eliminating potential options that display rapidly declining working capacities. Because the mass of substrate material is intentionally very large compared to the mass of the salt, these studies do not offer insight into edge cases where the material is only slightly soluble, but could experience significant corrosion in a larger bath of borate salt. Further study in the form of ICP and XRD is needed to determine whether zirconia and yttria-stabilized zirconia are viable candidates for long-term borate containment.

3 Capture and Electroreduction of CO_2 Via Eutectic Molten Alkali Borates

3.1 Bench-Scale Experimental Setup and Procedure

In order to perform the desired electrolysis experiments in a controlled temperature/gas environment, a custom tube furnace setup was designed and constructed, shown below.

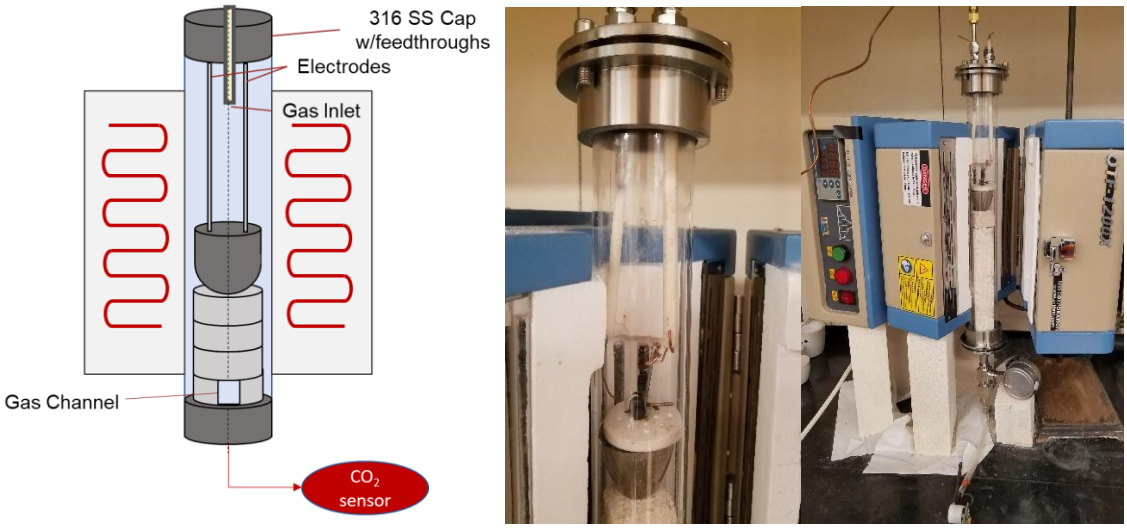

Figure 3-1: Depiction and photographs of experimental setup used for electrolysis in this work

The furnace is an MTI OTF-1200X rotated for a vertical tube, and the quartz glass tube, steel endcaps, alumina feedthroughs, and pressure regulator were also sourced from MTI. Alumina firebricks were cut to size with a gas channel in the bottom and used to support the crucible inside the tube. A GasLab GC-0016 sensor was used to monitor outlet CO_2, and a Bio-Logic SAS SP-150 potentiostat was used for all electrochemical measurements.

3.1.1 Experimental Procedure Development

Size restrictions prevent perfect sealing of the glass tube, requiring overpressure to prevent backflow and making vacuum pumping and backfilling infeasible. The constrained dimensions of the crucible also make bubbling of gas into the salt infeasible, introducing kinetic uncertainties. Through the following calculations, we ensure that in spite of these limitations, experimental conditions should still allow the desired release and uptake of CO_2 prior to electrolysis in lean and rich conditions.

Initial Headspace

The glass tube housing is 450 mm long with a 44 mm inner diameter, for a total volume of 684 cubic centimeters. Discounting spatial effects and the volume occupied by the ceramic stand and crucible, at a flow rate of 50 cubic centimeters per minute, the entire volume of the glass tube should be replaced every 13.7 minutes. Therefore, the system is sealed and purged with Nitrogen for 2 full exchanges (30 minutes) prior to heating to eliminate most of the oxygen and CO_2 present. This flow creates an overpressure in the system, preventing backflow of ambient air into the tube. During the 75-minute heating process, at least 45 minutes are spent below temperatures that would

allow oxidation of the cathode/anode or CO_2 uptake by the salt, allowing further purging in a nonreacting environment.

CO_2 Availability

The maximum CO_2 capacity of $(Na_{0.5}Li_{0.5})_xB_{1-x}O_{1.5-x}$ for the optimal x=0.75 mixing ratio relative to the capacity at 800C in pure N_2 is approximately 7.5 mmol/g [28]. For the 20 grams of salt used in a typical experiment, this represents a CO_2 capacity of 150 millimoles. Assuming an ideal gas at room temperature where the gas flow controller operates, 50 cubic centimeters per minute of CO_2 converts to 2 millimoles per minute. Stoichiometrically, enough CO_2 has been added to the tube to achieve full uptake after 73 minutes, so CO_2 is purged for more than double this timescale (3 hours, or 180 minutes) prior to electrochemical interaction to ensure full uptake.

The high uptake of the salt and small gap between the crucible and tube wall (40 mm diameter crucible vs 44 mm inner diameter tube) generally prevent detection of CO_2 by the sensor during experimental operation. However, in control experiments with the same ceramic feedthroughs in place and the furnace engaged with no crucible present, the CO_2 is detected at the outlet near 100% quantities by the end of the first full exchange (15 minutes), indicating that all of the CO_2 is at least impinging on the salt before leaking from the top of the tube, likely through gaps surrounding the ceramic feedthroughs.

CO_2 Uptake Kinetics

Bubbling gases into the salt is infeasible in this experimental design due to spatial constraints, so therefore any absorbed CO_2 must be captured at the surface and allowed to diffuse into the salt. Halliday et. al. calculated CO_2 diffusion coefficients on the order of 10^{-9}-10^{-7} m^2/s for the borate salt in question[28]. As a simplified approximation, we take a characteristic length scale as the depth of the coiled cathode (1 cm) and find the corresponding timescale for the diffusion coefficient at 550°C (estimated at 9.6×10^{-9} m^2/s)

$$\frac{dC}{dt} = D\frac{d^2C}{dx^2} \rightarrow \frac{\Delta C}{\Delta t} \approx D\frac{\Delta^2 C}{\Delta x^2} \rightarrow \Delta t \sim \frac{1}{D}\Delta x^2 \qquad \text{Eq. 3-1}$$

$$\Delta t \sim \frac{1}{9.6 * 10^{-9}} \times (0.01)^2 = 10416\ sec\ = 2.89\ hours$$

This is consistent with the 3 hours of CO_2 equilibration allowed after switching from N_2 to CO_2.

3.1.2 Procedure Summary

Unless specified otherwise, the overall procedure followed in the electrolysis experiments in this chapter consists of the following steps:

1) Sample Preparation

To produce the desired borate salt, sodium hydroxide (NaOH, 97%), lithium hydroxide (LiOH 99%) and boric acid (H_3BO_3, 99%) were purchased from Sigma-Aldrich. Powders in the proper mixing ratio were dissolved in deionized water and allowed to neutralize. The resulting solution was then evaporated at 120°C overnight (16 hours) before an additional 2 hours of drying at 400°C to precipitate the desired $(Na_{0.5}Li_{0.5})_xB_{1-x}O_{1.5-x}$, x=0.75.

To produce the desired carbonate salts, potassium carbonate (K_2CO_3) and lithium carbonate (Li_2CO_3) were purchased from Sigma Aldrich. Powders in the eutectic 1.63 Li_2CO_3/K_2CO_3 molar ratio were blended with a small quantity of water, mixed thoroughly using a mortar and pestle, and the resulting slurry was dried at 350°C for 16 hours. The dried solidified salt was then ground and blended again.

Mixtures of borates and carbonates were produced by thoroughly blending the constituent powders, synthesized as above.

Nickel crucibles were purchased from VWR, and an opening was punctured and used to coil a copper wire lead. Cathode materials consisted of either 0.5 mm diameter straight platinum wire (Sigma Aldrich), or 1 cm diameter coils of galvanized steel (Fi-Shock WC-14200, G90 coating designation according to ASTM A653; zinc coating layer thickness approximately 18 μm)., 316 stainless steel (Mcmaster-Carr), or nickel (Goodfellow).

2) Experimental Procedure

Unless specified otherwise, all electrolysis experiments detailed in this chapter consist of the following steps:

1) The salt powder is loaded into a nickel crucible and placed in the furnace. After purging N_2 for 30 minutes, the furnace is then heated to 600°C in 75 minutes and held isothermally for 60 minutes to melt the salt and release residual water.
2) After cooling, freezing, and disassembly, a hole is drilled in the solidified salt and used to insert the cathode, which is then locked into place by a mica lid with holes for gas exchange. This ensures full submersion regardless of variations in packing density or water content of the initial powder.
3) After assembly, the electrolysis cell is loaded into the tube, and N_2 is purged for 30 minutes at room temperature. The furnace is then heated to 550°C in 75 minutes and held isothermally for 60 minutes to ensure full melting before cyclic voltammetry measurements are taken.
4) The gas flow is switched to 50 cc/min of 99% CO_2 and held isothermally for 3 hours before additional cyclic voltammetry measurements are taken. A constant current of -240 mA is then applied for 1 hour, and the cathode is manually lifted out of the salt prior to cooling and freezing.
5) The carbonaceous product and residual salt are removed from the cathode by sonication in deionized water (0.5 h). The product is then purified from the residual salt by dialysis of the suspension against 1% nitric acid (membrane cut-off weight, 12-14 kDa) followed by the particle removal, washing in deionized water, and lyophilization.

3.2 Characterization of Borate Electrolytes with Platinum Electrodes

3.2.1 Sodium/Lithium Borate Electrolyte Characterization

To characterize the electrochemical properties of the alkali borate salts, a series of experiments were performed using two platinum wires, which have been shown to be chemically inert with respect to alkali borates, in a nickel crucible. Prior to the experiment, 3 batches of salt were

successively pre-melted into a nickel crucible under a nitrogen environment at 600°C. The melt took on a slight greenish tint compared to its usual white, darkening with each successive melt and indicating dissolution of the nickel crucible. While no definitive conclusions can be drawn about the oxidation state, this resembles the green coloration of nickel ii oxide, compared to black nickel iii oxide formed on the crucible by steam leaving the salt.

Figure 3-2: Pre-melted and solidified Sodium/Lithium Borate in a nickel crucible prior to experimentation. The green coloration suggests dissolution of nickel oxide into the melt.

After pre-melting and freezing, the smooth 0.5 mm diameter wires were inserted 14 mm into the melt, for an active surface area of 0.22 cm. Cyclic voltammetry results examining $Na_{1.5}Li_{1.5}BO_3$ are given below.

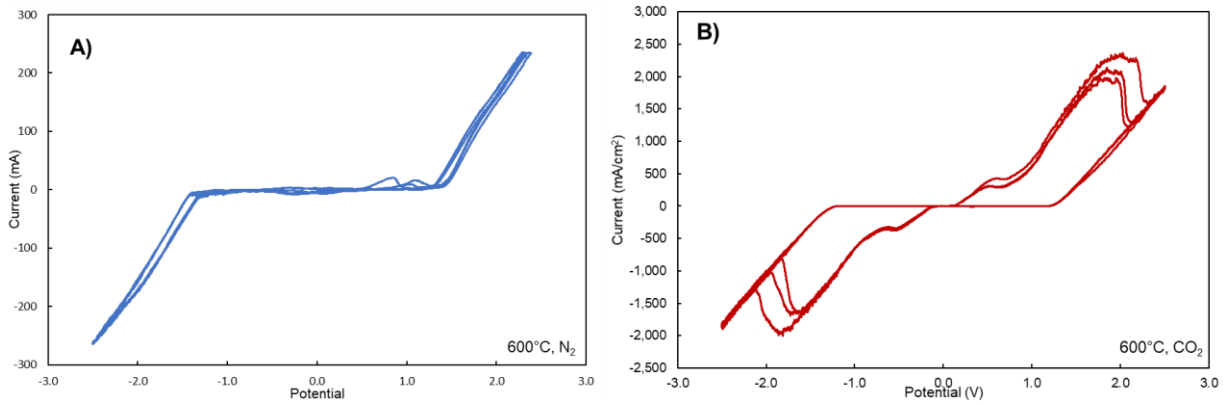

Figure 3-3: Cyclic Voltammetry of $(Na_{0.5}Li_{0.5})_xB_{1-x}O_{1.5-x}$ for x=0.75 at 600°C at 20mV/s between two platinum electrodes a) after 2 hours in N_2 and b) after 6 hours in CO_2

Prior to CO_2 uptake (a), the only reaction observed in the molten $Na_{0.5}Li_{0.5}BO_3$ is a plating reaction initialized between a 1.3 and 1.4V pair potential. Based on trends observed in carbonate salts,[19] and other studies examining electrolysis of boron oxides,[67] this most likely represents electrodeposition of lithium and/or sodium. Sodium is more susceptible to electroreduction, and is the more likely candidate unless co-deposition of both metals occurs.

After CO_2 is absorbed (b), an additional set of symmetric, irreversible peaks is clearly observed, potentially representing electroreduction of carbonates. It is important to note that time elapsed is a confounding variable – nickel is known to be corroded and dissolved by alkali borates over time, so these new peaks could also represent nickel ions present in greater quantities in the salt after

equilibrating for several hours. A 60-minute chronopotentiometry was then conducted, as shown below.

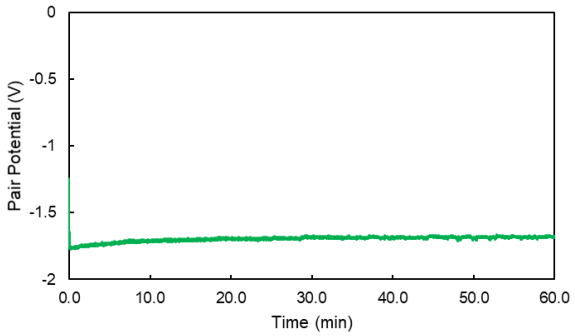

Figure 3-4: Chronopotentiometry of $(Na_{0.5}Li_{0.5})_xB_{1-x}O_{1.5-x}$ for x=0.75 at 600°C after 7 hours in CO_2 at a constant current of -150 mA (-650 mA/cm2)

The resulting voltage (-1.75V) is outside of the window of alkali borate stability, indicating that if carbon is successfully reduced, co-deposition of Na/Li/B will likely also have occurred. The applied potential magnitude does not increase with time, suggesting that depletion of carbonates did not impact performance. An additional cyclic voltammetry measurement was repeated after electrodeposition to probe the electrochemical changes resulting from the process.

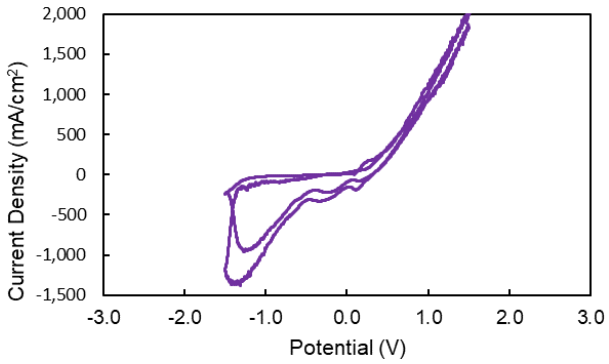

Figure 3-5: Cyclic Voltammetry of $(Na_{0.5}Li_{0.5})_xB_{1-x}O_{1.5-x}$ for x=0.75 at 600°C at 20mV/s between two platinum electrodes after 1 hour of constant current electrolysis at -150 mA (-680 mA/cm2*)*

The cyclic voltammetry profile observed differs significantly from that observed prior to electrodeposition in Figure 3-3 b. It is difficult to ascertain the absolute changes in pair potential due to a lack of viable reference electrodes in these operating conditions. The anode from the experiment shows the same sharp slope of alkali metal reduction in a positive current regime, but the additional peaks introduced during CO_2 absorption dominate at the cathode. The voltage range employed in this sweep was truncated due to current limitations of the potentiostat, which could contribute partially to the change in observed behavior at the cathode.

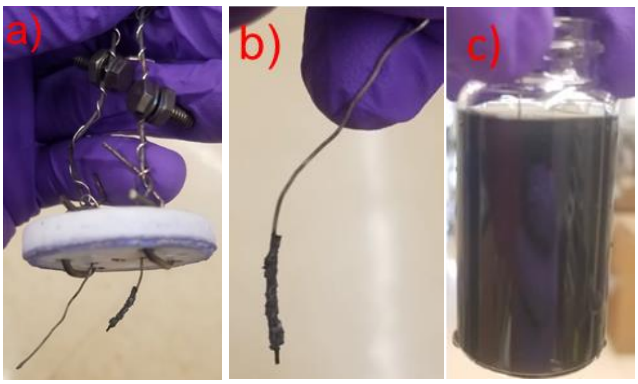

Figure 3-6: a) Platinum electrodes after experimentation b) Product observed on the platinum cathode, c) blackened product readily dispersed into deionized water, suggesting the presence of carbon

Upon disassembly, a significant buildup of blackened material was observed on the platinum cathode, which was readily dispersed into deionized water via sonication. Some amount of product was lost during extraction, evidenced by the exposed wire at the bottom of Figure 3-6b. By a geometric argument based on the length of wire exposed compared to the total length coated, this represents a product loss of roughly 15%, so the measured yield will be an underestimate. Of the 26 mg of product recovered, 10% (2.6 mg) was determined to be organic carbon after elemental analysis. The coulombic efficiency is given by the following equations:

$$C_e(\%) = \frac{M_{C,actual}}{M_{C,Theoretical}} \quad \text{Eq. 3-2}$$

$$M_{C,Theoretical} = \frac{QM_{C,g/mol}}{nF} \quad \text{Eq. 3-3}$$

Q represents the charge transferred, $M_{C,g/mol}$ is the molar mass of carbon, n is the number of electrons transferred per atom of carbon (4) and F is Faraday's constant (96485 C/mol). Accounting only for the 1-hour electrodeposition, we obtain a theoretical mass of 16.8 mg, for a Coulombic efficiency of 15.4%. If all negative currents incurred during cyclic voltammetry after CO_2 absorption are integrated and included in this calculation, the theoretical mass of carbon increases to 29.1 mg, and the corresponding coulombic efficiency decreases to 8.9%.

While the observed coulombic efficiency is low, the electrodes used were small, and therefore the applied current density of 680 mA/cm^2 was quite high (typical current densities applied in carbonate electroreduction experiments are on the order of 50-100mA/cm^2). From the CV profiles obtained, there could be a potential range where carbonate is reduced without significant co-deposition of alkali metals.

3.2.2 Lithium Borate Electrolyte Characterization

The body of literature suggests that sodium is electro-reduced at a lower potential than lithium, suggesting that lithium borate could offer a wider electrochemical stability window for reduction of carbonates. Therefore, the platinum electrode study was repeated using lithium borate ($Li_xB_{1-x}O_{1.5-x}$, x=0.75) at 800°C. Three batches of lithium borate were again successively pre-melted into a nickel crucible at 800°C under nitrogen, and holes were drilled for insertion of the platinum

electrodes. In Figure 3-7, it is observed that the salt took on a blue color compared to its normal white, darkening with each successive melt as more nickel was oxidized and dissolved.

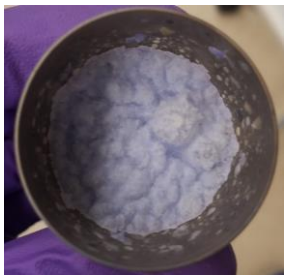

Figure 3-7: Pre-melted and solidified lithium borate in a nickel crucible prior to experimentation. The blue coloration suggests dissolution of nickel oxide into the melt.

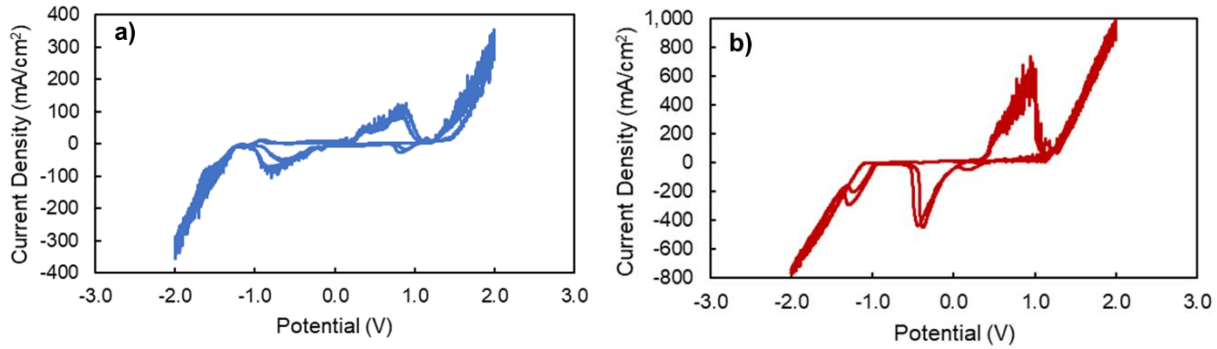

Figure 3-8: Cyclic voltammetry of $Li_xB_{1-x}O_{1.5-x}$ for x=0.75 at 800°C at 20mV/s between platinum electrodes a) after 2 hours in N2 and b) after 6 hours in CO2

In the cyclic voltammetry measurement performed under nitrogen (Figure 3-8a), two new symmetric, irreversible peaks are observed compared to the eutectic salt CV profile in Figure 3-3a. Because this experiment is conducted at 800°C and lithium borate is known to be more corrosive than sodium borate or the eutectic sodium/lithium blend, it is likely that this represents a reaction with the nickel dissolved into the salt medium, potentially the reduction of nickel iii oxide to nickel ii oxide. The onset of lithium plating occurs at a smaller pair potential difference of +/- 1.1-1.2V, indicating that the increase in temperature further reduces the electrolyte stability window.

Cyclic voltammetry measurements taken after 3 hours in CO_2 indicate no new peaks; the magnitudes of the nickel and alkali metal peaks already present are modified due to transient effects. Noticeably absent are the peaks near 1.75V observed in $Na_{1.5}Li_{1.5}BO_3$, which likely represented the reduction of carbonates. Lithium borate (Li_3BO_3) has been proven effective at adsorbing CO_2 in the solid phase up to 650C,[68] but has not been studied as a standalone liquid sorbent due to its excessively high working temperature - the lack of carbonate reduction peaks suggests that no CO_2 was absorbed.

A chronopotentiometry trial was attempted, but after 50 minutes of steady operation at -1.7V, the voltage rapidly dropped to -13V and exceeded the potentiostat working limits. At the experiment conclusion, the electrodes could not be fully extracted from the salt before cooling, and therefore

the product was frozen in place and could not be characterized. Because no evidence of CO_3^{2-} reduction was observed, the experiment was not repeated.

3.3 Electroreduction of CO_2 in Borate/Carbonate Blends

3.3.1 Thermodynamic Properties of Borate-Carbonate Blends

While $Na_{1.5}Li_{1.5}BO_3$ and $(Li_{0.62}K_{0.38})_2CO_3$ are well studied individually, the resulting intermediate mixtures have not been characterized in the literature. The working capacity of borate salts was shown to be heavily dependent on the lithium content, with sodium primarily serving to lower the working temperature as a eutectic mixture.[28] Therefore, we hypothesize that a eutectic mixture approaching $(Na_{0.25}K_{0.25}Li_{0.5})_2$ would match this capacity and potentially achieve lower working temperatures. To determine the melting points and CO_2 capacities of these blends, we conducted measurements using differential scanning calorimetry (DSC) and thermogravimetric analysis (TGA).

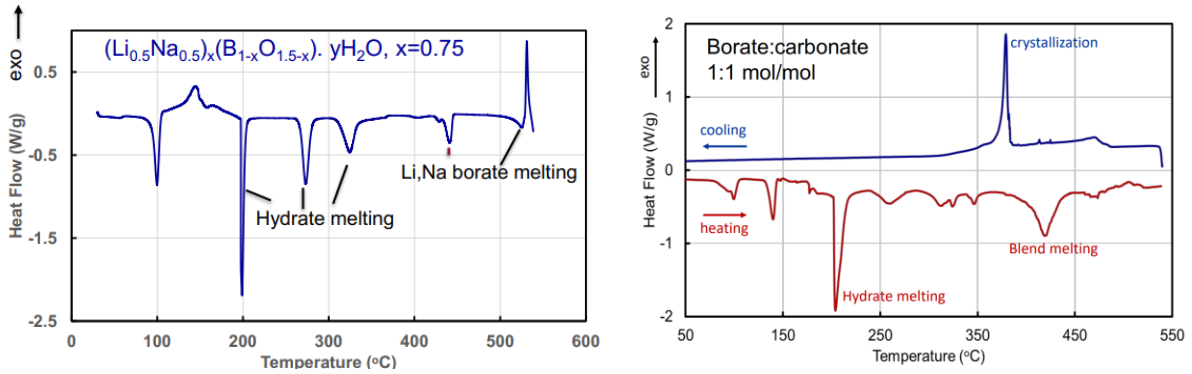

Figure 3-9: DSC Characterization of a) $Na_{1.5}Li_{1.5}BO_3$ and b) 1:1 $Na_{1.5}Li_{1.5}BO_3$: $(Li_{0.62}K_{0.38})_2CO_3$ blends under N_2 at a heating rate of 5°C/min

In Figure 3-9a, we observe a series of peaks representing the release of hydrates from 100C-350C, becoming fully molten at 530C. These results are consistent with previous findings.[28] Figure 3-9b characterizes a 1:1 molar blend of these salts. We again observe a series of small hydrate peaks, ultimately followed by peaks representing melting of the blend components. After the initial melting, we observe a single reversible peak at 380C, representing the melting point of the eutectic mixture.

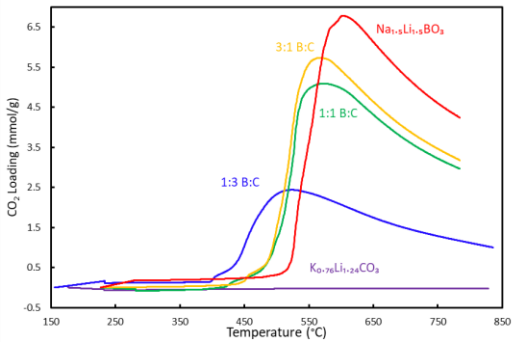

Figure 3-10: CO_2 uptake profiles of $Na_{1.5}Li_{1.5}BO_3$ / $(Li_{0.62}K_{0.38})_2CO_3$ blends under 60 mL/min of 99% CO_2 at a heating rate 5°C/min. All ratios are on a C to B molar basis

From the TGA profiles presented in Figure 3-10, we observe that the working capacities of each salt follow roughly the proportion of borate/carbonate present, scaling from 0 mmol/g capacity with 100% carbonate to 6.5 mmol/g at 100% borate. We observe that the working capacities are lower than those observed by Halliday et. al.,[28] which showed uptake in excess of 8 mmol CO_2/g under 20% CO_2. This discrepancy is primarily because pretreatment under nitrogen in this study was only carried out to 600°C rather than 850°C to avoid calcining the carbonates. It is also noted that the onset temperature of CO_2 uptake is lowered to 400°C for the blended salts, compared to 500°C for pure borate, indicating that the eutectic effect lowering the melting point also corresponds to earlier CO_2 uptake.

3.3.2 Electrochemical Characterization and Electrolysis of Borate/Carbonate Blends

To determine the electrochemical properties of the borate/carbonate blends, a series of electrolysis experiments were performed according to the procedure described in section 3.1.2 using a galvanized steel cathode and a nickel crucible anode at 550°C. Cyclic voltammetry profiles are presented below for a 1:1 borate to carbonate starting mixture.

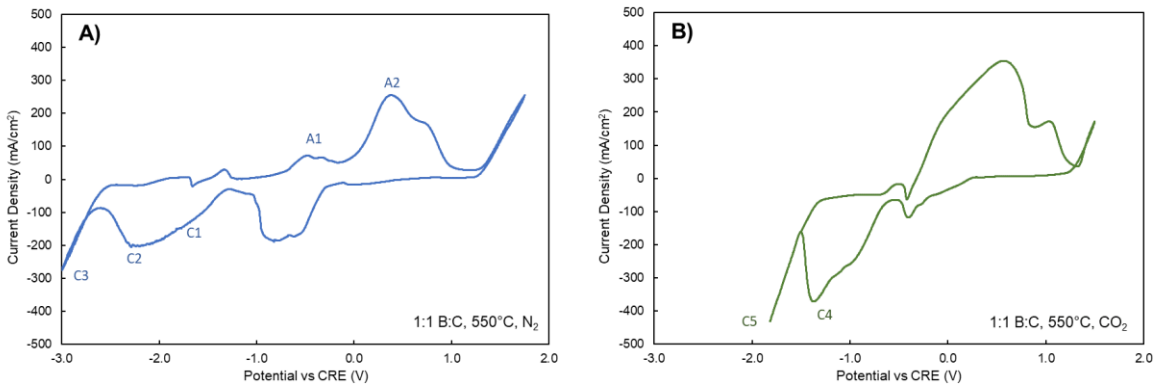

Figure 3-11: Representative cyclic voltammograms (CV) of a galvanized steel cathode in molten borate and carbonate blend (nominal borate: carbonate mol ratio, 1:1,. Borate: $(Li_{0.5}Na_{0.5})_xB_{1-x}O_{1.5-x}$; x=0.75; carbonate: $Li_{0.62}K_{0.38}CO_3$. Anode: nickel crucible; temperature: 550°C. The potential scan started cathodically from 0 V, and the reduction and oxidation sweep directions are shown by arrows (IUPAC convention). Solid and dotted lines show three consecutive scans (scanrate, 10 mV/s) measured under nitrogen and CO_2 purge, respectively. Designations A and C stand for anodic and cathodic peak potentials, respectively. CVs are conducted A) after 1 hour at 600°C in N_2 and B) after 3 hours purging CO_2 at 600°C

In Figure 3-11, CRE stands for Carbonate Reference Electrode (potential vs reference CO_2 oxidation reaction is E^o=0 V (900°C). In our control experiment conducted under air purge, a systemic -0.131 V shift was observed due to the electrochemical cell parameters and conditions relative to the standard potential (E^o=0 V, 900°C) characteristic of the carbonate ion oxidation in molten carbonates. [69]

$$CO_3^{2-} \rightarrow CO_2 + 0.5O_2 + 2e^- \qquad \text{Eq. 3-4}$$

Reaction 3-4 is indicated by A1 in Figure 3-11. The observed formation of black coating on the anode interior (compare with Fig. 6) is attributed to the nickel oxidation reaction on the anode-melt interface with the reported standard potential E^o = 0.697 V (900°C)[69,70]

$$Ni^o + CO_3^{2-} \rightarrow NiO + CO_2 + 2e^- \qquad \text{Eq. 3-5}$$

Reaction 3-5 is indicated by A2 on the oxidation scan in nitrogen atmosphere in Figure 3-11 A. Lower oxidation currents are observed on the initial scan. Numerous prior studies reported a variety of reduction reactions for nickel compounds in the presence of neutral gas or carbon dioxide:[71–74]

$$NiO + 2e^- \rightarrow Ni^o + O_2^- ; E^o = -1.50\ V \qquad \text{Eq. 3-6}$$

Important deposition potentials of alkali and alkaline earth metals via reactions (13) and carbon through reactions (14) in their own molten carbonate salts are well-known and are given below in Table 2.[19,75]

$$\text{Electrochemical deposition of metal: } 2M_2CO_3 \rightarrow 4M + 2CO_2 + O_2 \text{ (M = Li, Na or K)} \qquad \text{Eq. 3-7}$$

$$\text{Deposition of carbon via salt decomposition: } 3M_2CO_3 \rightarrow C + 3M_2O + O_2 \qquad \text{Eq. 3-8}$$

Molten salt	Alkali metal deposition, potential (V)	Carbon deposition, potential (V)
Li_2CO_3	-2.964	-1.719
Na_2CO_3	-2.546	-2.551
K_2CO_3	-2.612	-3.083

Table 3-1: Deposition potentials (vs. $CO_3^{2-}/CO_2–O_2$) of alkali and alkaline earth metals via reaction (3-7), and carbon via reaction (3-8) in their respective molten carbonate salts at 600 ºC. Deposition potentials are taken from prior art75

In our experiments with borate/carbonate blends in nitrogen atmosphere (Figure 3-11 A), carbon was produced by cathodic reduction of the carbonate anions (reaction 3-8) formed by dissociation of the molten alkali metal carbonates (indicated as C2 in the -2.3 V range). Carbon was deposited on galvanized steel cathode in significant quantities, along with deposition of alkali metals and boron. The processes of deposition are indicated by C3 in Figure 3-11 A.

In the presence of the Li,Na borate in the borate/carbonate blend, borate anions (BO_3^{3-}) anions formed by dissociation of the borate in the molten salt greatly contribute to the CO_2 capture and its enhanced chemisorption.

$$BO_3^{3-} + CO_2 \leftrightarrow CO_3^{2-} + BO_2^- \qquad \text{Eq. 3-9}$$

Borate anions also contribute to the metaborate and oxygen anion generation by the molten salt:[61]

$$BO_3^{3-} \leftrightarrow BO_2^- + O^{2-} \qquad \text{Eq. 3-10}$$

Hence, in the presence of borate, the formation of carbonate anions needed for CO_2 electroreduction is augmented, which, in turn, leads to the carbon deposition on cathode at lower cathodic potentials:

$$CO_3^{2-} + 4e^- + 3BO_2^- \rightarrow C + 2BO_3^{3-} \qquad \text{Eq. 3-11}$$

Potentials corresponding to the carbonate electroreduction under CO_2 atmosphere in the -1.4 to -1.2 V range and carbon/metal deposition in the -1.8 to -1.5 V range are indicated by C4 and C5, respectively, in Figure 3-11 B. Electroreduction processes in Eq. 3-11 (C4) can be seen as

transient, as their peak potentials were lowered with the number of scans, indicating that the majority of dissolved CO_2 was electroreduced.

After each experiment, the cathode was retracted and the product was recovered according to the procedure in 3.1.2. We again define the coulombic efficiency using the following equations:

$$C_e(\%) = \frac{M_{C,actual}}{M_{C,Theoretical}} \quad \text{Eq. 3-12}$$

$$M_{C,Theoretical} = \frac{QM_{C,g/mol}}{nF} \quad \text{Eq. 3-13}$$

Q represents the charge transferred, $M_{C,g/mol}$ is the molar mass of carbon, n is the number of electrons transferred per atom of carbon (4) and F is Faraday's constant (96485 C/mol). Here, Q is integrated overall negative currents applied in cyclic voltammetry and chronopotentiometry. These values are used to construct the following figure relating the starting borate/carbonate molar ratio to coulombic efficiency.

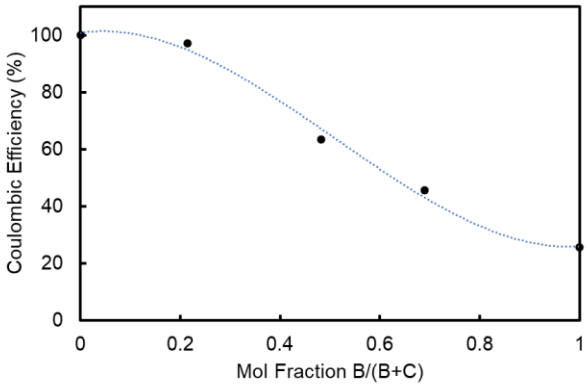

Figure 3-12: Coulombic Efficiency of CO_2 reduction in $Na_{1.5}Li_{1.5}BO_3$ /$(Li_{0.62}K_{0.38})_2CO_3$ blend

The coulombic efficiency of the electrolysis process decreases as the relative concentration of carbonate decreases with respect to borate. Comparing the coulombic efficiency to CO_2 uptake capacity, we observe two competing trends:

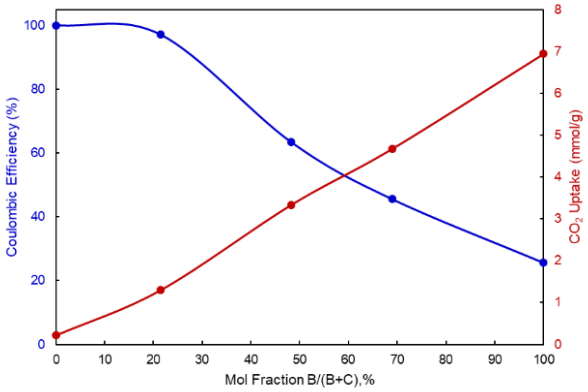

Figure 3-13: Coulombic Efficiency of carbon electrodeposition in $Na_{1.5}Li_{1.5}BO_3$ / $(Li_{0.62}K_{0.38})_2CO_3$ blend compared to the CO_2 capacity

As borate concentration increases, so does the capacity for CO_2. At the same time, the reduction in CO_3^{2-} concentration results in lowered coulombic efficiency from co-deposition of K/Na and B. This visualization suggests that a 1:3 borate to carbonate ratio optimizes the effectiveness of the sorbent, dramatically increasing the CO_2 solubility of the molten salt without sacrificing significant coulombic efficiency to the relatively small electrochemical stability window of alkali borates compared to alkali carbonates.

3.3.3 Characterization of CNT Products

While elemental analysis indicates the organic carbon content of the recovered product, the product morphologies are equally important for this study. To determine if carbon nanotubes were obtained, the recovered products were analyzed via x-ray diffraction and transmission electron microscopy. We first present profiles obtained by x-ray diffraction of the obtained products:

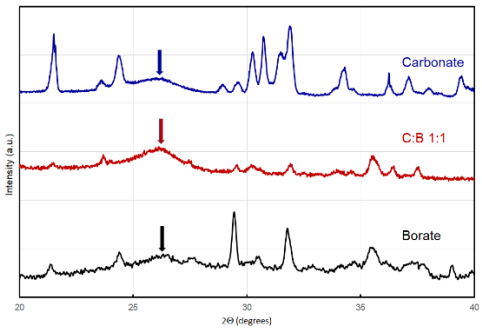

Figure 3-14: X-ray diffraction analysis of the carbon produced by CO_2 uptake and electrolysis of pure carbonate ($(Li_{0.62}K_{0.38})_2CO_3$), a 1:1 borate carbonate mixture on a C:B molar basis, and pure borate ($Na_{1.5}Li_{1.5}BO_3$)

The peaks shown in the x-ray diffraction profiles presented are characteristic of lithium, sodium, carbonate, and oxides of nickel and zinc. Importantly, the broader peaks denoted by an arrow are characteristic of graphitic carbon. While graphitic peaks are promising, several possible carbon morphologies could produce them. Therefore, transmission electron microscopy was also used to observe the carbonaceous products in detail. Images are presented in Figure 3-15.

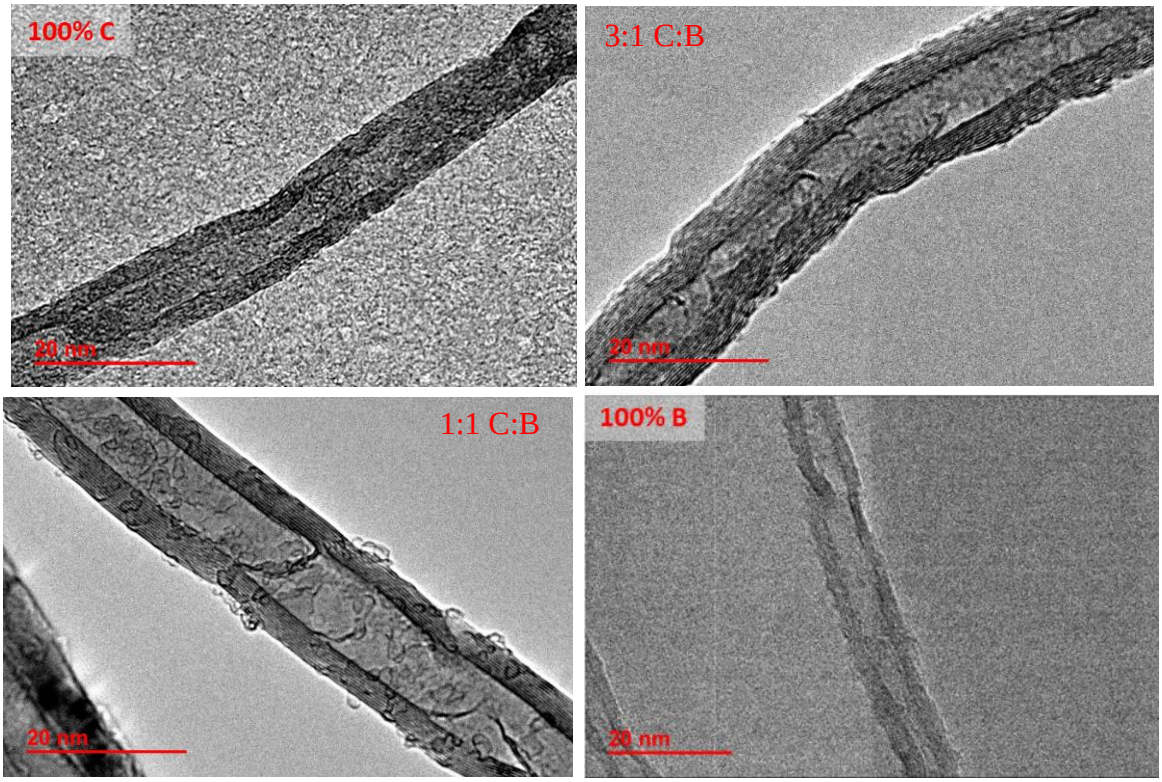

Figure 3-15: TEM images of carbonaceous products obtained using blends of $Na_{1.5}Li_{1.5}BO_3$ / $(Li_{0.62}K_{0.38})_2CO_3$ both individually and in 3:1 and 1:1 ratios.

The images in Figure 3-15 show carbon nanotubes approximately 15 nm in diameter with walls 5 nm thick. The nanotubes obtained with each electrolyte do not differ appreciably, but rough structures observed in detail in the 1:1 image suggest co-deposition of boron nanoparticles as observed by Wang et. al. when adding calcium metaborate ($CaBO_2$) to lithium carbonate (Li_2CO_3) for electrolysis.[48] While this image indicates the presence of carbon nanotubes, it does not inform the relative quantities of different species. Scanning electron microscopy images (SEM) are provided below for further insight, clearly showing carbon nanotubes in high quantities.

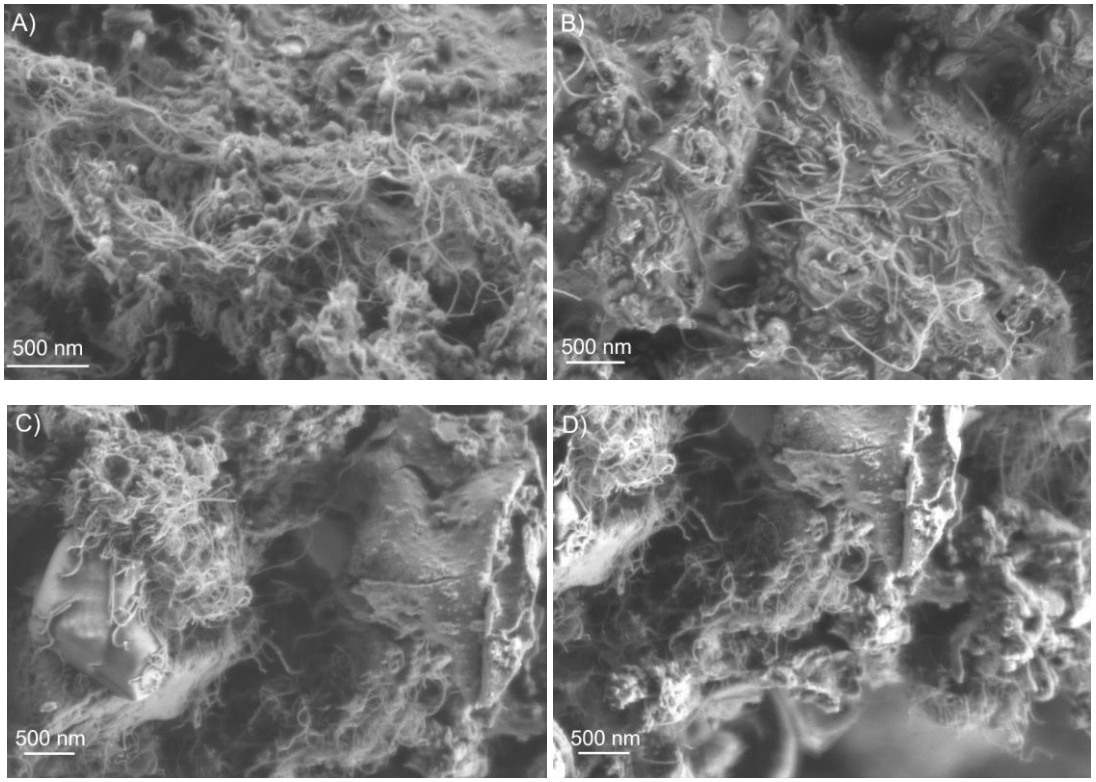

Figure 3-16: SEM images of carbon nanotubes obtained by electrolyzing a 1:1 C:B starting molar mixture (A and B), and pure borate starting mixture (C and D)

3.4 Alkali Borate Electrolysis with Alternate Cathode Materials

The study above was conducted using a galvanized steel cathode, which is known to be oxidized and dissolved by the alkali borate salts[33]. The mass of the galvanized steel is small with respect to the overall mass of the salt, so the impact of this dissolution is limited - salt drilled out from the crucible retained its CO_2 capacity from before the experiment, indicating that this effect is relatively small. However, in a real system utilizing alkali borates, these material compatibility concerns would be significant. Therefore, it is desirable to determine if other electrode material can be used for deposition of carbon nanotubes in alkali borates even without the catalyzing effects of zinc oxide or iron. The work of Halliday et. al. indicates that nickel is the most stable non-precious containment material with respect to alkali borates[33], and was therefore chosen as a candidate material. 316 Stainless steel was found to be corroded much less rapidly by borates than galvanized steel in the same study, and has been shown to be an effective cathode for formation of CNTs in carbonates in other studies.[50]

3.4.1 Electrolysis Between Nickel and Stainless Steel

Following the experimental procedure outlined in 3.1.2, a series of cyclic voltammetry measurements and an electrodeposition were conducted between a nickel crucible anode (Sigma Aldrich) and a coiled 14-gauge wire 316 stainless steel (316SS) cathode (McMaster-Carr). A comparison of cyclic voltammetry profiles is presented below.

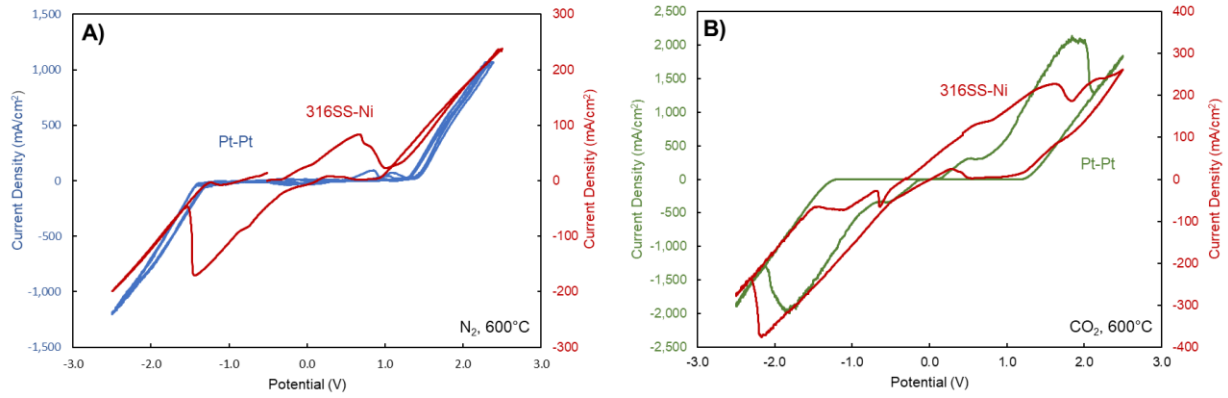

Figure 3-17: Cyclic voltammetry profile of $(Na_{0.5}Li_{0.5})_xB_{1-x}O_{1.5-x}$ for x=0.75 at 20 mV/s comparing a pair of platinum electrodes to a 316SS coil/nickel crucible pair after a) 1 hour at 600°C in N_2 and b) after 3 hours purging CO_2 at 600°C

In Figure 3-17a under N_2, two additional peaks are present in addition to the standard electrodeposition of sodium, representing the oxidation and reduction of nickel. After purging CO_2 for several hours, the characteristic CO_3^{2-} peak is observed near -2.0 V. Not shown are 2 earlier CV cycles taken in N_2 showing this same 2.0V peak with a gradually diminishing magnitude, suggesting that some CO_2 is initially present in the salt prior to CO_2 purging

The chronopotentiometry conducted at -120 mA/cm^2 was carried out at a steady -1.79V, showing no signs of fluctuation due to ion depletion. Coulombic efficiencies and electron micrographs were not available at the time of submission, but ready dispersion of the obtained product suggests CNT formation.

3.4.2 Electrolysis Between Nickel Electrodes

Following the experimental procedure outlined in 3.1.2, a series of cyclic voltammetry measurements and an electrodeposition were conducted between a nickel crucible (Alfa Aesar) and a coiled wire nickel cathode (Goodfellow). A comparison of cyclic voltammetry profiles is presented below.

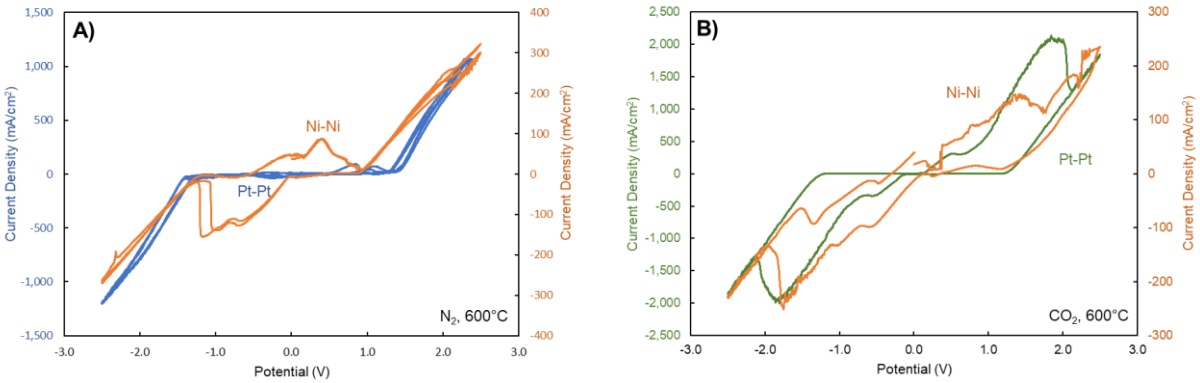

Figure 3-18: Cyclic voltammetry profile of $(Na_{0.5}Li_{0.5})_xB_{1-x}O_{1.5-x}$ for x=0.75 at 20mV/s comparing a pair of platinum electrodes to a nickel coil/crucible pair after a) 1 hour at 600°C in N_2 and b) after 3 hours purging CO_2 at 600°C

In Figure 3-18a under N_2, two additional peaks are present in addition to the standard electrodeposition of sodium, representing oxidation and reduction of nickel and nickel oxides.

After purging CO_2 for several hours, the characteristic CO_3^{2-} peak is observed near -2.0 V. Not shown are 2 earlier CV cycles taken in N_2 showing this same 2.0V peak with a gradually diminishing magnitude, suggesting that some limited CO_2 is initially present in the salt prior to CO_2 purging.

The chronopotentiometry conducted at -120 mA/cm^2 was carried out at a steady -2.3V, requiring nearly 0.5V more than 316SS cathode, but showing no signs of fluctuation due to ion depletion. It is unclear what contributions to this additional potential are due to potential variation in the submersion depth of the two cathodes, ohmic losses, or the cathode chemistry. Coulombic efficiencies and electron micrographs were not available at the time of submission, but ready dispersion of the obtained product suggests CNT formation.

4 Electrochemically Mediated Alkaline Thermal Treatment Process – Feasibility Studies

4.1 Introduction – The Alkaline Thermal Treatment Process

A recent paper by the Park group at Columbia University details an Alkaline thermal treatment process (ATT), whereby hydrocarbons in organic material (here, seaweed) are gasified through a reaction with alkali hydroxide salts to produce hydrogen.[64] This is exemplified through the following nominal cellulose exothermic reaction (ΔH=-629.2 kJ/mol), taking place at 500°C:

$$C_6H_{10}O_5 + 12NaOH + H_2O \rightarrow 6Na_2CO_3 + 12H_2 \qquad \text{Eq.4-1}$$

While further study is necessary to understand the exact mechanisms at play, the key to this process is hypothesized to be the alkalinity of the molten salt. It is analogous to paper pulping, where concentrated NaOH is used to break down cell walls, cell fibers, and glycoproteins to access the underlying sugars and hydrocarbons. This paper represents a significant advancement, both for its high relative conversion efficiencies compared to other biomass gasification processes, and because the process has synergy with seaweed, which is abundant but typically undesirable for biomass applications due to its high water and salt content. Preliminary results suggest that this process can be used for gasification of common plastic wastes such as LDPE – if this generalizes, alkaline thermal treatment could offer a promising avenue for treatment of biomass-contaminated ocean surface plastics, which cannot currently be recycled or gasified cost-effectively through traditional means. The Alkaline Thermal Treatment Process[65] outlined by Zhang et. al. is presented in Figure 4-1, with key process operations detailed below.

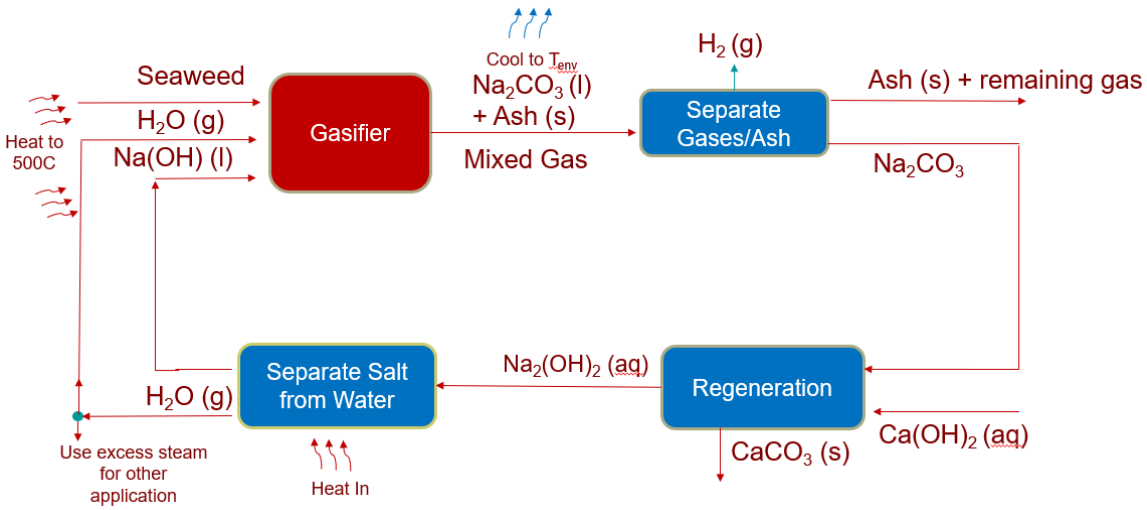

Figure 4-1: Base configuration of the Alkaline Thermal Treatment Process for hydrogen production from oceanic biomass, as described in[64]

Alkaline Gasification + Water-Gas Shift

Molten NaOH salt is contacted with seaweed and steam to produce hydrogen, carbonate salt, ash, and carbon monoxide. Downstream, the syngas produced in the gasifier is reacted with steam over a Ni/ZrO_2 zeolite catalyst to produce H_2 and CO_2 by the water-gas shift reaction:76

$$CO + H_2O \rightarrow H_2 + CO_2 \qquad \text{Eq. 4-2}$$

The conversion efficiency of this reaction is heavily temperature dependent, becoming more thermodynamically favored at low temperatures, but with increasingly sluggish kinetics as the

temperature decreases. In industrial steam methane reforming processes, this reaction is typically performed in two stages, with most (~95%) of the CO being converted at high temperature and the remaining gas being converted at low temperatures. Because the carbon capture is assumed to occur at 500 °C, this reaction will contain inherent thermodynamic inefficiencies associated with side reactions and waste process heat that necessitate thermodynamic study. The overall gasification reaction consisting of molten salt gasification and water gas shift steps is described in aggregate via Eq. 4-1.

Gas Treatment + CO_2 Capture

After reacting the syngas to near completion, the CO_2 in the gas is captured, the remaining steam is condensed and removed as liquid, and Hydrogen is separated for export. In the original paper, it is proposed that the CO_2 capture be performed using calcium looping, according to the following set of reactions:

$$Ca(OH)_2 + CO_2 \rightarrow CaCO_3 + H_2O \quad \text{Eq. 4-3}$$

$$CaCO_3 \rightarrow CaO + CO_2 \quad \text{Eq. 4-4}$$

$$CaO + H_2O \rightarrow Ca(OH)_2 \quad \text{Eq. 4-5}$$

While technologically feasible, implementation of this process is challenging due to sluggish CO_2 capture kinetics that require aqueous chemical treatment or calcining at elevated temperatures in excess that of the second stage of most industrial water-gas shift reactors (most real processes perform this reaction at 900°C, which would require a separate oxy-combustion unit). In practice, this would more likely be performed via room temperature options like pressure swing adsorption.

Ash Separation

The $NaCO_3$/ash mixture is cooled to room temperature, crushed, dissolved, and filtered to remove ash solids. Dust generated during crushing is recovered electrostatically. Removing only water-insoluble species will result in a gradual buildup of trace elements over time, but the gasification process is tolerant to containments, and the salt medium and can be replaced periodically as needed due to the relatively low capital cost of Na_2CO_3.

NaOH Regeneration

Na_2CO_3 is cooled to room temperature, crushed, and dissolved in a $Ca(OH)_2$ solution for regeneration via the following metathesis reaction:

$$Ca(OH)_2(s) + Na_2CO_3(aq) \leftrightarrow 2NaOH(aq) + CaCO_3(s) \quad \text{Eq. 4-6}$$

This is an equilibrium reaction that loses effectiveness as the concentration of Na species increases77, following Le Chatelier's principle. This process is slightly endothermic, but the heat is readily provided by the initial CaO to $Ca(OH)_2$ reaction.

Salt Separation

To re-use in the gasifier, the NaOH must be separated from solution. In the closely analogous NaOH regeneration step of the Kraft process used in wood pulping78, this is accomplished by heating to 180 °C under slight vacuum.

Causticizing

When contacted with water, CaO readily reacts to form $Ca(OH)_2$ via Eq. 6. While this process is exothermic, the waste heat is low temperature and difficult to recover – it can generally be assumed to be consumed in the conjugate NaOH regeneration reaction.

The base process described above is not optimized and does not account for heat recuperation and other practical considerations; a more detailed technoeconomic analysis is presented in Chapter 5.

4.1.1 Alkaline Thermal Treatment: Regeneration Considerations

The high relative cost of NaOH and other alkali hydroxides compared to CaOH readily eliminates once-through processes with respect to alkali salts, so regeneration is necessary for economic operation. This regeneration can be accomplished through several means, primarily either through the metathesis reaction with $Ca(OH)_2$ described in Equation 4-6

4.1.1.1 $Ca(OH)_2$ Regeneration: Closed vs Open Loop sourcing

In the original concept paper, it is noted that $Ca(OH)_2$ can be sourced in fairly large quantities as industrial waste from industrial wastes such as steel slag, or from silicate minerals, constituting an open loop process with regards to $Ca(OH)_2$. These wastes are typically available at little or no cost beyond transportation and crushing, but it should be noted that the contained sulfur species can result in emissions of SO_x and H_2S upon hydration, requiring additional care.

It is also possible to close this loop by adopting a configuration in which a shared calciner is used to convert $CaCO_3$ back into CaO (and reacted with water to form $Ca(OH)_2$) for use both in carbon capture and NaOH regeneration. A closed loop process may in principle be advantageous due to lower feedstock prices and reduced waste treatment. However, in practice the closed loop process is economically and energetically prohibitive in unit operations associated with the $Ca(OH)_2$ regeneration cycle at small-to-medium scales if the associated carbon emissions are to be avoided. Therefore, an open process sourcing $CaO/Ca(OH)_2$ as a consumable may be more feasible. The relative capital and energetic impact of $Ca(OH)_2$ regeneration with respect to hydrogen production unit operations will inform our understanding of the tradeoffs between closed-loop $Ca(OH)_2$ regeneration and open-loop $Ca(OH)_2$ procurement as a consumable feedstock, and is explored in greater depth in Chapter 5.

4.1.1.2 Electrochemical Regeneration Process Alternatives

The most significant energetic cost of the ATT process is the sensible heat associated with cycling the salt between 500-600°C for gasification and room temperature for aqueous regeneration. While the steam produced when separating NaOH from water can be fed into the reactor or used for other processes, heat recovery will not be perfect, especially given that Na_2CO_3 emerges from the reactor as a solid. A potential isothermal alternative in the form of carbonate electrolysis is as follows:

Carbonate Reduction: $\left.\begin{matrix} M_2CO_3 + 4e^- \rightarrow M_2O + C + 2O^{2-} \\ 2O^{2-} \rightarrow O_2 + 4e^- \end{matrix}\right\} M_2CO_3 \rightarrow M_2O + C + O_2$ Eq. 4-7

Causticization: $M_2O(soln) + H_2O(g) \rightarrow 2MOH\ (l)$ Eq. 4-8

This pathway requires a significant amount of electrical energy input compared to thermochemical regeneration. By selecting a lithium-rich electrolyte, it can be possible to derive carbon nanotubes (CNTs) or other high value carbonaceous products, recuperating the cost. With multiwalled CNT valued at $100-200/kg and significant costs imposed by the high associated electricity consumption of electrolysis, the economics of this regeneration step overshadow the rest of the system. It would therefore be better framed as CNT production with low-cost hydrogen as an added benefit. If losses of the more expensive lithium-based working fluid can be minimized, this additional revenue stream could make less profitable ATT applications like conversion of ocean surface plastics more attractive, as the hydrogen and thermal energy released are not solely responsible for profitability.

A challenge arises in the temperature mismatch between established conditions for ATT and carbonate electrolysis. In the ATT configuration posed by Zhang et al.[64], the gasification process is limited to 500-600°C, as the nickel/zirconia catalysts employed in cracking gaseous hydrocarbons become less active above this temperature range. Target temperature ranges for electrolysis of Li_2CO_3 are typically above 750°C due to the increased solubility of oxide species in the melt. Li_2O solubility in Li_2CO_3 is reported on the order of 15% at 750°C, with some studies suggesting a solubility as high as 42% by mole at 750°C. [60] This is significantly higher than the solubility of 0.5% by mole measured up to 700°C in eutectic $Li_{0.87}Na_{0.62}K_{0.5}CO_3$.[60] This increased solubility dramatically improves the working capacity of the electrolyte and improves kinetics, as the oxygen evolution reaction is kinetically limiting.[50] Nonisothermal operation is a possibility, but poses thermodynamic penalties due to imperfect heat exchange in streams between the two reactors and the higher temperature for required heat input.

The causticization reactions described above offer a potential means to remedy this temperature mismatch. If steam were to be continuously purged into the cell during electrolysis, the Li_2O species would be converted to LiOH as they form. MOH species melt at a much lower temperature than M_2O or M_2CO_3 species, and therefore would not impose the same solidification challenges. The system working capacity would therefore be limited by the coulombic efficiency achievable by the electrolysis cell with an increasing MOH/M_2CO_3 ratio, as the carbonate reduction reaction must compete with the corresponding OH^- reduction reactions:

$$\left.\begin{matrix} 4LiOH + 4e^- \rightarrow 2Li_2O + 2H_2 + 2O^{2-} \\ 2O^{2-} \rightarrow 4e^- + O_2 \end{matrix}\right\} 4LiOH \rightarrow 2Li_2O + 2H_2 + O_2 \quad \text{Eq. 4-9}$$

In prior studies of eutectic carbonate/hydroxide blends, at low current densities (2-30mA/cm^2), evolution of CO, CH_4 and H_2 tends to dominate.79 As the applied potential and corresponding current density increases on the order of 100mA/cm^2, deposition of carbon begins to dominate. In this manner, a portion of the carbonate could be converted to hydroxide by electrolyzing at high current density while purging steam. Syngas will be co-evolved with a steep overpotential penalty, but conversion can proceed until diminishing returns are achieved due to a drop in carbon deposition coulombic efficiency.

The two potential pathways described above are summarized in Figure 4-2.

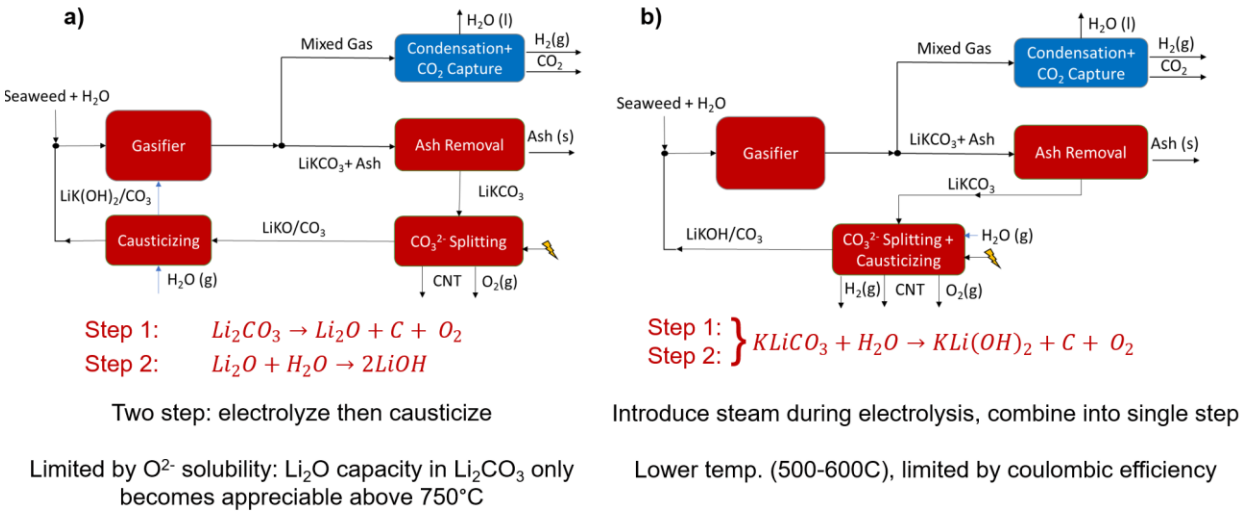

Figure 4-2: Process alternatives for electrochemically mediated alkaline thermal treatment process: a) two step regeneration at 750C, b) one step regeneration at 500-600C. Heat recovery is omitted for simplicity.

A third configuration closely analogous to the pathway in Figure 4-2b is a single continuous reactor, matching inputs of steam, biomass/plastics, and electrical current to achieve steady outputs of ash, carbon, and gaseous products. The primary benefit of this design is the potential to minimize space and capital expense, needing only one high temperature reactor vessel instead of two, which could enable economic operation at smaller scales. Several potential challenges are also posed by this approach. The rate of electrolysis is limited by the current density, limiting the achievable throughput compared to relatively rapid thermal gasification in a given working volume. Co-evolved oxygen from the electrolysis reactions is also likely to oxidize species and alter the overall chemistry. It is also unclear if the presence of hydrocarbons and ash in the salt impede the electrolysis reactions. This final point is addressed through experiments described in this work.

4.2 Electrochemical Synthesis of CNTs in Alkali CO_3^{2-}/OH^- Eutectic Salts

In the following experiments, we first aim to modify prior studies carried out examining carbonate/hydroxide blends to verify that we can obtain CNTs using our setup and determine the coulombic efficiencies of electrolysis in our chosen salts.79 We then aim to simulate gasification and electrolysis in a combined reactor to determine potential effects of LDPE and seaweed on CNT formation.

4.2.1 Molten Salt Selection and Characterization

Phase diagrams for common eutectic lithium salts used in material selection are presented below. Both $(Li_xNa_{1-x})_2CO_3$ and $Li_xK_{1-x}CO_3$ are fully molten in the target 500-600°C range in their eutectic ratios. It has been shown that the yield of carbon nanotubes increases with increasing lithium proportion80, so the eutectic $(Li_{0.62}K_{0.38})_2CO_3$ is selected over $NaLiCO_3$. It should be noted that sodium's lower costs, higher reductive potential, and higher presence in seaweed could also present compelling arguments for using $NaLiCO_3$, but the choice of complementary alkali metal is not expected to have a significant impact.

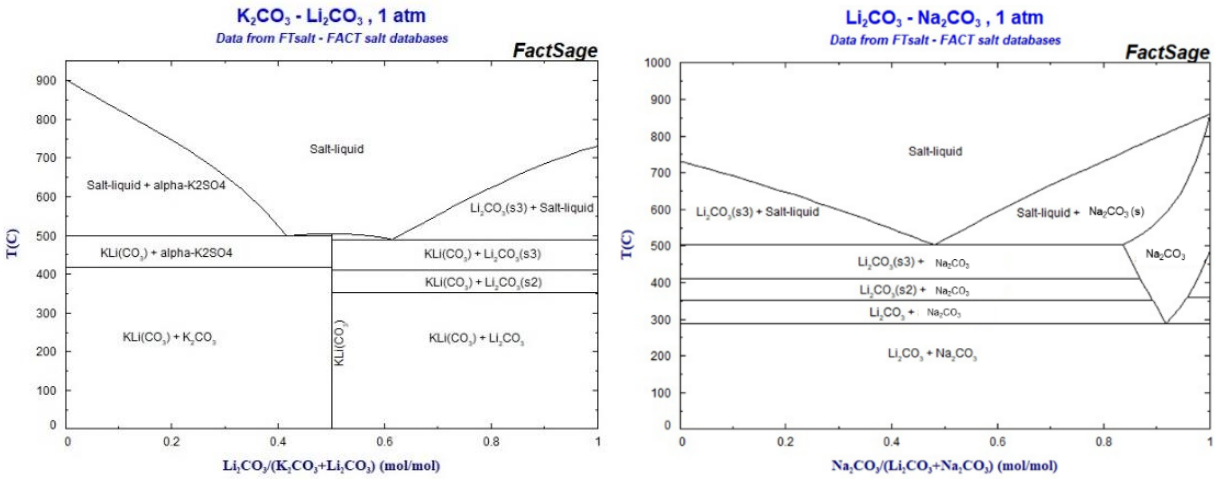

Figure 4-3*:* Phase Diagrams for K_2CO_3/Li_2CO_3 and Na_2CO_3/Li_2CO_3, taken from FactSage Database

By examining the phase diagram for various compositions of K^+/Li^+ and CO_3^{2-}/OH^-, we observe that the presence of hydroxide lowers the melting point of the salt, so we ensure that the system will be fully molten throughout operation.

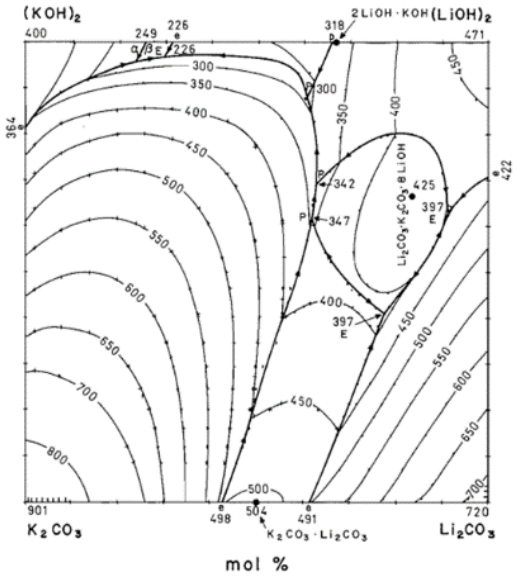

Figure 4-4: $KLiOH/KLiCO_3$ phase diagram,
Taken from Bale, C. W. & Pelton, A. D. Coupled phase diagram and thermodynamic analysis of the 18 binary systems formed among Li2Co3, K2Co3,Na2Co3, Lioh, Koh, Naoh, Li2So4, K2So4 and Na2So4. Calphad **6**, (1982).81

4.2.1.1 Salt Preparation

Potassium Carbonate (K_2CO_3), Lithium Carbonate (Li_2CO_3), and Lithium Hydroxide (LiOH) were purchased from Sigma Aldrich. Li_2CO_3 and K_2CO_3 powders were blended thoroughly in the eutectic 1.63:1 molar ratio with a small amount of water using a mortar and pestle. Aqueous LiOH was added in various amounts to the eutectic blend, and the resulting slurry was again mixed and then dried at 350°C for 16 hours. Experiments were conducted using 0, 15, 25, 45, and 100% LiOH by mole.

4.2.1.2 Salt Characterization

To ensure proper synthesis of the eutectic mixtures, samples of the molten salts were synthesized and characterized by differential scanning calorimetry (DSC) using a Discovery DSC 250 from TA Instruments. Heating ramp scan rates of 10°C were applied under a nitrogen atmosphere, and results are provided in Figure 4-5.

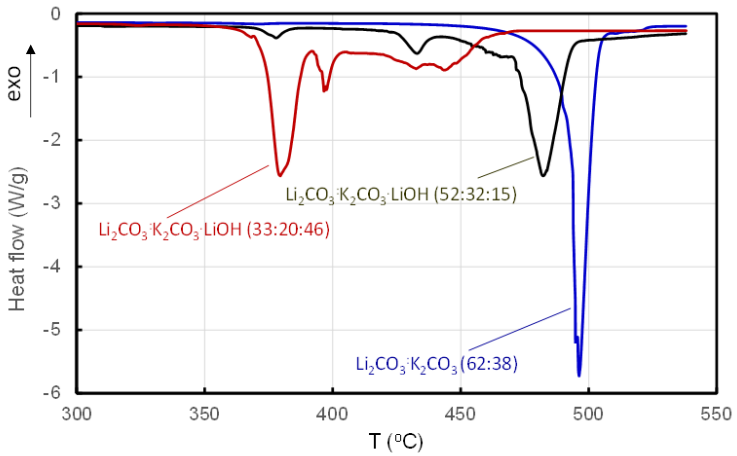

Figure 4-5: Differential Scanning Calorimetry of Eutectic Li_2CO_3 K_2CO_3 LiOH mixtures

The eutectic 0.68:0.32 Li_2CO_3:K_2CO_3 in blue displays a melting peak right before 500°C as anticipated from the phase diagram in Figure 4-3, indicating that the mixing procedure induces the desired chemical mixing. The anticipated melting point depression is observed in the hydroxide mixtures, confirming the desired mixtures are formed.

4.2.2 Methods and Materials

4.2.2.1 Experimental Setup

In order to perform the desired electrolysis experiments in a controlled temperature/gas environment, a custom tube furnace setup was designed and constructed, shown below.

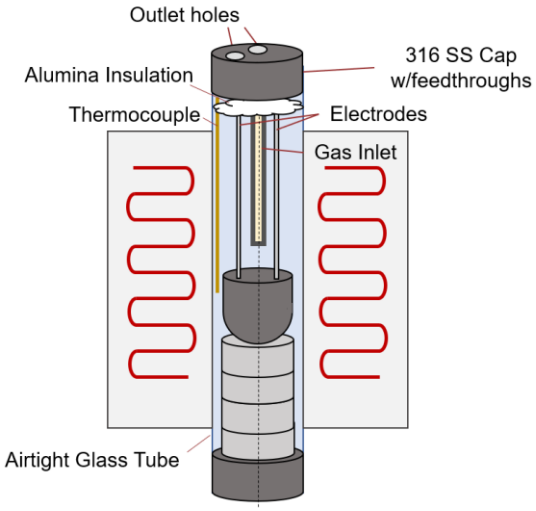

Figure 4-6: Depiction of experimental setup used for electrolysis in this work

The furnace is an MTI OTF-1200X, rotated for a vertical tube alignment. The quartz glass tube, steel endcaps, alumina feedthroughs were sourced from MTI. An Omega K-type thermocouple was used to ensure internal temperature conditions matched the furnace setpoint. Alumina firebricks were cut to size with a gas channel in the bottom and used to support the crucible inside the tube. A notable difference between this configuration and that described in Chapter 2 is that the top is not entirely sealed: two ¼" feedthroughs are left open, partially obstructed by the gas inlet and thermocouple, as waxy products of the seaweed/LDPE decomposition could not be safely passed through the pressure regulator at the bottom outlet. Fluffy alumina insulation was used at the top of the furnace to slow the gas exchange and minimize radiative heat loss to the lid. It is important to note that while the setup had significantly reduced oxygen presence due to continuous purging of N_2/CO_2 near the sample, some amount of atmospheric air could still pass in and out of the tube, and therefore the atmosphere was not entirely controlled. The setup was constructed inside of a fume hood to ensure safe operation and off-gassing.

4.2.2.2 Experimental Methods

Salts in the desired ratios were prepared as detailed in 4.2.1.1 above and loaded into the experimental apparatus. The anode consisted of a nickel crucible (99.5%, Sigma Chemical Company), and the cathode was a Fi-Shock WC-14200 14 Gauge galvanized steel wire coiled into a disc 1 cm across. Nickel was selected for its fast oxygen evolution kinetics and promotion of nucleated CNT growth[50], and galvanized steel was selected for the catalyzing effects of zinc and iron.[49]

The salt was initially melted under nitrogen and subjected to several cycles of cyclic voltammetry at 500°C. The purge gas was then switched to CO_2 for half an hour, and electrolysis experiments were conducted by applying a constant current of i = -240 mA for 1 hour (this translates to a current density of 120 mA/cm^2, using the surface area of the coiled disc).

After completion, the cathode was retracted from the crucible, and the system was allowed to cool. The product and frozen salt were removed from the cathode by sonication in deionized water (0.5 h). The product was then purified from the residual carbonates by dialysis of the suspension against 1% nitric acid (membrane cut-off weight, 12-14 kDa) followed by the particle removal, washing in deionized water and lyophilization.

4.2.3 Results

4.2.3.1 Electrolysis Results

We define a coulombic efficiency for the carbon electrodeposition as:

$$C_e(\%) = 100 \times \frac{M_{Measured}}{M_{Theoretical}} \qquad \text{Eq. 4-10}$$

Where $M_{experimental}$ is the mass of purified carbon product removed from the cathode. $M_{Theoretical}$ is the theoretical mass, calculated as (Q/nF) × (12.01 g C mol^{-1}), where Q is the time integrated charge passed during electrolysis, F is the Faraday constant (96485 A s mol^{-1} e), and n=4 mol^{-1} is

the reduction number of tetravalent carbon. The obtained Coulombic efficiencies are shown in Figure 4-7.

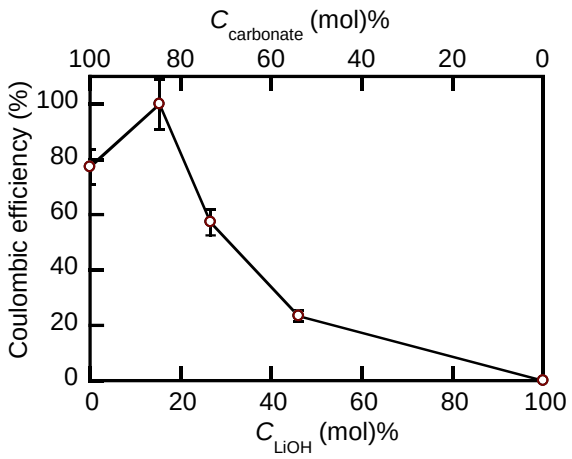

Figure 4-7: Effect of initial LiOH content (C_{LiOH}, mol%) and initial carbonate content ($C_{Carbonate}$, mol%) of the Li_2CO_3/K_2CO_3/LiOH electrolyte on the Coulombic efficiency of CO_2 electrosplitting process at 500C. The electrolyte Li_2CO_3/K_2CO_3 mol ratio was set at eutectic 1.63

The results demonstrate that both high initial concentrations of carbonate ions (CO_3^{2-}) and lithium in the molten electrolyte are required for the efficient conversion of CO_2 into carbon, according to the well-established mechanism of the 4-electron reduction of the carbonate ions to carbon. Our results (Figure 4-7) demonstrate that the effect of LiOH addition to the eutectic blend of two molten carbonates is the additive result of two opposing trends. That is, the enhancement of the overall lithium content in the composite by approximately 1 wt% at C_{LiOH}~15 mol% enables approximately 20% enhancement of the carbon product yield and Coulombic efficiency. However, further "dilution" of the carbonate by LiOH and decrease in $C_{carbonate}$ leads to a precipitous drop in the production of carbon, with the initially pure LiOH electrolyte failing to result in any carbon formation under the conditions of our experiment.

There are two major limitations that should be noted on this study. The setup developed in 4.2.2.1 does not have gas chromatography capabilities, so it is unclear whether or how much hydrogen or methane were evolved during electrolysis. It should be noted that the electrolysis experiments were conducted under CO_2 to ensure that carbonates could be replenished as they were electrolyzed; it is unclear how much of the hydroxide was converted to carbonate as the experiment progressed.

The carbon product obtained via electrosplitting of the optimal C_{LiOH}~15 mol% was examined via scanning electron microscopy (FEI/Philips XL30 FEG ESEM).

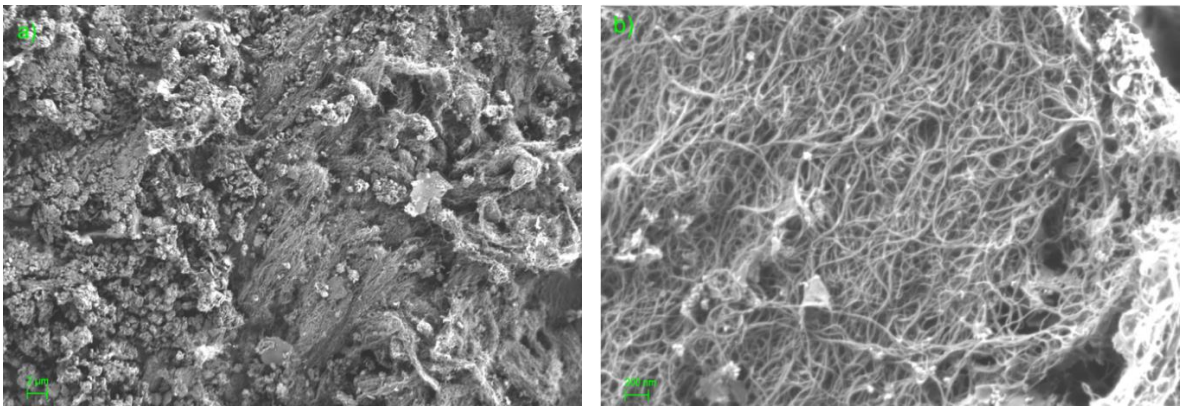

Figure 4-8: Electrolysis Product from Li_2CO_3/K_2CO_3 with 15% LiOH added, at a) 17.4kx magnification and b) 22.62kx magnification

Small quantities of amorphous carbon and unpurified salt are present in Figure 4-8a, but the vast majority of the product shown takes the form of a carbon nanotube wool. This indicates high efficiencies in the desired reactions.

4.2.3.2 Cyclic Voltammetry of Carbonate/Hydroxide Salts

To establish a baseline for comparison, here we present a cyclic voltammetry of the $(Li_{0.62}K_{0.38})_2CO_3$ + 13%LiOH salt used in the subsequent ATT experiments.

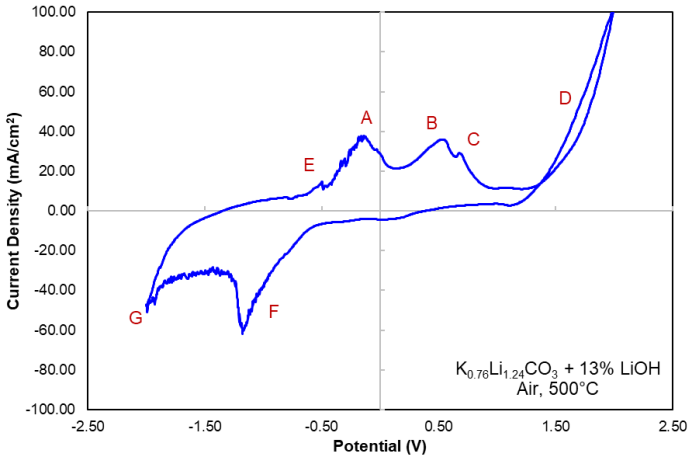

Figure 4-9: Cyclcic Voltammetry of $(Li_{0.62}K_{0.38})_2CO_3$ + 13% LiOH, using galvanized steel cathode and a nickel crucible anode at 500°C in air. Peaks are described below.

The decision to stop the cyclic voltammetry at 2V was in experimental error, as this was an early trial. From the literature, the peaks labelled are suggested to be the following79,82,83

A) Oxidation of the carbonate ion, according to
$CO_2^{2-} + 0.5O_2 + 2e^- \rightarrow CO_3^{2-}$
This reaction is typically used as a reference voltage in carbonate electrolysis studies.

B) Evolution of (H_2):
$$2OH^- + 2e^- \rightarrow H_2 + 2O^{2-}$$

C) Evolution of methane (CH_4):

$$CO_3^{2-} + OH^- + 8e^- \rightarrow CH_4 + 7O^{2-}$$

D) Electrodeposition of potassium:

$$K^+ + e^- \rightarrow K$$

E) Oxidation of nickel

$$Ni + CO_3^{2-} \rightarrow NiO + CO_2 + 2e^-$$

F) Reduction of nickel II oxide to nickel

$$NiO + 2e^- \rightarrow Ni + O^{2-}$$

G) Reduction of carbonate and carbon deposition, according to

$$CO_3^{2-} + 4e^- \rightarrow 3O^{2-} + C$$

While not shown in this CV, it should be noted that the magnitudes of current obtained at the carbonate reduction peak greatly exceed those of gas evolution: if it is permissible that some portion of the electrical energy input is used to convert H_2O to H_2 at a high overpotential, this suggests the salt should be regenerable to OH in-situ using the method described earlier.

4.3 Preliminary Investigation of Concurrent ATT/Carbonate Electrolysis

To investigate the potential viability of a combined electrolysis/alkaline thermal treatment process, experiments were conducted simulating concurrent gasification and electrolysis at the gram scale. These experiments are conducted by adding seaweed and LDPE to simulate the effects of biomass and plastic waste on the process. Brown seaweed (Saccharina japonica) from the coastal waters of Wando Island, Korea was utilized for this study, with a total solid ash content of 28.3 wt.% and a moisture content of 7.8 wt.%. The seaweed was ground to a particle size of less than 150 micrometers. For the representative plastic species, polyethylene powder (<500 micron, 99% pure, Alfa Aesar) was utilized due to its relative production and major presence as a marine surface plastic pollutant with a carbon content reported of about 85 wt.%.

Due to limitations of the experimental setup, it is not possible to carry out the full alkaline thermal treatment process under steam; therefore, we aimed to gasify the inputs under nitrogen for partial replication of the process.

4.3.1 Thermogravimetric Analysis

To investigate differences in the reactions between hydroxide salts and seaweed or LDPE under nitrogen, thermogravimetric analysis was conducted in a platinum pan using a Q50 TGA (TA Instruments). To examine interactions between the seaweed or LDPE and salt, we first conducted individual experiments to examine the weight loss profile of each material under nitrogen at a heat rate of 10°C/min under 60cc/min of nitrogen, matching the thermal profile used in experiments performed by collaborators in the Park Group. We then conducted experiments at the same conditions heating molten salt in the presence of seaweed or LDPE. Using weighted averages of the individual curves, we compared “predicted” behavior with no interaction to “actual” behavior of seaweed or LDPE in salt. If ATT reactions occurred, we would expect a net weight increase in the system weight from predicted to actual, as carbon would be affixed by the hydroxide species instead of off-gassing. It is important to note that mass transport and kinetics are confounding variables in these experiments. Slower or quicker weight losses could be attributed to mass transfer differences due to sample size rather than retention due to reaction. In the experiments involving

KLiOH and K_2CO_3/Li_2CO_3+LiOH, the salts were melted to 400C and returned to room temperature prior to the run to eliminate excess water and allow formation of the eutectic mixture.

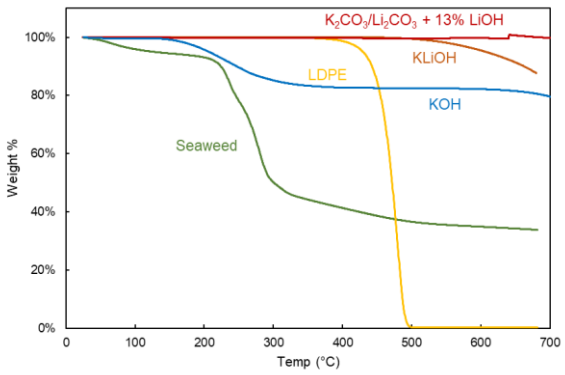

Figure 4-10: Thermogravimetric Analysis of LDPE, Seaweed, KLiOH, KOH, and eutectic carbonate salt with 13% LiOH individually at 10C/min under nitrogen

As individual components, seaweed and LDPE both demonstrate significant weight losses upon heating. Seaweed expels water gradually out to 200°C, after which it begins to char and loses almost half its weight between 200°C and 300°C. LDPE melts and remains largely unchanged until 400°C, fully decomposing and vaporizing as low molecular weight hydrocarbons between 400°C and 500°C.

KOH demonstrates weight loss between 200°C and 300°C, suggesting desorption of water contained in the powder prior to melting. KLiOH is known to melt at 300°C; LiOH and KOH typically do not fully decompose until 924°C and 1327°C respectively, but some degree of weight loss is observed after 550°C. It is likely that the vapor pressure of these species becomes non-negligible at elevated temperatures, and this represents evaporation of the species or water release. K_2CO_3/Li_2CO_3+13% LiOH has a higher melting point and does not result in noticeable weight loss over the temperature range studied, lending credence to this vapor pressure hypothesis.

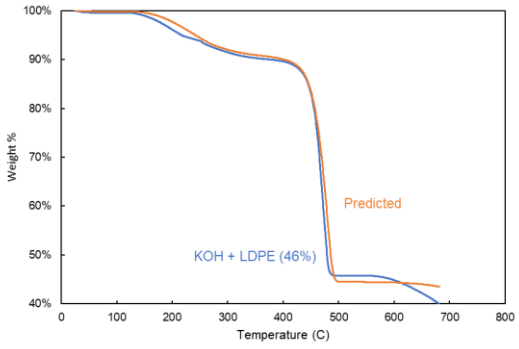

Figure 4-11: TGA Analysis of KOH with LDPE (46%) under N_2 heated at 10°C/min. Predicted curves are a weighted average of individual curves from Figure 4-10

KOH and LDPE mixed and heated together show almost no deviation from the weighted average of their individual temperature/weight profiles, indicating no strong interaction; the LDPE is decomposed and vaporized regardless of the salt present.

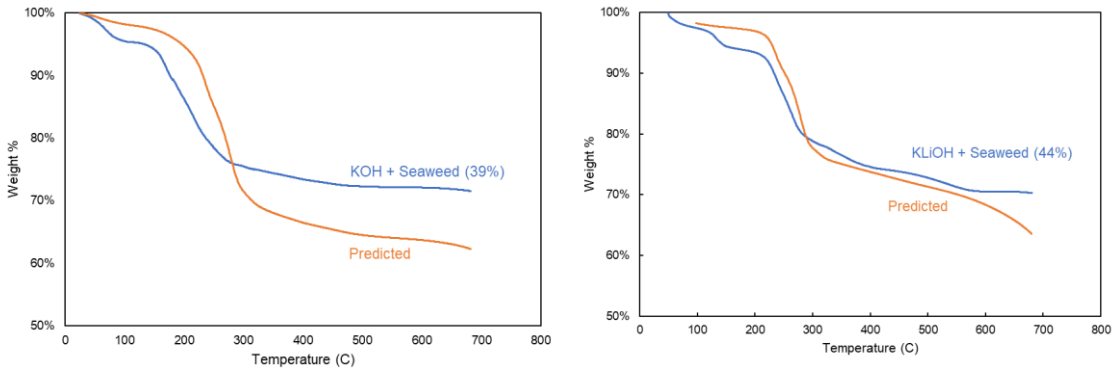

Figure 4-12: TGA Analysis of KOH with seaweed (39%) and pre-melted LiKOH with Seaweed (44%) under N2, heated at 10°C/min. Predicted Curves are a weighted average of individual curves from Figure 4-10

In both seaweed/hydroxide salt experiments, the predicted profile overestimates the weight out to 300°C and then underestimates the weight profile thereafter. The deviation is insignificant in the case of pre-melted KLiOH compared to powdered KOH. The underestimated final weight suggests that some amount of carbon could be sequestered in the form of carbonates, or that intermixing of the molten salt and seaweed ash slows the rate of hydroxide evaporation or release of species from the seaweed. In either case, it is likely that these conditions deviate significantly from ATT reaction conditions, and further study would be required after these experiments to make a definitive statement on the plausibility of concurrent gasification and electrolysis.

4.3.2 Electrolysis Study: Methods and Materials

Salt and crucible preparation are carried out in the same manner established in section 4.2.2.2. Prior to experimentation, 8% LDPE or 8% seaweed by mass were blended into the unmelted salt powder.

In the seaweed experiment, 40 cc/min of N_2 was purged for 30 minutes, followed by heating to 500°C in 1 hour and isothermal operation for an additional hour. During isothermal operation, cyclic voltammetry measurements were taken to examine transient effects.

In testing with LDPE, the sample was brought to 600°C and pre-melted under nitrogen for 90 minutes at 600°C to simulate gasification. After cooling and re-melting, the experiment proceeded as in the seaweed case to determine the effects of residual LDPE.

4.3.3 Results: Electrolysis in the Presence of Seaweed

Prior to electrodeposition at constant current, cyclic voltammetry measurements were performed to determine the effects of seaweed on the electrolyte.

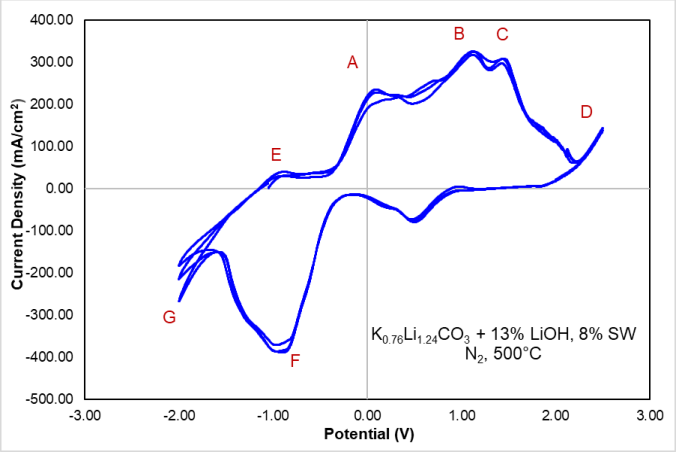

Figure 4-13: Cyclic Voltammetry of $(Li_{0.62}K_{0.38})_2CO_3$ + 13 mol% LiOH and 8wt% SW at 500C after 70 minutes in N_2

The peaks observed in the CV obtained represent a 1:1 correspondence with those shown in Figure 4-9, suggesting that the desired electrochemical reactions proceed without interference from seaweed ash and char. A chronopotentiometry experiment was then conducted at 120 mA/cm^2 for one hour, and the cathode was retracted and cooled. The obtained materials are shown in Figure 4-14.

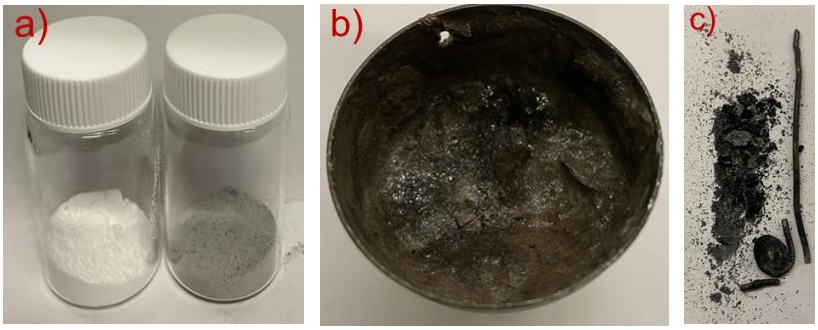

Figure 4-14: Materials after seaweed experiment, a) salt from the bulk before (left) and after (right), b) crucible after electrolysis, c) cathode and recovered carbon product and ash. CNTs are clearly distinguishable from ash.

Ultimately, 40 mg of product were recovered after purification, and elemental analysis indicated 83.3% carbon. This corresponds to a coulombic efficiency of 88%. However, inspection using scanning electron microscopy suggests that no carbon nanotubes were present, and the product instead primarily took the form of amorphous carbon. Carbon nanotubes were observed under TEM, suggesting that CNT formation was inhibited but not entirely suppressed.

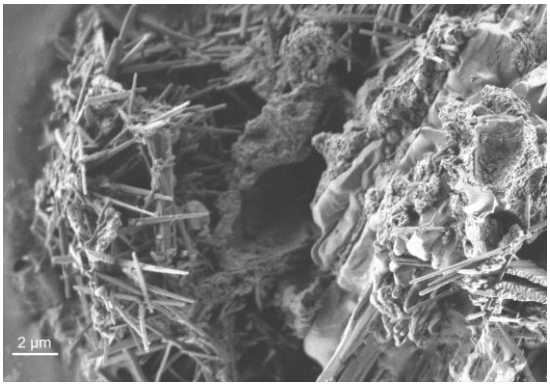

Figure 4-15: SEM Image characteristic of product recovered from electrolysis in the presence of seaweed. A solid amorphous carbon structure is coated in residual oxide crystals from the seaweed ash

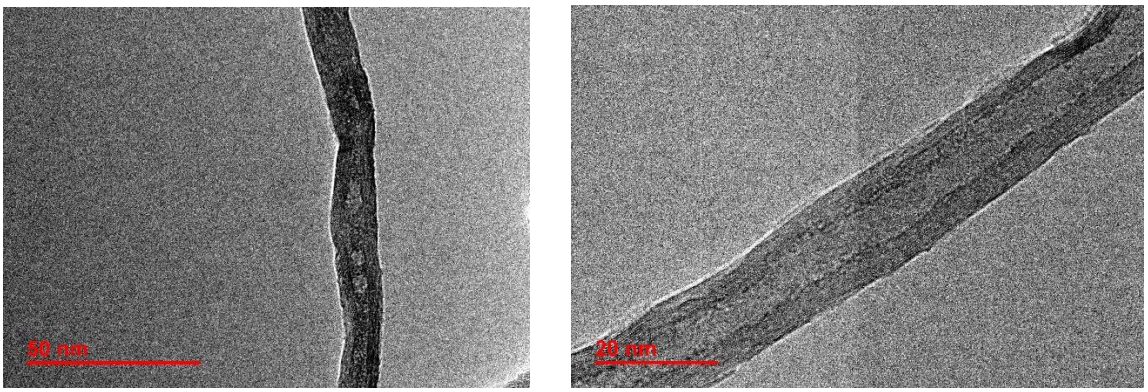

Figure 4-16: Representative TEM images of product obtained by electrolyzing $(Li_{0.62}K_{0.38})_2CO_3$ + 13 mol% LiOH with 8wt% seaweed, confirming multiwalled carbon nanotubes.

4.3.4 Results: Electrolysis in the Presence of LDPE

Figure 4-17: Salt ($(Li_{0.62}K_{0.38})_2CO_3$ + 13 mol% LiOH with 8wt% LDPE) with embedded electrode crucible after 90 minute pre-treatment at 600°C in N_2

From Figure 4-17, it can be seen that unlike other experiments where the frozen salt formed a solidified mass attached to the crucible, the salt came out in a single disconnected piece after pre-melting. This likely indicates that the LDPE remained molten and was rejected to the outer surface as the salt froze in the middle and continued to boil off. We then re-melted and electrolyzed the salt, generating the CV profile shown in Figure 4-18.

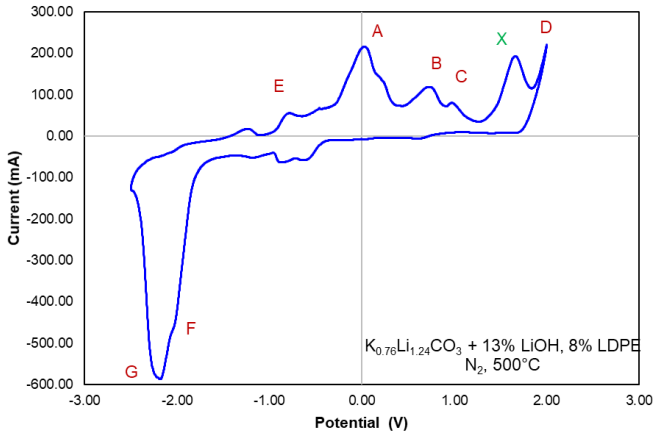

Figure 4-18: Cyclic Voltammetry Profile of $(Li_{0.62}K_{0.38})_2CO_3$ + 13 mol% LiOH with 8wt% LDPE at 500°C after 90-minute pre-treatment at 600°C in N_2 and an additional 70 minutes in N_2

All peaks observed in pure $(Li_{0.62}K_{0.38})_2CO_3$ + 13 mol% LiOH are again observed above, with a notable addition at 2V; this potentially represents oxidation of hydrocarbons at the nickel anode, but does not affect carbon deposition at the cathode.

After purification, 60 mg of product were recovered, of which 83.2% was found to be carbon through elemental analysis. This would correspond to a coulombic efficiency of 175%, indicating that some additional pyrolysis of the LDPE likely occurred. A significant portion of the product took the form of carbon nanotubes (shown in Figure 4-19), suggesting that the gasification of LDPE does not interfere with the electrodeposition.

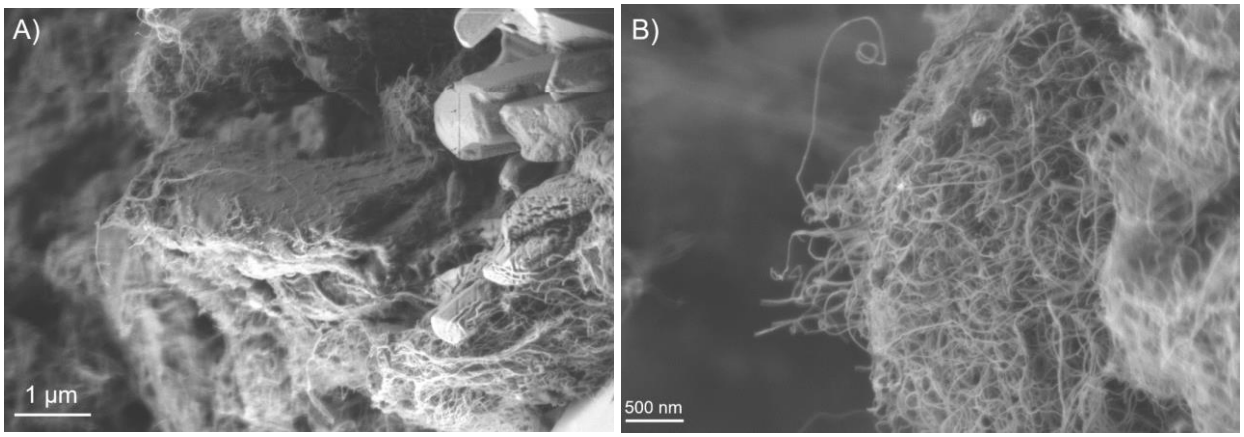

Figure 4-19: Representative SEM images of product obtained by electrolyzing $(Li_{0.62}K_{0.38})_2CO_3$ + 13 mol% LiOH with 8wt% LDPE. A is at 14.2kx magnification, and B is 20.2kx

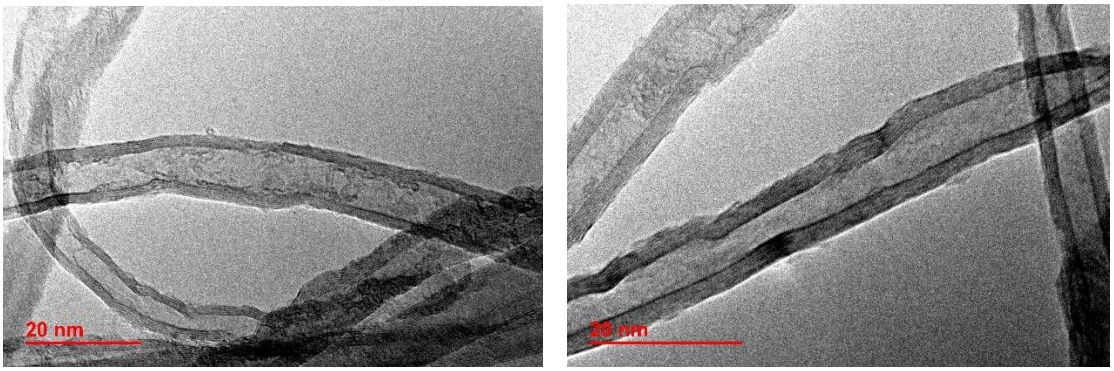

Figure 4-20: Representative TEM images of product obtained by electrolyzing $(Li_{0.62}K_{0.38})_2CO_3$ + 13 mol% LiOH with 8wt% LDPE, confirming multiwalled carbon nanotubes.

5 Electrochemically Mediated Alkaline Thermal Treatment Process – Technoeconomic Comparison

The original Alkaline Thermal Treatment (ATT) concept paper presents a simplified analysis of the ATT process, tabulating reaction enthalpy values to calculate a nominal energy required per unit of hydrogen produced[64]. However, the analysis presented is limited to the laboratory scale; it does not account for practical considerations such as sensible heating requirements of inputs and products or potential for heat recovery in the system. In the following study, we aim to perform a system-level analysis of the process to refine their estimation of an achievable energy per unit of hydrogen for nominal comparison to existing methods of hydrogen production from biomass. We also aim to estimate a total cost per unit of hydrogen both to determine the cost breakdown of the process and associated facilities and for comparison with the DOE Technical Targets for Hydrogen Production from Biomass84. From there, we analyze a modified process using an electrochemical regeneration pathway using the same framework. While the work in this thesis has examined the possibility of in-situ regeneration, this work assumes a two-step regeneration process, first removing solid ash.

5.1 Technoeconomic Analysis of Steel Slag Regenerated Alkaline Thermal Treatment

5.1.1 Analysis Framework and DOE Target Criteria

To evaluate the efficacy of emerging hydrogen production technologies from biomass, the United States Department of Energy (DOE) has defined target metrics for energy efficiency, capital cost, fixed operating cost, and variable operating cost for biomass gasification and pyrolysis systems85 (Table 1). Meanwhile, costs and energy impacts associated with conventional grey hydrogen production are well-documented. Therefore, process-level modelling of the energy and economic impact of emerging molten salt gasification technologies is necessary to compare their efficacy to conventional green, blue, and grey hydrogen production pathways. To inform process-level technoeconomic and environmental considerations for oceanic biomass gasification in molten salts, thermodynamic, material flow, and economic factors must all be considered in the presumed tradeoff between energetic and capital efficiencies. Therefore, characterization of the proposed pathway for hydrogen production from oceanic biomass is conducted along two main avenues:

1. Mass and energy balances across reagent usage and byproduct generation to develop a high-level life cycle inventory for determination of energy requirements for molten salt gasification of oceanic biomass, and to identify the processing steps with the highest potential for waste heat recovery
2. Preliminary cost assessment to identify investment bottlenecks in the proposed hydrogen production process and to estimate the relative economic burden of waste heat recovery versus major processing unit operations

Analysis methodologies for mass and energy balances and cost estimation are detailed in the following sections.

Metric	Cost
Hydrogen levelized cost / kg H2	$2.00
System capital cost / kg H2 capacity	$3.33
Feedstock cost / kg H2	$0.90
Fixed Operating Cost / kg H2	$0.20
Variable Operating Cost / kg H2	$0.30

Table 5-1: 2020 DOE Hydrogen Production Targets85

Mass and Energy Balances for Molten Salt Gasification of Oceanic Biomass

To evaluate material flows and energy requirements for hydrogen production via molten salt gasification of oceanic biomass, a high-level life cycle inventory will be conducted across all major processing steps outlined in Figure 5-1**.** Using mass and energy balances across individual unit operations, material feed requirements, energy input, and waste heat generation associated with hydrogen production will be determined. Proposed system boundaries for the mass and energy balances are inputs of wet seaweed, water, electricity, and natural gas for process heating (as deemed necessary from process energy balances), with outputs of separated hydrogen, carbon dioxide, and steam gasses, electricity produced from waste heat, and ash. Our analysis may therefore be viewed as a "gate to gate" study through the lens of the conventional life cycle inventory methodology86. To distinguish energy requirements for hydrogen production versus energy that ultimately went to producing byproduct electricity, allocation of material and energy flows between the two products will be conducted following the ISO 14040 hierarchy87:

1. Isolation of energy and materials inputs for processing steps directly tied to the production of hydrogen or the production of electricity from waste heat
2. Allocation of energy and materials inputs between hydrogen production and electricity production from waste heat based on physical relationships, such as usable product energy
3. Allocation of energy and materials inputs between hydrogen production and electricity production from waste heat based on non-physical relationships, such as market value

A functional unit of 1 ton of hydrogen will be adopted for normalization of energy input to production capacity. While in reality sodium compound and calcium compound will have to be gradually purged and replenished in the system to avoid the buildup of impurities in material recycle loops, per functional unit of hydrogen these impacts are taken to be negligible and will not be accounted for in our analysis.

Mass and energy balances will be conducted in the thermodynamic limit using data and thermodynamic correlations from FactSage 7.3. Real-world energy and material efficiencies will be estimated for individual processing steps using reported energy and water usage for similar processes as tabulated in the ecoinvent 3.6 database. These data tabulated for each processing step will form the basis of our thermodynamic model and life cycle inventory for hydrogen production via molten salt gasification of oceanic biomass.

5.1.2 Thermodynamic Analysis of the Alkaline Thermal Treatment Process

5.1.2.1 Overview and Assumptions

Compared to the original process outlined by Zhang et. al.[64], several modifications have been made to enable efficient heat recovery, illustrated in the updated process configuration in

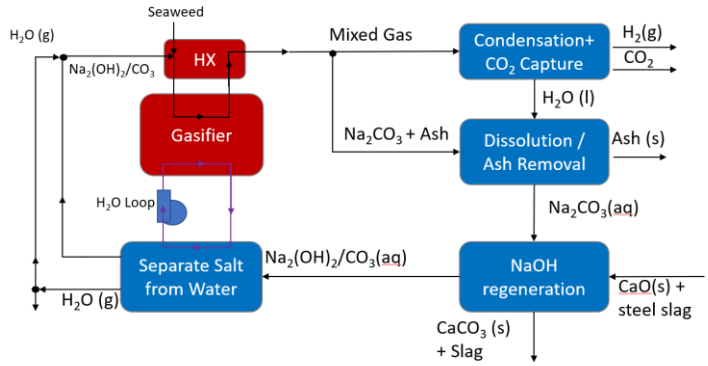

Figure ***5-1***.

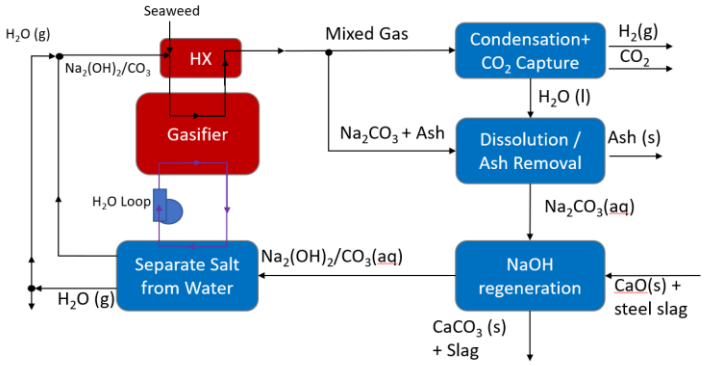

Figure 5-1: Alkaline Thermal Treatment Process for hydrogen production from oceanic biomass with incorporated heat recovery

New additions include utilization of sensible heat in the products leaving the reactor is used to preheat the incoming reactants. Pressurized water also flows through the reactor to absorb the heat released by gasification to provide heating to boil the water out of the treated salt – the overall process is endothermic due to the quantities of water that must be treated, so there is insufficient heat to recover electricity.

The following simplifying assumptions were made to compute the mass and energy balance results:

Gasifier Reactions and Mass Flows

1. The seaweed is assumed to be sun-dried, with a mass composition of 10% moisture, 28.3% ash, and 61.7% volatiles. The volatiles here are modeled as cellulose ($C_6H_{10}O_5$) due to wide variation in seaweed composition; the seaweed analyzed in the original ATT paper had a stoichiometric balance of $C_{5.5}H_{10}O_{3.4}$, so this is a fairly conservative estimate.
    a. The original paper indicates that over 60% of the ash is K_2O, so the thermal properties of K_2O are used as a substitute for ash throughout this analysis.

2. An 8:1 steam to volatile molar ratio flows through the reactor. It is worth noting that because this is a continuous process, the actual ratio of steam to volatiles in the reactor at any given time can be higher – this value is higher than the stoichiometric consumption rate, and allows its use as a sweep gas for the hydrogen. It is difficult to tell if this is an over- or underestimate, as it was based on supercritical water gasification technologies which are analogous but much more steam intensive.
3. In the reactor, we assume that the following overall net reactions occur:

$$C_6H_{10}O_5 + 12NaOH + H_2O \rightarrow 6Na_2CO_3 + 12H_2 \quad \text{Eq. 5-1}$$

$$C_6H_{10}O_5 + 7H_2O \rightarrow 12H_2 + 6CO_2 \quad \text{Eq. 5-2}$$

The former represents alkaline thermal treatment, and the latter is decomposition of volatiles and subsequent steam reforming/ water gas shift. The original paper indicates that each of these reaction pathways occurs in equal quantities, but with only 71% efficiency (~8.5 mol H_2/mol volatiles). We assume process optimization at scale that leads to a stoichiometric efficiency near 100%. All unintended heat transfer is assumed to be captured in modelled thermal efficiencies. Reaction enthalpies are calculated using the enthalpies of formation at 500°C.

Water Loop

1. The water is pumped to 10 bar on each pass with an isentropic efficiency of 85%
2. Excess heat from the reactor is exchanged with water flowing through pipes in contact with the reactor at 10 bar, heating it from ambient temperature to 500°C.
3. A portion of this steam is used to boil the water in the salt regeneration tank, with 90% heat exchanger efficiency. The pressurized steam will condense at 180°C – the maximum temperature of the opposite stream - so this assumption is reasonable.
4. Any excess steam will be used to provide electricity through a turbine at a first law efficiency of 35%, operating between 10 bar at 500°C and 99°C at 1 bar.

Preheater

1. It is assumed that seaweed enters the preheater at ambient temperature, and that the salt and water are carried over from the causticizing process. They are preheated at 100% effectiveness, as the emerging thermal mass is greater than that being input.
2. In a real system, there is typically an upper bound on the allowable temperatures for biomass preheating before pyrolysis would occur; this consideration is neglected.
3. The products emerge from the preheater at approximately 180°C, and this heat is rejected to the environment.

Slag Composition

The assumed composition of the slag utilized in this analysis is sourced from the Nippon Slag Association web page, tabulated below:

Component	Mass %
CaO	41.7
SiO_2	33.8
T-Fe	0.4
MgO	7.4

Al_2O_3	13.4
S	0.8
P_2O_5	<0.1
MnO	0.3

Table 5-2: Assumed Slag Composition

CaO is the primary component of interest, as it will react to form $Ca(OH)_2$ (aq) and ultimately regenerate our soda ash according to:

$$Ca(OH)_2(s) + Na_2CO_3(aq) \leftrightarrow 2NaOH(aq) + CaCO_3(s) \quad \text{Eq. 5-3}$$

This replacement reaction does not proceed to completion; under normal industrial operating conditions, a regeneration efficiency of 80-85% can be achieved88. Of the remaining species, MgO and SiO_2 are very slightly water soluble, but will remain as a solid upon melting the molten salt and can either be removed or pass through the reactor without inducing side reactions. Sulfur will form dilute sulfuric acid upon water addition, but this will be readily neutralized by the caustic species and can be readily disposed as liquid waste after passing through the reactor as SO_x. P_2O_5 will dissolve to form phosphoric acid, but this is assumed to be negligible due to the small quantity in the slag.

In the literature, on-site steel slag directly from the blast furnace is typically considered to be industrial waste, available free of charge. However, the cost of granulation and of transportation can be significant; several sources quoted this resulting cost at $80/metric ton, and this value was adopted for simplicity89. A transportation analysis similar to that performed for seaweed could be performed to minimize this value, as could an analysis of crushing or granulating on-site depending on the plant sizing, but these considerations are neglected for simplicity.

Gas Separation

In a standard steam methane reforming plant, often hydrogen separation is performed using pressure swing adsorption. It is difficult to ascertain what method of gas separation would be employed in an actual ATT system, as sulfur species and unforeseen hydrocarbons could impact the process. To provide a reasonable estimate, the system capital cost was estimated as a more expensive cryogenic gas separation unit, and electricity consumption was calculated by assuming gas separation at a 20% second law efficiency.

The DOE cost metrics do not account for H_2 pressurization and transport, so these considerations are neglected. These metrics also assume a process that is approximately carbon neutral rather than carbon negative – therefore, liquefaction and storage of CO_2 are also not considered.

NaOH Regeneration

1. The Na_2CO_3/$Ca(OH)_2$ metathesis reaction is assumed to proceed at an efficiency of 85% based on similar values achieved in the paper pulping industry.
2. The concentration of NaOH in water is assumed to be 82 g/L at the outlet based on industrial causticizing effectiveness curves. This value is well below the NaOH solubility limit of 418 g/L88.

3. It is assumed that dehydration occurs at 101°C. This is normally conducted under slight vacuum conditions at 180°C in paper pulping processes, but the salt and water will be re-mixed in the reactor regardless because there are no real adverse effects from any residual water. Therefore, the process can occur under ambient pressure.
4. It is assumed that dissolved species have no impact on the specific heat capacity of water, and enthalpies of dissolution, solidification, and causticizing are neglected
5. CaOH present in the outgoing stream is neglected; in a real process, the ~15% CaOH in the salt would absorb CO_2 in the outlet stream and eventually precipitate in the next pass without impacting the ATT reactions, so this assumption will simply result in an increase in work required for gas separation.

5.1.2.2 Thermodynamic Analysis: Results

Energy and Mass Balances

Reactor:
Molar inputs and outputs for the ATT reactor are tabulated below:

Species	In (mol/kg SW)	Out (mol/kg SW)
H_2O	31.83	15.92
$C_6H_{10}O_5$	3.979	0
Ash (K_2O)	2.704	2.704
Na_2CO_3	4.2135	16.1517
NaOH	23.8764	0
H_2	0	47.75
CO_2	0	11.93

Table 5-3: Reactor molar balances in model of baseline ATT proces

Steam Loop
The reactor rejects 5.09MJ/kg seaweed to the steam loop, or enough to heat 83 mol/kg of steam from 25°C to 500°C at 10 bar. However, assuming 90% heat exchanger efficiency, 511 moles of steam at this temperature would be required to boil all the water used in regeneration, so additional heat must be imported. The pump consumes 1.916 kJ/kg of electricity to pressurize and circulate the water throughout.

NaOH Regeneration

Species	Inflow (mol/kg SW)	Outflow (mol/kg SW)
H_2O	621.5894	621.5894
Na2CO3	16.1517	4.2135

NaOH	0	23.8764

Table 5-4: NaOH Regeneration step mole balances

1.8463 kg slag/kg seaweed is consumed in this step (contributing $0.147/kg SW to operating expenditures). It is noted that the water used in this step exceeds that fed into the gasifier by nearly twentyfold, representing a loss of energy unless re-used in another process.

Gas Separation

After the steam is allowed to condense off with SOx species, the minimum work of separation for the remaining H_2 and CO_2 is given by the change in gibbs free energy:

$$W_{Min} = G_{H2,Out} + G_{CO2,Out} - G_{Mix,In} \quad \text{Eq. 5-4}$$

The minimum work evaluates to 263 kJ/kg SW. With a 20% second law efficiency, this is realized as a system electricity penalty of 132 kJ/kg SW.

Solids Handling

The industrial handbook estimates power requirements of solids handling at 12.5 kWh/ton. Therefore, the ash requires 11.5 kJ/kg SW of electricity

5.1.3 Economic Assessment for Alkaline Thermal Treatment of Oceanic Biomass

5.1.3.1 Economic Analysis Methodology

The economic viability of hydrogen production via molten salt gasification of oceanic biomass is evaluated by estimating the fixed operating cost, variable operating cost, and capital cost of the

Country / Region	Location Factor
United States, Gulf Coast	1
United States, East Coast	1.04
United States, West Coast	1.07
United States, Mid-West	1.02
Canada, Ontario	1
Canada, Ft. McMurray	1.6
Mexico	1.03
China, imported tech	1.12
China, local tech	0.61
Japan	1.26
Australia	1.21
India	1.21
Middle East	1.07
France	1.13
Germany	1.11

Table 5-5: Location factors for chemical plant capital cost[104]

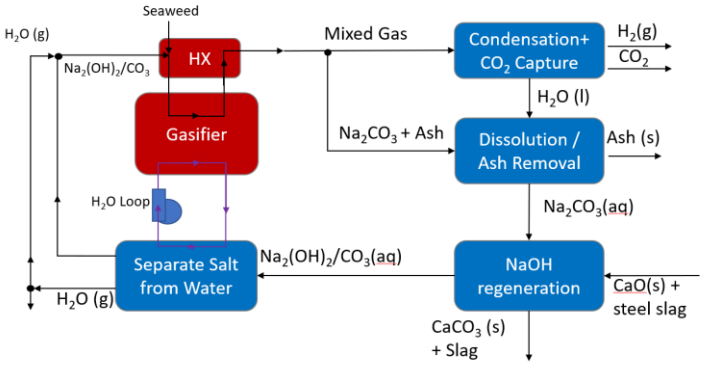

process summarized in Figure ***5-1***. Through amortization of the capital cost and normalization of the fixed and variable operating costs per unit of hydrogen, the cost per unit of hydrogen produced via molten salt gasification of oceanic biomass may be estimated and compared to DOE targets for total hydrogen production cost, capital cost, fixed operating cost, variable operating cost, and electricity usage cost (Table 5-1). Variable operating costs associated with reagent usage, energy usage, and waste management are readily determined from process mass and energy balances, reagent price data, and utilities data90,91. Fixed operating costs consist of factors including labor, maintenance, rent, taxes, insurance, interest, overhead, licensing, and royalties90,91. Labor costs are estimated through determining the number of operator shifts required in accordance with standard chemical plant procedures, with labor overheads (management, health insurance, etc) taken as some fraction of the plant operator labor cost90. Other fixed operating expenses are estimated through scaling total capital cost or total product revenue.

Capital costs, describing the extent of economic investment required for construction of a hydrogen production facility utilizing molten salt gasification, are readily scalable between regions using location factors, where C_A is the direct capital cost of the facility in location A, C_R is the total direct capital costs of the facility in a reference location, and F is the location scaling factor90:

$$C_A = F * C_R \qquad \text{Eq. 5-5}$$

Location scaling factors for capital cost estimation of chemical processes in different countries are included in Table 2. Globalization drives location scaling factors towards 1, while the capital cost of a facility increases based on its distance from the nearest industrial center and required development of local infrastructure90.

Capital cost may be estimated with different degrees of uncertainty, as outlined by the Association for the Advancement of Cost Estimating International92:

- Order of magnitude estimates (+/- 30-50%, “Class 5”): Derived from scaling laws relating total capital cost to production capacity based on previously-constructed facilities for similar processes
- Preliminary estimates (+/- 30%, “Class 4”): Derived from summing the capital costs associated with individual unit operations in the process, with scaling laws relating the capital cost of a unit operation to a relevant operating parameter for that unit operation (capacity, power, volume, etc)

- Definitive estimates (+/- 10-15%, “Class 3”): Derived from detailed piping and instrument diagrams and equipment sizes
- Detailed estimates (+/- 5-10%, “Class 2”): Derived from front end engineering diagrams and quoted equipment and construction costs
- As-bid estimates (+/- 5%, “Class 1”): Derived from complete process designs and negotiated with contractors

Methods of cost estimation for hydrogen production via seaweed gasification using molten salts are limited due to the lack of capital cost data for similar processes, making a Class 5 cost estimate as described above unfeasible. Meanwhile, since hydrogen production via molten salt gasification remains an emerging technology at this point, the lack of detailed process specifics and conditions hinders Class 1-3 estimates. However, the proposed flowsheet for hydrogen production via gasification in molten salts is largely based on unit operations that employ well-established reactor technology, making a cost estimation based on a summation of costs from individual unit operations feasible. Therefore, we propose a Class 4 study for estimating the capital cost of a molten salt oceanic biomass gasification facility.

Capital cost as considered herein consists of the total direct and indirect capital investment required for construction of the oceanic biomass gasification facility, and is estimated using the bare module method93. The bare module method consists of using equipment scaling laws of an exponential form to determine a free-on-board cost (FOB) for a unit operation, where A_{FOB} is a pre-exponential factor, n is a scaling exponent, and x is the relevant process parameter for which equipment cost scales by, often capacity, power, or vessel volume93

$$FOB = A_{FOB} * x^n \quad \text{Eq. 5-6}$$

The cost of the installed process module with supporting infrastructure (LM), consisting of the FOB plus construction, labor, materials, and supporting infrastructure, can be found by scaling the FOB by a labor and materials factor, A_{LM}93:

$$LM = A_{LM} * FOB \quad \text{Eq. 5-7}$$

Process Block	Process Module	Equipment Model	Scaling Exponent	FOB Pre-Exponential	L+M Factor	PM Factor	BM Factor	TM Factor	Model CEI / Year CEI	Scaling Pre-exponential	Scaling Metric
Gasifier	NaOH Melting	Cylindrical Furnace, Fired	0.74	375000	2	1.2	1.25	1.36	1000 / 607	928710	Heat Input / MW
	Molten Salt Reactor	Melting Cyclone Burner	0.49	1270000					1000 / 607	770890	Hearth Area / m^2
Ash Removal	Na_2CO_3 solidification	Flaker	0.6	152000	2.25	1.2	1.25	1.36	1000 / 607	423492	Drum Surface Area / m^2
	Heat Recovery / Steam Generation	Bayonet Heat Exchanger	1.33	656	1.53	1.2	1.25	1.36	1000 / 607	1243	Heat transfer surface area / m^2
	Na_2CO_3 Comminution	Milling / grinding circuit	0.65	311490			1.25	1.36	1000 / 607	321427	Solids flow / tonne / hour
	Na2CO3 Dissolution	Open, jacketed STR	0.53	20950	2.61	1.2	1.25	1.36	1000 / 607	67709	Working volume / m^3
	Ash filtration	Rotary drum filter, vacuum	0.34	116418	2	1.2	1.25	1.36	1000 / 607	288316	Drum volume / m^3

Water Gas Shift Reactor	Compressor	Compressor, reciprocating	0.79	4735	2.82	1.2	1.25	1.36	1000 / 607	16534	Drive Power / kW
	Reactor	Fixed Bed Catalytic PFTR	0.52	37066	2.7	1.2	1.25	1.36	1000 / 607	123925	Volume / m^3
Hydrogen Separation	Water Condensation	Barometric Condenser	0.6	2700	1.6	1.2	1.25	1.36	1000 / 607	5349	Water flow / L/s
	Air separation unit	Cryogenic distillation	0.6	7534					607 / 607	7534	Ton N_2 / year from air
Causticizing	$CaCO_3$ causticize	Open, jacketed STR	0.53	35615	2.61	1.2	1.25	1.36	1000 / 607	115105	Working volume / m^3
NaOH regeneration	Na_2CO_3 causticize	Open, jacketed STR	0.53	35615	2.61	1.2	1.25	1.36	1000 / 607	115105	Working volume / m^3
	$CaCO_3$ filtering	Rotary drum filter, vacuum	0.34	186269	2	1.2	1.25	1.36	1000 / 607	461306	Drum volume / m^3
	Water Boiling	Boiler, fired, packaged	0.92	320801	1.35	1.2	1.25	1.36	1000 / 607	536276	steam production, kg/s
	NaOH filtering	Rotary drum filter, vacuum	0.34	186269	2	1.2	1.25	1.36	1000 / 607	461306	Drum volume / m^3
	NaOH drying	Rotary kiln	0.84	1200000			1.25	1.36	1000 / 607	1238280	kg solid + liquid / s
Exhaust gas treatment	Dust collection	Electrostatic precipitator	0.39	149360	36				1000 / 607	3263815	M^3 gas / s
Electricity generation	Steam turbine and generator	steam turbine, generator	0.51	5771	1.6	1.2	1.25	1.36	1000 / 607	11434	Power / kW

Table 5-6: Capital Cost Curves93 for unit operations relevant for Hydrogen production through alkaline thermal treatment of seaweed

The physical module cost of the unit operation (PM), consisting of the LM plus taxes, freight, and insurance, is found by scaling the LM by a factor (A_{PM}) 93:

$$PM = A_{PM} * LM \qquad \text{Eq. 5-8}$$

The bare module cost (BM) of the unit operation, consisting of PM, field, and office expenses associated with construction of the unit operation are tabulated by scaling PM by a factor A_{BM}93:

$$BM = A_{BM} * PM \qquad \text{Eq. 5-9}$$

Finally, the total direct capital cost, also known as the total module cost (TM), is found by scaling BM by a factor A_{TM} to account for contractor fees, delay, and design change contingencies93:

$$TM = A_{TM} * BM \qquad \text{Eq. 5-10}$$

Therefore, the total direct capital cost associated with one unit operating and its supporting plant infrastructure is estimated as follows:

$$TM = A_{TM} * A_{BM} * A_{PM} * A_{FOB} * A_{LM} * x^n = A * x^n \qquad \text{Eq. 5-11}$$

Scaling relations for the direct capital cost of some relevant unit operations are included in Table 3. The total direct capital cost of the process is estimated as the sum of the TM for with all of the key unit operations. Indirect capital costs, such as arising from land, spare parts, legal fees, working capital, and startup expenses, are estimated from TM using similar scaling factors93. The sum of TM and indirect capital costs constitutes the total capital cost. Capital cost data

accumulated from different years is normalized to 2018 US dollars using the *Chemical Engineering Magazine's* Chemical Engineering Plant Cost Index (CEI)94.

To estimate a total cost per unit of hydrogen, the amortized total capital cost, including depreciation, fixed operating cost, and variable operating cost and totaled and normalized per unit of hydrogen90. This cost per unit of hydrogen constitutes a comparable metric to other hydrogen production processes95, as well as to the DOE hydrogen price target of $2.00 / kg for generation via biomass gasification.

5.1.3.2 Fixed Capital Cost Estimation for Hydrogen Production from Seaweed via Biomass Gasification

The capital cost (CAPEX) of hydrogen production from gasification of seaweed is estimated using Eqs 9-14, where relevant scaling factors are related to hydrogen production capacity via mass and energy balances. The US Department of Energy has set a target metric for CAPEX of $3330 / ton of H_2 capacity. As illustrated in Figure 3, the proposed alkaline thermal treatment for seaweed gasification is predicted to meet the DOE target at scales larger than 50 to 250 tons / day of H_2 production. As shown in Figure 5-3 (pie chart), solids handling processing steps pertaining to ash removal and NaOH regeneration via causticizing are predicted to be the largest individual contributors to capital cost, at 32% and 12% respectively. Water gas shift reactors and heat recovery equipment exhibit lower CAPEX, at contributions of 10% and 9% respectively. Despite the elevated temperature (~500 °C) of the seaweed gasification reaction, gasification is predicted to contribute a relatively small amount to CAPEX at just 9%, suggesting that hydrogen production via molten salt methods of gasification is not capitally prohibitive compared to conventional hydrogen production processing operations, such as the water gas shift reaction.

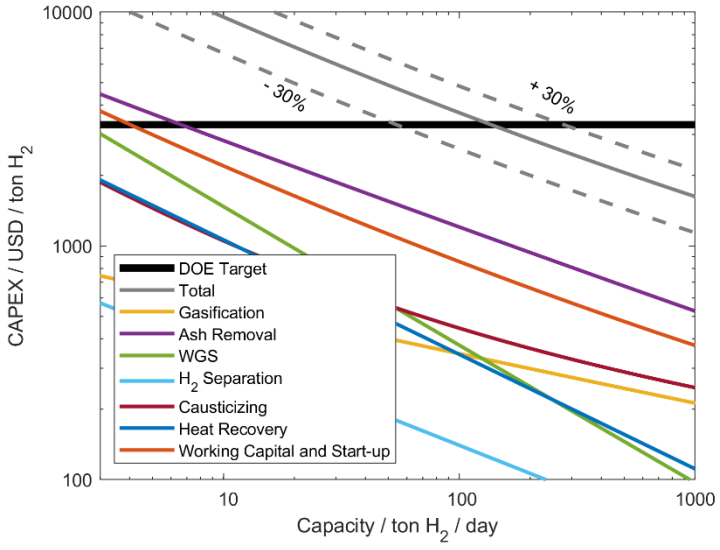

Figure 5-2: CAPEX as a function of hydrogen production capacity, with Class 4 Cost Estimation error bars of +/- 30% depicted. The DOE metric of $3330 / ton of H2 for CAPEX is predicted to be met at a processing scales larger than between 50 and 250 tons of H_2 per day

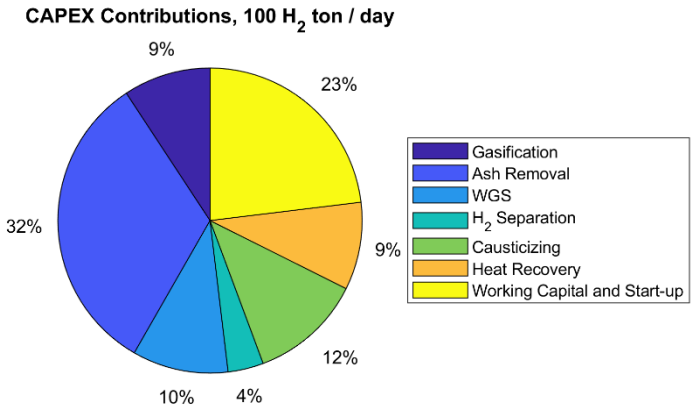

Figure 5-3: Estimated contributions to CAPEX at a scale of 100 t of H2 / day. Solids processing steps (ash removal, causticizing) are predicted to be the most expensive unit operations, while molten salt gasification is not expected to be cost prohibitive compared to conventional water-gas shift technology

5.1.3.3 Fixed Operating Cost Estimation

Fixed operating costs (Fixed OPEX) herein are taken to include plant maintenance, overhead, taxes, royalties, research and design, and labor. Such costs are dependent on plant capacity and design, but are obligations that exist regardless of the actual level of hydrogen production. Therefore, fixed OPEX may be estimated based on installed capacity, capital cost, the number of unit operations, and total production cost. The United States Department of Energy (DOE) specifies a target Fixed OPEX of $200 per ton of H_2 for biomass gasification, out of a total target OPEX of $500 per ton of H_2.

Maintenance, plant overhead, taxes, royalties, and research and design are generally estimated as fractions of the total direct capital cost, as outlined in Table X. Research and design expenses are generally assumed to be a fixed fraction of the total production cost, generally on the order of 5%. The total production cost for the purpose of estimation of research and design expenses is taken to be the DOE target metric for total OPEX of $500 / ton of H_2.

Labor expenses in modern chemical processing are generally more tied to the number and diversity of processing steps than the actual facility size. The number of operators required for a shift can be estimated from the number of solids and fluids processing steps (P_S and P_F) respectively, included in Table X:

$$\frac{operators}{shift} = \sqrt{6.29 + 31.7 * P_S^2 + 0.23 * P_F} \qquad \text{Eq. 5-12}$$

As shown in the relation above, solids processing steps are conventionally observed to be more labor intensive than fluids processing steps. For a continuous processing facility operating 350 days per year, four shifts are generally required. Labor overheads, supporting expenses such as healthcare, pensions, etc., are generally taken to be a fraction of the direct labor cost for operators, on the order of 50%. Management expenses are taken to be an additional 25% fraction of direct labor cost for operators.

A comparison of the components of Fixed OPEX are included in Figures 5-6. At smaller H_2 production capacities, Fixed OPEX is dominated by labor, whereas at higher production

capacities, Fixed OPEX is dominated by Maintenance. Labor expenses are taken to be a fixed contribution independent of capacity, whereas maintenance is assumed to be directly tied to the total direct CAPEX of the facility. Solids processing steps surrounding caustic soda regeneration, melting, and ash removal are predicted to be labor intensive compared to fluids handling steps, suggesting that seaweed biomass gasification may exhibit higher labor costs than fluid-centric hydrogen production methods such as conventional steam methane reforming.

Parameter	Value	Notes
Maintenance	0.06 * Total Direct CAPEX	6% of Total Direct CAPEX
Overhead	0.04 * Total Direct CAPEX	4% of Total Direct CAPEX
Taxes	0.03 * Total Direct CAPEX	3% of Total Direct CAPEX
Royalties	0.02 * Total Direct CAPEX	2% of Total Direct CAPEX
Research and Design	\$25 / ton of H_2	5% of Total OPEX, taken to be DOE Target of \$500 / ton of H_2
Labor Shifts	4	4 Labor shifts for continuous operation for 24 hours a day, 350 days per year
Solids Processing Steps	4	For estimation of number of operators
Fluids Processing Steps	6	For estimation of number of operators
Operator Salary	\$50,000 / year	Highly location dependent
Management Overhead	0.25 * Direct Labor Cost	25% of Direct Labor Cost
Labor Overhead	0.5 * Direct Labor Cost	50% of Direct Labor Cost
Operating Year	8400 Hours	Continuous Operation for 24 hours a day, 350 days per year

Table 5-7: Parameters Used to Estimate Fixed Operating Cost

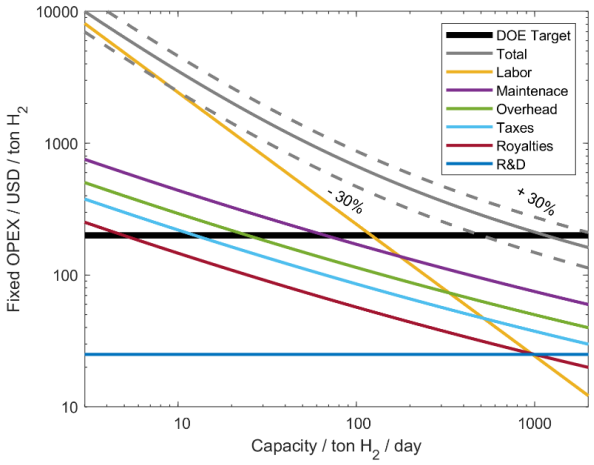

Figure 5-4: Fixed OPEX as a function of hydrogen production capacity, with Class 4 Cost Estimation error bars of +/- 30% depicted. The DOE metric of \$200 / ton of H_2 for fixed OPEX is predicted to be met at a processing scale between 500 and 2000 tons of H_2 per day.

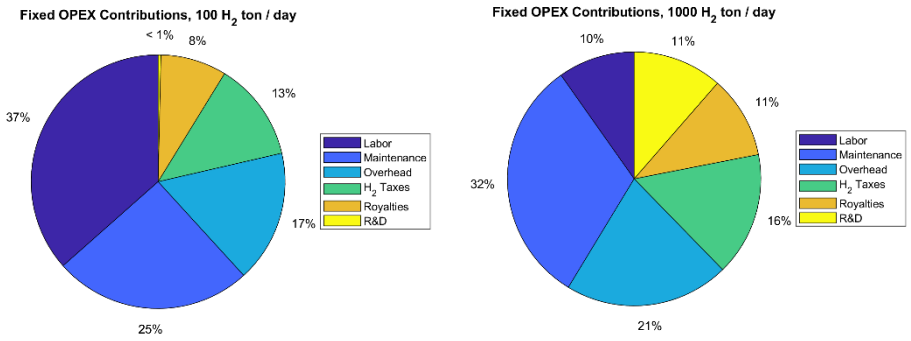

Figure 5-5: Estimated contributions to OPEX at scales of 100 and 1000 tons of H_2 per day. Labor expenses are taken to be independent of capacity, leading to a fixed OPEX contributions increasingly dominated by labor at increasingly smaller scales.

5.1.3.4 Variable Operating Cost Estimation

Calculating Feedstock Costs

The US Department of Energy has set a target feedstock price for hydrogen production via biomass gasification of $900 per tonne of hydrogen produced. Feedstock price may be broken up into two main contributions – a supplier price, and shipping cost. Other expenses, such as taxes, may be allocated between the supplier price and shipping cost. Presently, seaweed farming is predominantly conducted for foodstuff production. Therefore, the current global average seaweed price of $270 per tonne is not in itself representative of biomass growth for hydrogen production. According to the World Bank, a seaweed biomass price of $55 per ton is more consistent with biomass growth for gasification and fuel production. A seaweed price of $55 per dry ton, with a hydrogen production fraction of 0.0675 tons per ton of seaweed, equates to a feedstock price of $815 / tonne of hydrogen, less than the DOE target price of $900 per ton of hydrogen produced.

At a feedstock price of $815 per ton of hydrogen for seaweed, shipping and other expenses would need to fall below $85 per ton of hydrogen to meet the DOE target for feedstock price of $900 per ton of hydrogen. For bulk, commodity scale shipping of seaweed, transport via road, rail, and ship are considered. The cost, CO_2, SO_X, and NO_X emissions associated with commodity scale shipping via trucks (>32 ton, 16-32 ton, 7.5-16 ton, 3.5-7.5 ton), train (diesel, electric), and cargo ship are reported in Table 5-7, tabulated from the ecoinvent database.

Transportation Method	Cargo Capacity (tons)	USD / ton / km	CO_2 emissions / ton / km	NO_x emissions / ton / km	SO_x emissions / ton / km
Truck (>32 ton)	21	$0.0318	5.10E-02	7.17E-04	1.22E-05
Truck (16-32 ton)	13	$0.0370	7.69E-02	9.58E-04	1.84E-05
Truck (7.5-16 ton)	7	$0.0477	1.20E-01	7.68E-04	2.86E-05
Truck (3.5-7.5 ton)	4	$0.0588	1.18E-01	1.28E-03	2.84E-05
Rail, Diesel	flexible	$0.0406	1.20E-02	2.92E-04	3.95E-07
Rail, Electric	flexible	$0.0406	7.92E-04	1.86E-05	2.52E-08
Container Ship	43,000	$0.00074	7.84E-03	1.88E-04	1.11E-04

Table 5-8: Transportation Costs

For transportation of seaweed via truck (>32 ton), rail, and container ship, shipping cost per ton of hydrogen is tabulated as a function of distance in Figure 8. For land-based shipping, the cost of shipping is more dependent on the moisture content of the seaweed than the particular method (road versus rail). In practice, the most economical land-based method will likely be dependent on the established infrastructure in the region of the biomass gasification facility. Environmentally, rail-based shipping exhibits significantly lower emissions than road-based. Ocean-based shipping is significantly more economical than land-based methods, however is geographically limited by the existence of port infrastructure.

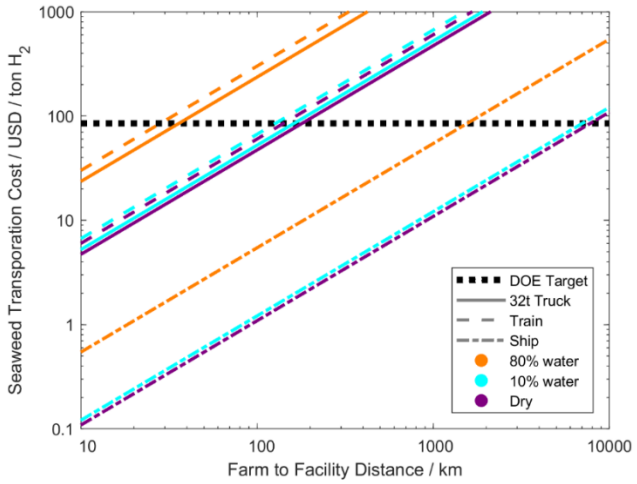

Figure 5-6: Transportation Costs

Total Variable Operating Expenditures

An overall breakdown of variable operating expenses per ton of H_2 is presented below:

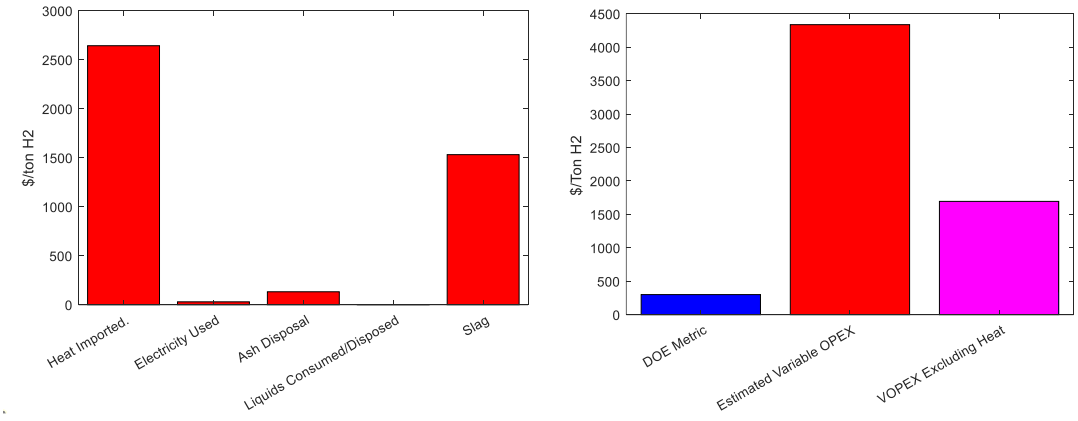

Figure 5-7: Variable expenses per ton of H2 by component and compared to the DOE cost metric for oceanic biomass

Within the assumptions outlined previously, variable operating expenses are independent of scale. Costs are dominated by heat and slag required for regeneration. Even in a case where the reactor provides all heat needed for regeneration due to co-location of another ready heat source, the DOE target is still exceeded due to slag costs. It should be noted that K_2O makes up 60% of the ash by

mass, and is a valuable commodity- depending on the purification processes required, it can be resold, so a portion of the ash disposal losses could feasibly be recuperated. This target can likely only be achieved if slag is co-located and costs are strictly due to

5.1.4 Conclusions

From the analysis conducted herein, the following conclusions can be drawn:

1. **There is potentially a viable path forward for hydrogen production via seaweed gasification using the alkaline thermal treatment process if variable operating expenses can be reduced**

Thermodynamic and technoeconomic modelling for hydrogen production via seaweed gasification using the alkaline thermal treatment process meets DOE target metrics for capital cost, fixed operating cost, and feedstock cost at economies of scale comparable to conventional hydrogen production technologies, and losses in reactor efficiency can be tolerated. Variable costs are significant due to the high energy penalty associated with cooling, dissolving, and precipitating salt – in a larger system potentially co-located with a source of slag and with heating available, this approach could be viable.

2. **Geographic location is very important**

Procurement cost of seaweed, labor costs, capital costs, and amortization practices are all highly dependent on the geographic location of the biomass gasification facility. For the shipping of seaweed to the gasification facility, ocean-based transportation exhibits markedly lower cost than land-based methods, with land-based methods becoming cost-prohibitive over distances larger than approximately 100 km. However, reliance on ocean-based shipping for seaweed delivery requires the presence of ship-port infrastructure nearby. Proximity to slag suppliers is just as important, as 1.8 times as much slag compared to seaweed is required by mass.

Meanwhile, at decreasing production capacities, labor cost becomes an increasingly large contribution to fixed operating cost. Labor cost, and the corresponding overheads associated with management and benefits, are highly geographic dependent. Similarly, variable operating costs are also geographic dependent based on local utility and feedstock procurement costs.

Capital costs also exhibit geographic dependence, with correlations available for scaling construction costs to different regions. Working capital targets are dependent on the operational and investment practices of the organization, company, or country undertaking the biomass gasification project. Similarly, amortization and depreciation practices, necessary to determine the capital cost contribution to hydrogen price, are specific to the region or organization undertaking the project, each exhibiting an array of expected rates of return and facility operation lifespans. This uncertainty, again largely geographic, motivates our decision to not calculate an effective hydrogen price from seaweed biomass gasification for comparison to DOE metrics.

3. **Solids processing costs are significant, especially at reduced operating scales**

Reviewing the relative contributions to capital and fixed operating costs, these metrics are predicted to be dominated by solids handling steps (ash removal and NaOH regeneration) and labor respectively, especially at smaller operating scales (< ~100 tons of H_2 per day). The capital burden of solids handling for seaweed gasification may be limited by optimization of reagent usage, ash removal methods of NaOH recycling. Likely, this balance lies in a minimization of hydrogen production cost across an integrated capital and operating cost framework.

Meanwhile, labor expenses associated with solids handling are classically higher than fluids handling. However, new methods of labor allocation, as well as increasing levels of process

automation, may lead to a closing of the labor intensity gap between solids and fluids handling. Overall, minimizing the number and intensity of solids processing operations is a path forward to further improve the economic prospects of hydrogen production from seaweed gasification via alkaline thermal treatment.

4. **Molten salt gasification is not cost prohibitive compared to conventional hydrogen production**

Breakdown of the contributions to capital cost of individual processing operations, gasification of biomass using molten salts is not an economic bottleneck in the process, and is capitally comparative to conventional water gas shift processing steps. From an operation standpoint, the gasification reaction is highly exothermic, allowing the gasification reactor to be run auto-thermally, thereby limiting operating expenses associated with elevated temperature reaction.

5. **Waste heat recovery via steam generation is predicted to provide limited economic benefit compared to direct thermal recuperation for process heating**

Turbines for power generation are observed to be significantly more expensive than heat exchangers for direct process heat recovery. For processes where solids are handled at elevated temperatures, using waste process heat to preheat feed streams is economically favorable to steam production for electricity generation.

5.2 Technoeconomic Analysis of Electrochemically Regenerated Alkaline Thermal Treatment

5.2.1 Analysis Framework

Here, we alter the process presented above to utilize electrochemical regeneration. The previous and new process alternatives are illustrated in Figure 5-8 A and B.

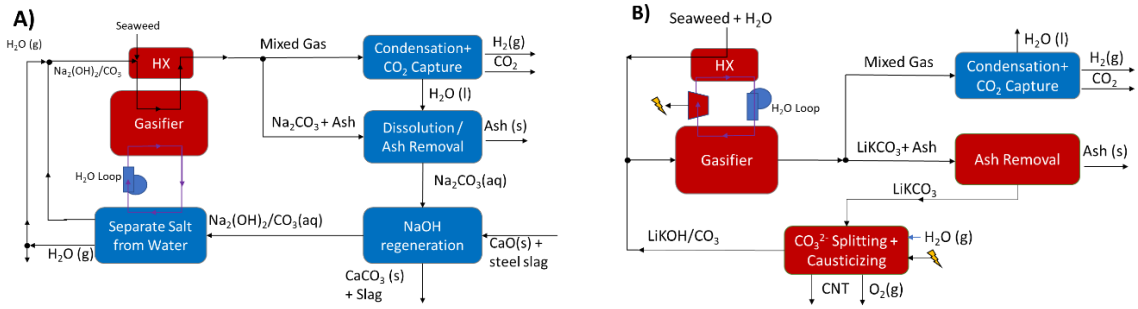

Figure 5-8: Alkaline Thermal Treatment Process Alternatives for comparison: A) slag regenerated B) electrochemically regenerated

In summary, rather than relying on an ambient temperature metathesis reaction with calcium hydroxide, regeneration is performed by electrochemically converting carbonates into carbon and oxygen. While hydrogen will be co-produced, at high overpotentials and low concentrations of Li_2CO_3, carbon deposition dominates the process.

While the DOE framework no longer applies, we can employ a similar methodology to examine differences between fixed and variable operating costs and capital costs between the two system configurations. While the overall fixed operating expenses will change, we assume the same labor requirements and scaling laws as a function of capital investment. Variable operating expenses

and capital expenses will be altered significantly, no longer including slag costs, but now accounting for revenue from CNT production and electrical requirements of electrowinning. Variable operating expenses

5.2.2 Thermodynamic Analysis of Electrochemically Mediated Alkaline Thermal Treatment

5.2.2.1 Overview and Assumptions

We conduct thermodynamic analysis using the same FactSage database, maintaining all assumptions made earlier. While data for eutectic K/Li carbonate/hydroxide salts is not readily available, Factsage offers estimated enthalpies of formation for Li_2CO_3 and Li_2O below their respective melting points as pure compounds. We utilize the assumptions outlined in 5.1.2.1 for input preheating and heat recovery, gasification, and gas separation. Assumptions for the electrolysis process are given as follows:

Electrolyzer Assumptions

1. We assume the following electrochemical reactions take place in the cell:
   a. $\left.\begin{matrix} Li_2CO_3 + 4e^- \rightarrow 2Li_2O + C + 2O^{2-} \\ 2O^{2-} \rightarrow 4e^- + O_2 \end{matrix}\right\} Li_2CO_3 \rightarrow 2Li_2O + C + O_2$
   b. $\left.\begin{matrix} 4LiOH + 4e^- \rightarrow 2Li_2O + 2H_2 + 2O^{2-} \\ 2O^{2-} \rightarrow 4e^- + O_2 \end{matrix}\right\} 4LiOH \rightarrow 2Li_2O + 2H_2 + O_2$

   As well as the following steam uptake reaction:
   c. $H_2O + Li_2O \rightarrow 2LiOH$
2. On a carbon deposition basis, we assume a Coulombic efficiency of 80%; that is, for each mole of electrons passed through the cell, 0.2 moles of carbon, 0.1 moles of hydrogen, and 0.25 moles of oxygen will be recovered.
3. The thermoneutral potential of carbon deposition/O_2 evolution reaction is assumed to be 1.575 at 500C.96 Electrolysis is conducted at an 0.5V overpotential (2.075V total), based on heat transfer models carried out to determine the conditions for an autothermal electrolyzer97 as well as experimental observations on potentials required for the desired 100mA/cm^2 operating current density detailed earlier in this work.
4. We assume the cell is autothermal, and that no meaningful amount of heat can be recovered from the causticizing reaction. Steam is preheated to 400°C before sparging.

5.2.2.2 Thermodynamic Analysis: Results

Energy and Mass Balances

Reactor:

Molar inputs and outputs for the ATT reactor are tabulated below:

Species	In (mol/kg SW)	Out (mol/kg SW)
H_2O	31.83	15.92
$C_6H_{10}O_5$	3.979	0
Ash (K_2O)	2.704	2.704
Li_2CO_3	135.3	147.23
LiOH	23.88	0
H_2	0	47.75
CO_2	0	11.93

Table 5-9: Reactor molar balances in model of baseline ATT proces

Steam Loop

The reactor rejects 19.2 MJ/kg seaweed to the steam loop, or enough to heat 316 mol/kg SW of steam from 25°C to 500°C at 10 bar. Of this quantity, 57.4 mol steam /kg SW are sent to boil the water used in causticizing and the ATT reactor. The remaining 259 mol steam/kg SW are directed to the turbine, producing 5 MJ / kg SW.

Electrochemical LiOH Regeneration

Species	Inflow (mol/kg SW)	Outflow (mol/kg SW)
H_2O	11.9	0
Li_2CO_3	147.2	135.3
LiOH	0	23.87
C	0	11.93
H_2	0	5.97
O_2	0	17.9

Table 5-10: LiOH Regeneration step mole balances

Gas Separation

After the steam is allowed to condense off with SOx species, the minimum work of separation for the remaining H_2 and CO_2 is given by the change in gibbs free energy:

$$W_{Min} = G_{H2,Out} + G_{CO2,Out} - G_{Mix,In} \quad \text{Eq. 5-13}$$

The minimum work evaluates to 263 kJ/kg SW. With a 20% second law efficiency, this is realized as a system electricity penalty of 132 kJ/kg SW.

Solids Handling

The industrial handbook estimates power requirements of solids handling at 12.5 kWh/ton. Therefore, the ash requires 11.5 kJ/kg SW of electricity

Electricity Considerations

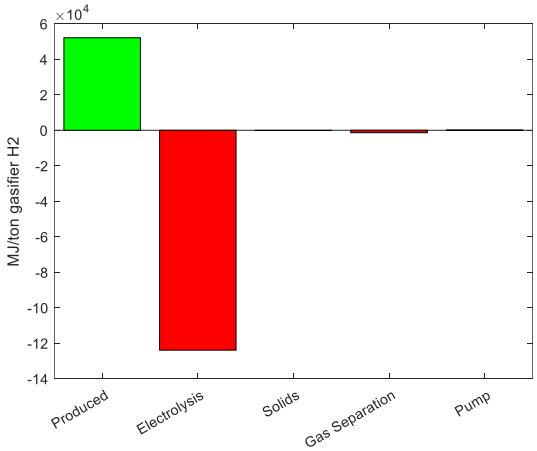

Figure 5-9: Electricity production and consumption normalized per metric ton of hydrogen produced in the gasifier

Electricity sources and sinks throughout the system are given in Figure 5-9. Electrolysis requirements outweigh all other electricity demands in the system, but because gasifier heat is no longer required to separating hydroxides from water, a significant portion of the electricity demands (42%) can be offset within the system.

5.2.3 Economic Assessment for Electrochemically Mediated Alkaline Thermal Treatment of Oceanic Biomass

5.2.3.1 Economic Analysis Methodology

In order to estimate the capital costs, we employ the same methodology as above for the reactor associated with electrochemical regeneration, with the notable change of replacing causticizing and NaOH regeneration unit operations with a single electrolyzer. To estimate the cost of such a plant, we adopt the methodology proposed by Stinn and Allanore98 for generalized electrowinning processes at high temperatures. We model the total capital investment (C) as a sum of the front-end processing (F) electrolysis and product handling (E) and rectifier (R):

$$C = F + E + R \qquad \text{Eq. 5-14}$$

We assume front-end costs are included in the unit operations already considered for alkaline thermal treatment, so the expressions

Capital costs of electrolysis and metal recovery (E) are dependent on the number of electrolyzers required, which can be determined as a function of production rate (p, kg/s) product molar mass (M, kg/,mol), current density (j, A/m^2), molar ratio of electrons to product (z), current efficiency (ε) and cathode area per cell (A). α_2 is a fitting parameter dependent on temperature (T, °C). F represents the Faraday constant (96485 C/mol electrons)

$$E = \alpha_2(T)\left(\frac{pzF}{jA\varepsilon M}\right)^{x_2} \qquad \text{Eq. 5-15}$$

To estimate the cost of a rectifier, Stinn et al. followed the model established by Hine et al[99]. The capital cost is considered as a function of installed power capacity (Q, MW), cell operating voltage (V, V), and number of operating lines (N). The fitting parameters x_3 and x_4 are assumed to be 0.15 and 0.5 respectively, and α_3 is a proportionality constant.

$$R = \alpha_3(T) Q V^{x_3} N^{x_4} \qquad \text{Eq. 5-16}$$

Substituting statistical best fit parameters for each α and using process-specific values of the overall capital cost can then be expressed as:

$$C = \alpha_2(T)\left(\frac{pzF}{jA\varepsilon M}\right)^{x_2} + \alpha_3(T) Q V^{x_3} N^{x_4}$$

$$= \frac{5634000}{1+e^{-7.813\times10^{-3}\times(T-349)}}\left(\frac{pzF}{jA\varepsilon M}\right)^{0.9} + 750000 Q V^{0.15} N^{0.5} \qquad \text{Eq. 5-17}$$

This expression can ultimately be converted to a function of only throughput for comparison to other cost curves shown before; an additional assumption must be made regarding the area per

electrolytic cell, so $50m^2$ is selected as the median of the metals used to inform the original statistical model.

5.2.3.2 Capital Expense

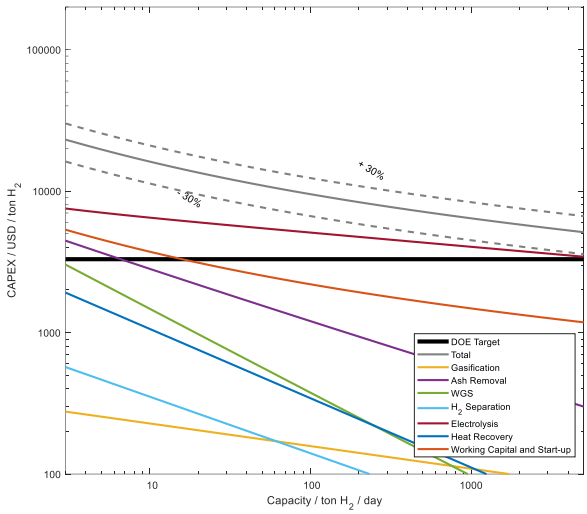

Figure 5-10: Capital Costs for the electrochemically mediated ATT process as a function of gasifier H2 output

The estimated cost of constructing the electrolyzer and rectifier dramatically outweighs anything else in the system: this component alone exceeds the DOE target. It should be noted that the DOE target does not include additional revenue streams provided by the electrolyzer hydrogen, oxygen, and carbon nanotubes – it is only provided as a standard of comparison for the baseline slag regenerated model. Because the electrolyzer cost scales linearly as the number of cells installed, economy of scale only exacerbates this cost share imbalance, illustrated in Figure 5-11**.**

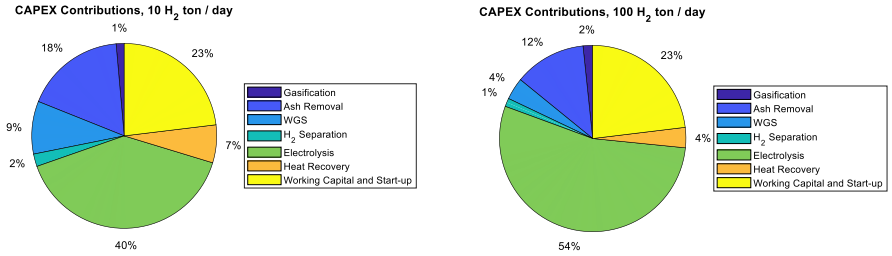

Figure 5-11: Relative CAPEX contributions at 10 tons H_2 per day and 100 tons H_2 per day

Due to the reduced hydroxide content in the gasifier salt, a larger reactor is also required, but this is still outweighed by the electrolyzer costs.

5.2.3.3 Variable Operating Expense

For the following analysis, we assume an electricity cost of $0.07/kWh.

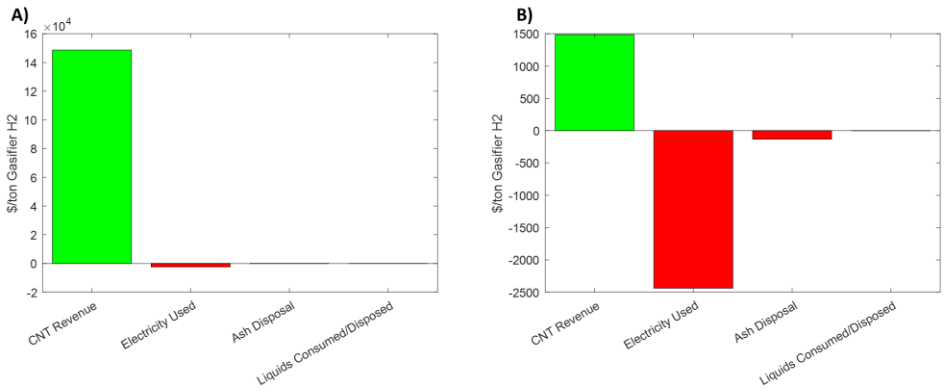

Figure 5-12: Variable operating expenses and CNT revenue with CNT values of A) $100k/ton, B) $1k/ton

In Figure 5-12, we present the variable operating expense estimates compared to revenue obtained from the new CNT product. A CNT value of $100k/ton ($100/kg) represents the current market value for comparable CVD-derived multiwalled carbon nanotube wools, whereas a lower bound of $1k/ton represents amorphous carbon black. It should be noted that costs associated with replacing cathodes and lithium loss to the environment are omitted and likely to be significant, but still much less than the revenue provided by the current market value of CNTs.

For comparison with the slag case, we present net variable operating expenses compared to the DOE metric for variable operating expenses in production of hydrogen from oceanic biomass.

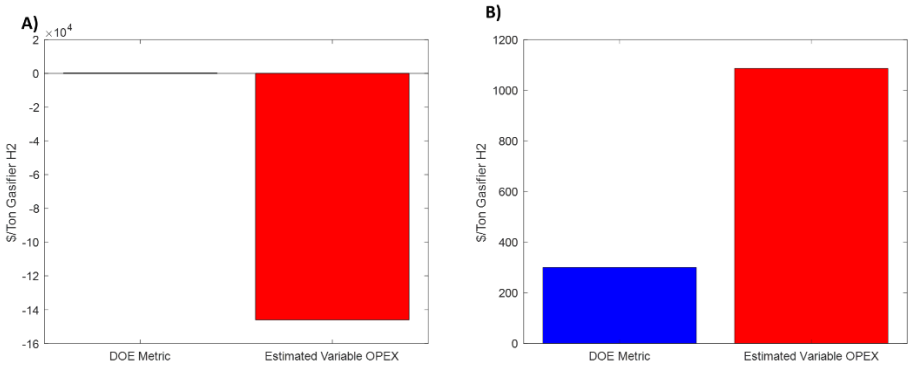

Figure 5-13: Net operating expenses compared to the DOE metric for H_2 production from oceanic biomass for CNT values of A) $100k/ton B) $1k/ton

From Figure 5-13, we observe that the value of carbon nanotubes dramatically outweighs any other variable operating expense at a current market value of $100k/ton, resulting in a highly negative operating expenditure. At a lower bound of $1000/ton representing the current cost of amorphous carbon, carbon no longer subsidizes the electricity costs, and the DOE metric is not met. It should be noted that the latter case closely resembles that of electrolytic production of amorphous carbon, motivating the use of a lithium-rich eutectic molten salt rather than an inexpensive sodium-potassium eutectic.

5.2.3.4 Fixed Operating Expense

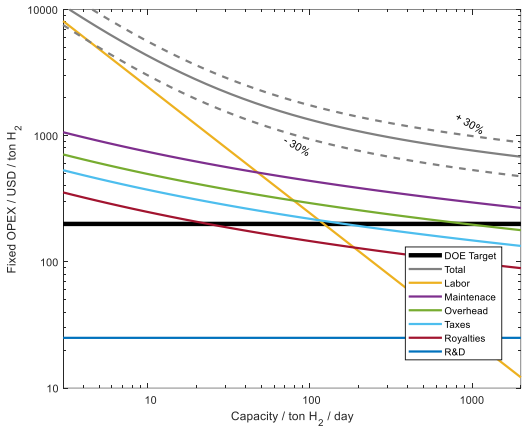

Figure 5-14: Estimated fixed operating expenses for the electrochemically mediated ATT process as a function of gasifier H_2 output

Fixed operating expenses scale primarily based on capital expenditure estimates, so they are also anticipated to increase significantly with the addition of an electrolyzer. Cost distributions do not change appreciably compared to those calculated in the slag case.

5.2.4 Conclusions

This study contained several major limitations. The electrolytic operating conditions including coulombic efficiency have not been verified in the presence of steam. However, we can make several general conclusions:

1. **Economics of electrolysis dominate the system in the electrochemical regeneration case**
   At a current value of $100/kg, carbon nanotubes are much more valuable than hydrogen – however, the electrolyzer and rectifier dominate capital expenses. It is therefore better to contextualize this process as carbon nanotube electrolysis with an added benefit of reduced cost hydrogen and offset electricity requirements. It is still unclear if the added benefits from using the calcined salt for ATT outweigh additional electricity requirements associated with hydrogen side reactions, necessitating further study.
2. **System thermodynamics are improved dramatically by electrochemical regeneration**
   Energy costs in the electrochemically mediated system are approximately half of those in the slag-regenerated case, with a significant additional revenue stream. The slag-regenerated case likely represents an overestimate of energy consumed (we assume full boiling rather than a humidification-dehumidification approach, and ignore potential synergy providing steam to other processes), and the electrochemically mediated case is potentially an underestimate (see conclusion 4), but comparable values suggest that there is potential merit to an electrochemically mediated approach due to the high value of CNTs.
3. **Lithium is necessary in the salt for economic operation, but losses with the removed solids must be minimized**
   The results in Figure 5-13 indicate that amorphous carbon that can be derived from inexpensive $NaKCO_3$ is insufficient to offset the additional economic penalties incurred by the cost of electricity and construction of an electrolysis unit. To achieve economic viability, lithium must be included in the salt to obtain high value multiwalled carbon

nanotubes. Special attention must be paid to ensuring the electrolyte can be effectively recovered when removing ash and carbonaceous products from the system.

4. **Further experimental study is needed to limit uncertainty and prove feasibility of the concept**

   Examples of high current density electrolysis of eutectic carbonates under steam were not observed in literature, and extrapolation from experiments under CO_2 to obtain a coulombic efficiency introduce questions about uptake and conversion. Operating expenses are highly sensitive to the current density, coulombic efficiency, and required overpotential for operation, so these assumptions were significant and merit further study.

6 Future Work and Opportunities

6.1 Corrosion Prevention for Long-Term Containment of Molten Alkali Borates

The thermogravimetric studies conducted suggest that zirconia or yttria stabilized zirconia (YSZ) could offer possible alternatives to nickel as a compatible construction material for alkali borate systems. This would be attractive in applications such as ceramic packing materials for absorber/desorber columns or electrically insulating containment for electrochemical applications.

Material costs and the brittle nature of zirconia ceramics likely make constructing pipes and machinery from YSZ unattractive, but it could be investigated for use in the form of thermal barrier coatings[100]. These coatings are most commonly used to increase the working temperature range of turbine blades, but they have been also investigated for use in protecting Inconel from vanadia and sulfate molten salts, and could potentially be applied to protect alloys from borates.[101,102] If successful, such coatings could enable construction from less expensive high temperature alloys like Inconel.

Another potentially viable solution would be thin protective platinum coatings - if sufficiently thin (on the order of single microns), platinum coatings on base alloys like 316 stainless steel or Inconel could have greater cost-effectiveness and longevity compared to building infrastructure from nickel 200/201. Several questions would need to be addressed with this approach regarding the method of deposition and whether such coatings would be mechanically and chemically robust to thermal expansion and erosion by flowing salt.

In the work of Halliday et. al., it was suggested that cathodic protection could be used to slow oxidation and corrosion of nickel.[33] The reversible nickel oxidation/reduction peaks in the cyclic voltammetry profiles obtained between a nickel cathode and a nickel crucible suggest that this is within the realm of possibility. If a constant voltage maintaining 0 current is applied between an inert platinum anode and nickel, this could potentially slow oxidation and dissolution of nickel ions, extending the life of the plant. Further experimental study is needed to determine the effectiveness of this method.

6.2 Borates as an Electrochemically Mediated CO_2 Sorbent

This thesis presented a comparative study on the conversion effectiveness of CO_2 into CNTs using borate/carbonate blends as an electrochemical medium. Using a galvanized steel cathode, a 1:3 B:C starting ratio was found to be optimal for increasing the CO_2 uptake capacity without sacrificing Coulombic efficiency. It was also found that more stable working materials like nickel and 316 stainless steel could also be used to electrodeposit carbon nanotubes in this fashion.

The work presented in this thesis is heavily focused on the thermodynamics of CNT production and not transport considerations or gas evolution. Future work with a larger, upgraded setup could pay closer attention to uptake kinetics by sparging CO_2 directly into the melt rather than purging the headspace, and examination of the effects of materials selection and carbonate/borate ratios on the evolution of CO would provide valuable insights.

The relatively small window of electrochemical stability of alkali borates remains a challenge for practical application. This concern is expressed in other studies on the effects of borates in CO_2 electrolysis,[61,62] as it is difficult to achieve CNTs without co-deposition of other boron species.

6.3 Investigating Electrochemical Regeneration for Alkaline Thermal Treatment

The experiments conducted indicate that in-situ electrochemical regeneration cannot be used in conjunction with alkaline thermal treatment for conversion of plastics and oceanic biomass into hydrogen and carbon nanotubes. However, if the seaweed ash is removed, there remains potential for a multi-step process. A significant limitation is the potential for lithium loss in the ash and plastic char removed – it is unclear how to perform this separation process at scale, and this could

Preliminary economic analysis suggests that alkaline thermal treatment as a standalone process can meet the department of energy technical targets for production of hydrogen from biomass under certain circumstances, but these cases are limited. Electrochemical regeneration in a steam-purged electrolyzer could dramatically reduce energy requirements and provide an additional CNT revenue stream, at the expense of dramatically increased capital expenses and a more expensive lithium working salt. The analysis conducted herein is cursory and only intended to observe broad trends - a more in-depth analysis would be helpful in making conclusive statements guiding future research. Several practical considerations must be addressed regarding ash removal and the practicality of a steam-purged electrolyzer configuration; if the latter is deemed infeasible, additional study on the feasibility of a solid to liquid oxide process would be invaluable.

Bibliography

1. Horowitz, C. A. Paris Agreement. *International Legal Materials* **55**, (2016).
2. IEA. *Global Energy Review 2019*. (2020).
3. IPCC. *AR5 Climate Change 2014: Mitigation of Climate Change*. (2014).
4. Jia, Z. & Lin, B. How to achieve the first step of the carbon-neutrality 2060 target in China: The coal substitution perspective. *Energy* **233**, (2021).
5. Schreyer, F. *et al.* Common but differentiated leadership: strategies and challenges for carbon neutrality by 2050 across industrialized economies. *Environmental Research Letters* **15**, (2020).
6. Feldman, D. *et al. U.S. Solar Photovoltaic System and Energy Storage Cost Benchmark: Q1 2020*. (2021).
7. Bui, M. *et al.* Carbon capture and storage (CCS): the way forward. *Energy & Environmental Science* **11**, (2018).
8. IEA. *Transforming Industry through CCUS*. (2019).
9. Hu, J., Galvita, V., Poelman, H. & Marin, G. Advanced Chemical Looping Materials for CO2 Utilization: A Review. *Materials* **11**, (2018).
10. Scheffknecht, G., Al-Makhadmeh, L., Schnell, U. & Maier, J. Oxy-fuel coal combustion—A review of the current state-of-the-art. *International Journal of Greenhouse Gas Control* **5**, (2011).
11. Allam, R. *et al.* Demonstration of the Allam Cycle: An Update on the Development Status of a High Efficiency Supercritical Carbon Dioxide Power Process Employing Full Carbon Capture. *Energy Procedia* **114**, (2017).
12. Allam, R. J., Fetvedt, J. E., Forrest, B. A. & Freed, D. A. The Oxy-Fuel, Supercritical CO2 Allam Cycle: New Cycle Developments to Produce Even Lower-Cost Electricity From Fossil Fuels Without Atmospheric Emissions. in *Volume 3B: Oil and Gas Applications; Organic Rankine Cycle Power Systems; Supercritical CO2 Power Cycles; Wind Energy* (American Society of Mechanical Engineers, 2014). doi:10.1115/GT2014-26952.
13. Sanders, D. F. *et al.* Energy-efficient polymeric gas separation membranes for a sustainable future: A review. *Polymer* **54**, (2013).
14. Zhang, Y., Sunarso, J., Liu, S. & Wang, R. Current status and development of membranes for CO2/CH4 separation: A review. *International Journal of Greenhouse Gas Control* **12**, (2013).

15. Song, C., Liu, Q., Deng, S., Li, H. & Kitamura, Y. Cryogenic-based CO2 capture technologies: State-of-the-art developments and current challenges. *Renewable and Sustainable Energy Reviews* **101**, (2019).

16. Dutcher, B., Fan, M. & Russell, A. G. Amine-Based CO_2 Capture Technology Development from the Beginning of 2013—A Review. *ACS Applied Materials & Interfaces* **7**, (2015).

17. SIRCAR, S. & GOLDEN, T. C. Purification of Hydrogen by Pressure Swing Adsorption. *Separation Science and Technology* **35**, (2000).

18. Kang, J. S., Kim, S. & Hatton, T. A. Redox-responsive sorbents and mediators for electrochemically based CO2 capture. *Current Opinion in Green and Sustainable Chemistry* **31**, (2021).

19. Yin, H. *et al.* Capture and electrochemical conversion of CO2 to value-added carbon and oxygen by molten salt electrolysis. *Energy & Environmental Science* **6**, (2013).

20. Ball, R. Using the second law first: Improving the thermodynamic efficiency of carbon dioxide separation from gas streams in an Endex calcium looping system. *Applied Thermal Engineering* **74**, (2015).

21. Blamey, J., Anthony, E. J., Wang, J. & Fennell, P. S. The calcium looping cycle for large-scale CO2 capture. *Progress in Energy and Combustion Science* **36**, (2010).

22. Hanak, D. P., Anthony, E. J. & Manovic, V. A review of developments in pilot-plant testing and modelling of calcium looping process for CO_2 capture from power generation systems. *Energy & Environmental Science* **8**, (2015).

23. Perejón, A. *et al.* The Calcium-Looping technology for CO2 capture: On the important roles of energy integration and sorbent behavior. *Applied Energy* **162**, (2016).

24. Huang, L. *et al.* Alkali Carbonate Molten Salt Coated Calcium Oxide with Highly Improved Carbon Dioxide Capture Capacity. *Energy Technology* **5**, (2017).

25. Naeem, M. A. *et al.* Optimization of the structural characteristics of CaO and its effective stabilization yield high-capacity CO2 sorbents. *Nature Communications* **9**, (2018).

26. Florin, N. H. & Harris, A. T. Reactivity of CaO derived from nano-sized CaCO3 particles through multiple CO2 capture-and-release cycles. *Chemical Engineering Science* **64**, (2009).

27. Kanai, Y., Terasaka, K., Fujioka, S. & Fukunaga, K. Absorption of Carbon Dioxide at High Temperature with Molten Alkali Carbonate Using Bubble Column Reactor. *JOURNAL OF CHEMICAL ENGINEERING OF JAPAN* **52**, (2019).

28. Halliday, C., Harada, T. & Hatton, T. A. Toward a Mechanistic Understanding and Optimization of Molten Alkali Metal Borates ($A_xB_{1-x}O_{1.5-x}$) for High-Temperature CO_2 Capture. *Chemistry of Materials* **32**, (2020).

29. Halliday, C. & Hatton, T. A. Net-Negative Emissions through Molten Sorbents and Bioenergy with Carbon Capture and Storage. *Industrial & Engineering Chemistry Research* **59**, (2020).

30. Halliday, C. & Hatton, T. A. The potential of molten metal oxide sorbents for carbon capture at high temperature: Conceptual design. *Applied Energy* **280**, (2020).

31. Halliday, C., Harada, T. & Hatton, T. A. Acid Gas Capture at High Temperatures Using Molten Alkali Metal Borates. *Environmental Science & Technology* **54**, (2020).

32. Halliday, C., Harada, T. & Hatton, T. A. Bench-Scale Demonstration of Molten Alkali Metal Borates for High-Temperature CO_2 Capture. *Industrial & Engineering Chemistry Research* **59**, (2020).

33. Halliday, C., Ozbek, N. & Hatton, T. A. Understanding Material Compatibility in CO_2 Capture Systems Using Molten Alkali Metal Borates. *ACS Applied Materials & Interfaces* **12**, (2020).

34. Wilberforce, T., Baroutaji, A., Soudan, B., Al-Alami, A. H. & Olabi, A. G. Outlook of carbon capture technology and challenges. *Science of The Total Environment* **657**, (2019).

35. Voormeji, D. A. & Simandl, G. J. Geological, Ocean, and Mineral CO2 Sequestration Options: A Technical Review. *Geoscience Canada* **31**, (2004).

36. Alvarado, V. & Manrique, E. Enhanced Oil Recovery: An Update Review. *Energies* **3**, (2010).

37. Gale, J. Overview of CO2 emission sources, potential, transport and geographical distribution of storage possibilities . in *IPCC workshop on carbon dioxide capture and storage* 15–29 (ECN, 2002).

38. IEA. *Putting CO2 to Use*. (2019).

39. Jarvis, S. M. & Samsatli, S. Technologies and infrastructures underpinning future CO 2 value chains: A comprehensive review and comparative analysis. *Renewable and Sustainable Energy Reviews* **85**, (2018).

40. Koytsoumpa, E. I., Bergins, C. & Kakaras, E. The CO 2 economy: Review of CO 2 capture and reuse technologies. *The Journal of Supercritical Fluids* **132**, (2018).

41. Saravanan, A. *et al.* A comprehensive review on different approaches for CO2 utilization and conversion pathways. *Chemical Engineering Science* **236**, (2021).

42. Weng, W., Tang, L. & Xiao, W. Capture and electro-splitting of CO2 in molten salts. *Journal of Energy Chemistry* **28**, (2019).

43. Ren, J. *et al.* Recent Advances in Solar Thermal Electrochemical Process (STEP) for Carbon Neutral Products and High Value Nanocarbons. *Accounts of Chemical Research* **52**, (2019).

44. Licht, S. *et al.* A New Solar Carbon Capture Process: Solar Thermal Electrochemical Photo (STEP) Carbon Capture. *The Journal of Physical Chemistry Letters* **1**, (2010).

45. Liu, X., Wang, X., Licht, G. & Licht, S. Transformation of the greenhouse gas carbon dioxide to graphene. *Journal of CO2 Utilization* **36**, (2020).

46. Liu, X., Ren, J., Licht, G., Wang, X. & Licht, S. Carbon Nano-Onions Made Directly from CO_2 by Molten Electrolysis for Greenhouse Gas Mitigation. *Advanced Sustainable Systems* **3**, (2019).

47. Johnson, M. *et al.* Carbon nanotube wools made directly from CO2 by molten electrolysis: Value driven pathways to carbon dioxide greenhouse gas mitigation. *Materials Today Energy* **5**, (2017).

48. Wang, X., Liu, X., Licht, G. & Licht, S. Calcium metaborate induced thin walled carbon nanotube syntheses from CO2 by molten carbonate electrolysis. *Scientific Reports* **10**, (2020).

49. Ren, J., Li, F.-F., Lau, J., González-Urbina, L. & Licht, S. One-Pot Synthesis of Carbon Nanofibers from CO_2. *Nano Letters* **15**, (2015).

50. Moyer, K., Zohair, M., Eaves-Rathert, J., Douglas, A. & Pint, C. L. Oxygen evolution activity limits the nucleation and catalytic growth of carbon nanotubes from carbon dioxide electrolysis via molten carbonates. *Carbon* **165**, (2020).

51. SASAKI, K., KUNAI, A. & SADA, T. Production of Carbon Monoxide by Means of Molten Salt Electrolysis. *Denki Kagaku oyobi Kogyo Butsuri Kagaku* **48**, (1980).

52. Johnson, M. *et al.* Carbon nanotube wools made directly from CO2 by molten electrolysis: Value driven pathways to carbon dioxide greenhouse gas mitigation. *Materials Today Energy* **5**, (2017).

53. Kumar, M. & Ando, Y. Chemical Vapor Deposition of Carbon Nanotubes: A Review on Growth Mechanism and Mass Production. *Journal of Nanoscience and Nanotechnology* **10**, (2010).

54. Arora, N. & Sharma, N. N. Arc discharge synthesis of carbon nanotubes: Comprehensive review. *Diamond and Related Materials* **50**, (2014).

55. Kim, H. C. & Fthenakis, V. Life Cycle Energy and Climate Change Implications of Nanotechnologies. *Journal of Industrial Ecology* **17**, (2013).

56. Endo, M., Strano, M. S. & Ajayan, P. M. Potential Applications of Carbon Nanotubes. in *Carbon Nanotubes: Advanced Topics in the Synthesis, Structure, Properties and Applications* (eds. Dresselhaus, G. & Dresselhaus, M. S.) 13–62 (Springer Berlin Heidelberg, 2008).

57. Prieto, C., Fereres, S., Ruiz-Cabañas, F. J., Rodriguez-Sanchez, A. & Montero, C. Carbonate molten salt solar thermal pilot facility: Plant design, commissioning and operation up to 700 °C. *Renewable Energy* **151**, (2020).

58. Licht, S. *et al.* Amplified CO2 reduction of greenhouse gas emissions with C2CNT carbon nanotube composites. *Materials Today Sustainability* **6**, (2019).

59. Licht, S. Co-production of cement and carbon nanotubes with a carbon negative footprint. *Journal of CO2 Utilization* **18**, (2017).

60. Licht, S. & Wu, H. STEP Iron, a Chemistry of Iron Formation without CO2 Emission: Molten Carbonate Solubility and Electrochemistry of Iron Ore Impurities. *The Journal of Physical Chemistry C* **115**, (2011).

61. Hu, L. *et al.* Tunable Selectivity and High Efficiency of CO2 Electroreduction via Borate-Enhanced Molten Salt Electrolysis. *iScience* **23**, (2020).

62. Hu, L., Deng, B., Yang, Z. & Wang, D. Buffering electrolyte alkalinity for highly selective and energy-efficient transformation of CO2 to CO. *Electrochemistry Communications* **121**, (2020).

63. Harada, T., Halliday, C., Jamal, A. & Hatton, T. A. Molten ionic oxides for CO_2 capture at medium to high temperatures. *Journal of Materials Chemistry A* **7**, (2019).

64. Zhang, K., Kim, W.-J. & Park, A.-H. A. Alkaline thermal treatment of seaweed for high-purity hydrogen production with carbon capture and storage potential. *Nature Communications* **11**, (2020).

65. Zhang, K., Kim, W.-J. & Park, A.-H. A. Alkaline thermal treatment of seaweed for high-purity hydrogen production with carbon capture and storage potential. *Nature Communications* **11**, 3783 (2020).

66. Bouzouita, K. & Desmaison, J. Oxidation mechanism of tantalum in carbon dioxide. *Journal of Alloys and Compounds* **336**, (2002).

67. Yukin, G. I. The mechanism of electroplating with boron. *Metal Science and Heat Treatment* **13**, (1971).

68. Harada, T. & Hatton, T. A. Tri-lithium borate (Li_3BO_3); a new highly regenerable high capacity CO_2 adsorbent at intermediate temperature. *J. Mater. Chem. A* **5**, (2017).

69. Wartena, R., Winnick, J. & Pfromm, P. H. Recycling wood pulping chemicals by molten salt electrolysis: cyclic voltammetry of mixtures containing Na2CO3 and Na2SO4. *Journal of Applied Electrochemistry* **32**, (2002).

70. Izaki, Y., Mugikura, Y., Watanabe, T., Kawase, M. & Selman, J. R. Direct observation of the oxidation nickel in molten carbonate. *Journal of Power Sources* **75**, (1998).

71. Ingram, M. D. & Janz, G. J. The thermodynamics of corrosion in molten carbonates: Application of E/pCO2 diagrams. *Electrochimica Acta* **10**, (1965).

72. Yazici, M. S. & Selman, J. R. Dissolution of partially immersed nickel during in situ oxidation in molten carbonate: cyclic, stripping and square wave voltammetry measurements. *Journal of Electroanalytical Chemistry* **457**, (1998).

73. Qingfeng, L., Borup, F., Petrushina, I. & Bjerrum, N. J. Complex Formation during Dissolution of Metal Oxides in Molten Alkali Carbonates. *Journal of The Electrochemical Society* **146**, (1999).

74. Vossen, J. P. T., Plomp, L. & de Wit, J. H. W. Corrosion of Nickel in Molten Carbonate. *Journal of The Electrochemical Society* **141**, (1994).

75. Ijije, H. v. *et al.* Electro-deposition and re-oxidation of carbon in carbonate-containing molten salts. *Faraday Discuss.* **172**, (2014).

76. Smith R J, B., Loganathan, M. & Shantha, M. S. A Review of the Water Gas Shift Reaction Kinetics. *International Journal of Chemical Reactor Engineering* **8**, (2010).

77. Sanchez, D. R. Recausticizing - Principles and Practice. in *Curso de Recuperação de Produtos Químicos* (Tappi, 2002).

78. Tran, H. & Vakkilainen, E. K. *The Craft Chemical Recovery Process*. (2016).

79. Ji, D. *et al.* The optimization of electrolyte composition for CH4 and H2 generation via CO2/H2O co-electrolysis in eutectic molten salts. *International Journal of Hydrogen Energy* **44**, (2019).

80. Ji, D. *et al.* The optimization of electrolyte composition for CH4 and H2 generation via CO2/H2O co-electrolysis in eutectic molten salts. *International Journal of Hydrogen Energy* **44**, (2019).

81. Bale, C. W. & Pelton, A. D. Coupled phase diagram and thermodynamic analysis of the 18 binary systems formed among Li2Co3, K2Co3,Na2Co3, Lioh, Koh, Naoh, Li2So4, K2So4 and Na2So4. *Calphad* **6**, (1982).

82. Ji, D. *et al.* A comparative study of electrodes in the direct synthesis of CH4 from CO2 and H2O in molten salts. *International Journal of Hydrogen Energy* **42**, (2017).

83. Vossen, J. P. T., Plomp, L. & de Wit, J. H. W. Corrosion of Nickel in Molten Carbonate. *Journal of The Electrochemical Society* **141**, (1994).

84. US-DOE. DOE Technical Targets for Hydrogen Production from Biomass Gasification. *Fuel Cell Technology Office Multi-year Research, Development, and Demonstration Plan* (2020).

85. US-DOE. DOE Technical Targets for Hydrogen Production from Biomass Gasification. *Fuel Cell Technology Office Multi-year Research, Development, and Demonstration Plan* (2020).

86. Graedel, T. E. On the concept of industrial ecology. *Abstracts of the Pacific Basin Nuclear Conference* 193 (2004).

87. ISO. *ISO 14044*. (2006).

88. Sanchez, D. R. *Recausticizing -Principles and PRactice*.

89. Lee, J., Ryu, K. H., Ha, H. Y., Jung, K.-D. & Lee, J. H. Techno-economic and environmental evaluation of nano calcium carbonate production utilizing the steel slag. *Journal of CO2 Utilization* **37**, (2020).

90. Towler, G. & Sinnott, R. *Chemical Engineering Design*. (Elsevier, 2013).

91. Green, D. W. & Perry, R. H. *Perry's Chemical Engineer's Handbook*. (Mc, 2008).

92. Christensen, P. & Dysert, L. *Cost Estimate Classification System as Applied in Engineering, Procurement, and Construction for the Process Industries*. *AACE International Recommended Practice No. 18R-97 COST, TCM Framework: 7.3 - Cost Estimating and Budgeting* (2005).

93. Woods, D. R. Appendix D: Capital Cost Guidelines. in *Rules of Thumb in Engineering Practice* 376–436 (Wiley-VCH Verlag GmbH & Co. KGaA, 2007). doi:10.1002/9783527611119.app4.

94. Jenkins, S. Plant Cost Index Archives - Chemical Engineering. *Plant Cost Index Archives - Chemical Engineering* https://www.chemengonline.com/site/plant-cost-index/ (2020).

95. Salkuyeh, Y. K., Saville, B. A. & MacLean, H. L. Techno-economic analysis and life cycle assessment of hydrogen production from different biomass gasification processes. *International Journal of Hydrogen Energy* **43**, 9514–9528 (2018).

96. Ren, J., Lau, J., Lefler, M. & Licht, S. The Minimum Electrolytic Energy Needed To Convert Carbon Dioxide to Carbon by Electrolysis in Carbonate Melts. *The Journal of Physical Chemistry C* **119**, (2015).

97. Peng, J. *et al.* Thermal Modeling for High Temperature Electrolysis of Lithium Carbonate with Carbon Dioxide Sequestration. in *2017 Ninth Annual IEEE Green Technologies Conference (GreenTech)* (IEEE, 2017). doi:10.1109/GreenTech.2017.20.

98. Stinn, C. & Allanore, A. Estimating the Capital Costs of Electrowinning Processes. *Electrochemical Society Interface* **29**, (2020).

99. CHEN, L. B. YTTRIA-STABILIZED ZIRCONIA THERMAL BARRIER COATINGS — A REVIEW. *Surface Review and Letters* **13**, (2006).

100. Khajezadeh, M. H., Mohammadi, M. & Ghatee, M. Hot corrosion performance and electrochemical study of CoNiCrAlY/YSZ/YSZ-La2O3 multilayer thermal barrier coatings in the presence of molten salt. *Materials Chemistry and Physics* **220**, (2018).

101. Ozgurluk, Y., Doleker, K. M. & Karaoglanli, A. C. Hot corrosion behavior of YSZ, Gd 2 Zr 2 O 7 and YSZ/Gd 2 Zr 2 O 7 thermal barrier coatings exposed to molten sulfate and vanadate salt. *Applied Surface Science* **438**, (2018).

102. Gates, B. *How to Avoid a Climate Disaster*. (Alfred A. Knopf, 2021).

103. Towler, G. & Sinnott, R. *Chemical Engineering Design*. (Elsevier, 2013).